Dissertation VTT PUBLICATIONS 730

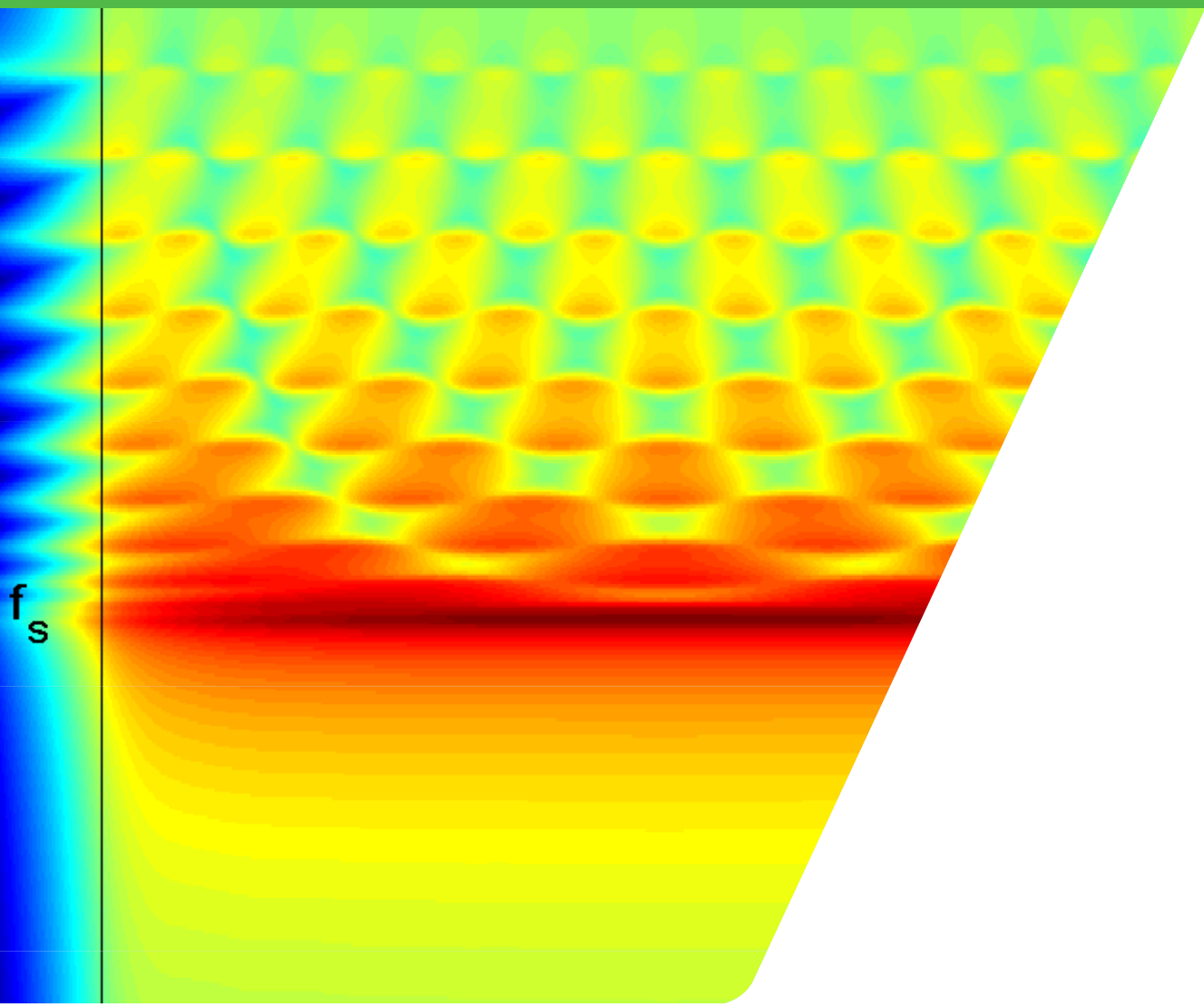

Tuomas Pensala

Thin Film Bulk Acoustic Wave Devices

Performance Optimization and Modeling

VTT PUBLICATIONS 756

Thin Film Bulk Acoustic Wave Devices

Performance Optimization and Modeling

Tuomas Pensala

Dissertation for the degree of Doctor of Science in Technology to be presented with due permission of School of Science for public examination and debate in Auditorium AS1 at Aalto University, School of Science (Otaniementie 17, Espoo Finland) on 25th of February, 2011, at 12 noon.

ISBN 978-951-38-7722-4 (soft back ed.)
ISSN 1235-0621 (soft back ed.)

ISBN 978-951-38-7723-1 (URL: http://www.vtt.fi/publications/index.jsp)
ISSN 1455-0849 (URL: http://www.vtt.fi/publications/index.jsp)

JULKAISIJA – UTGIVARE – PUBLISHER

VTT, Vuorimiehentie 5, PL 1000, 02044 VTT
puh. vaihde 020 722 111, faksi 020 722 4374

VTT, Bergsmansvägen 5, PB 1000, 02044 VTT
tel. växel 020 722 111, fax 020 722 4374

VTT Technical Research Centre of Finland, Vuorimiehentie 5, P.O. Box 1000, FI-02044 VTT, Finland
phone internat. +358 20 722 111, fax + 358 20 722 4374

Technical editing Leena Ukskoski

Edita Prima Oy, Helsinki 2011

Tuomas Pensala. Thin Film Bulk Acoustic Wave Devices. Performance Optimization and Modeling [Pietsosähköiset ohutkalvoresonaattorit. Suorituskyvyn optimointi ja mallinnus]. Espoo 2011. VTT Publications 756. 97 p. + app. 73 p.

Keywords thin film, bulk acoustic wave, BAW, AlN, ZnO, resonator, filter, GHz, microacoustic, modeling, interferometric imaging

Abstract

Thin film bulk acoustic wave (BAW) resonators and filters operating in the GHz range are used in mobile phones for the most demanding filtering applications and complement the surface acoustic wave (SAW) based filters. Their main advantages are small size and high performance at frequencies above 2 GHz. This work concentrates on the characterization, performance optimization, and modelling techniques of thin film BAW devices.

Laser interferometric vibration measurements together with plate wave dispersion modeling are used to extract the full set of elastic material parameters for sputter deposited ZnO, demonstrating a method for obtaining material data needed for accurate simulation of the devices.

The effectiveness of the acoustic interference reflector used to isolate the vibration from the substrate is studied by 1-D modeling, 2-D finite element method and by electrical and laser interferometric measurements. It is found that the Q-value of reflector-based BAW resonators operating at 2 GHz is limited to approximately 2000 by mechanisms other than leakage through the reflector.

Suppression of spurious resonances in ZnO resonators is studied in depth by modeling and measurements. It is verified that the approximate mode orthogonality is behind the suppression in boundary frame type ZnO devices operating in the piston mode, but also another narrow band mode suppression mechanism is found.

A plate wave dispersion based 2-D simulation scheme for laterally acoustically coupled BAW resonator filters is developed and employed in designing of experimental devices, which show both good agreement with the model predictions and a remarkable 4.9 % relative bandwidth.

Tuomas Pensala. Thin Film Bulk Acoustic Wave Devices. Performance Optimization and Modeling [Pietsosähköiset ohutkalvoresonaattorit. Suorituskyvyn optimointi ja mallinnus]. Espoo 2011. VTT Publications 756. 97 s. + liitt. 73 s.

Avainsanat thin film, bulk acoustic wave, BAW, AlN, ZnO, resonator, filter, GHz, microacoustic, modeling, interferometric imaging

Tiivistelmä

Pietsosähköisiin ohutkalvoihin perustuvia GHz-alueen mikroakustisia tilavuusaaltoresonaattoreita (BAW) ja niihin pohjautuvia suodattimia käytetään matkapuhelinteknologiassa kaikkein vaativimmissa suodatuskohteissa. Teknologian keskeiset edut ovat pieni koko ja hyvä suorituskyky korkeilla (≥ 2 GHz) taajuuksilla. Työssä keskityttiin BAW-resonaattoreiden karakterisointiin, suorituskyvyn optimointiin ja mallinnustekniikkoihin.

Laserinterferometrimittauksia ja Lambin aaltojen dispersion mallinnusta käytetään yhdessä ohutkalvomateriaalin elastisten materiaaliparametrien määrittämiseen. Näin demonstroidaan menetelmä, jolla voidaan parantaa mm. mallinnuksen tarkkuutta paremman materiaaliparametritiedon kautta.

Resonaattorit substraatista erottavan akustisen peilin ominaisuuksia analysoidaan 1D-malleilla, 2D-elementtimenetelmällä sekä kokeellisesti sähköisin ja laserinterferometrimittauksin. Akustista peiliä parantamalla n. 2 GHz taajuudella toimivien resonaattorien hyvyyslukua ei saada parannettua juurikaan yli 2000:n.

Sivuresonanssien vaimennusta reunapaksunnosmenetelmällä ZnO-resonaattoreissa analysoidaan mallinnuksella ja mittauksin. Tulokset osoittavat, että sivuresonanssit saadaan vaimennettua laajalla kaistalla niiden ominaismuotojen heikkoon lineaariseen riippuvuuteen perustuen, mutta myös toinen kapeakaistainen vaimennusefekti havaitaan.

Laatta-aaltojen dispersio-ominaisuuksiin perustuen kehitetään tehokas 2D-mallinnusmenetelmä, jolla voidaan simuloida horisontaalisesti akustisesti kytkettyjä suodattimia. Mallia vertaillaan kokeellisiin suodattimiin hyvin tuloksin, ja sen avulla suunniteltu kokeellinen suodatin saavuttaa 4,9 % suhteellisen kaistanleveyden 2 GHz:n taajuudella.

Preface

Development of thin film Bulk Acoustic Wave resonators and filters was started at VTT starting already in 1994 on the initiative of Nokia Mobile Phones, where Juha Ellä and Helena Pohjonen became the principal driving forces. I had the opportunity to join the highly talented team of VTT formed by Markku Ylilammi, Jyrki Kaitila, Jyrki Molarius and Meeri Partanen, and lead by Ilkka Suni, in 1998. I cannot overstate the value of that experience where I was introduced to physics, modeling, characterization, and fabrication of the BAW resonators and a highly innovative and focused way of working.

Great collaboration with the Materials Physics Laboratory of the Helsinki University of Technology in the fields of finite element modelling and interferometric vibration imaging was carried with Tapani Makkonen, Jouni Knuuttila and Prof. Martti M. Salomaa and others since the beginning of my work at VTT. The fruitful co-operation has continued since then in many projects and outside them with Kimmo Kokkonen, Olli Holmgren and others in the Optics and Photonics group at Aalto University. Their optical measurement expertise provides a magnificent direct view into the operation of the devices. I wish to thank Prof. M. Kaivola for supervising this work.

Most of the work presented in this thesis deals with optimization and deeper study of the thin film BAW technology and was carried out in the forms of both industrial co-operation and as academic collaboration. I want to thank the distinguished BAW team at Infineon Technologies for the excellent co-operation in the optimization of the resonators and the BAW team at Philips Semiconductors (later NXP Semiconductors) for very interesting work and fresh views, especially so in the field of acoustically coupled resonators.

In all of the work, the people, their knowledge, and infrastructure of the VTT Microelectronics has played an instrumental part. Close collaboration with my colleagues Johanna Meltaus, Tommi Riekkinen, James Dekker, Arto Nurmela, Mervi Hämäläinen and others over the years has made possible this thesis. I want to thank Ilkka Suni, Jouni Ahopelto and Hannu Kattelus for creating the atmosphere for a successful work.

Finally, thanks to my family for support. I should cite my eldest son Ilmari: ”Mikä ihmeen väitöskirja? Väitetäänkö siinä että aikuisten pitää leikkiä enemmän lasten kanssa?”

Abstract

Thin film bulk acoustic wave (BAW) resonators and filters operating in the GHz range are used in mobile phones for the most demanding filtering applications and complement the surface acoustic wave (SAW) based filters. Their main advantages are small size and high performance at frequencies above 2 GHz. This work concentrates on the characterization, performance optimization, and modeling techniques of thin film BAW devices.

Laser interferometric vibration measurements together with plate wave dispersion modeling are used to extract the full set of elastic material parameters for sputter deposited ZnO, demonstrating a method for obtaining material data needed for accurate simulation of the devices.

The effectiveness of the acoustic interference reflector used to isolate the vibration from the substrate is studied by 1-D modeling, 2-D finite element method and by electrical and laser interferometric measurements. It is found that the Q-value of reflector-based BAW resonators operating at 2 GHz is limited to approximately 2000 by mechanisms other than leakage through the reflector.

Suppression of spurious resonances in ZnO resonators is studied in depth by modeling and measurements. It is verified that the approximate mode orthogonality is behind the suppression in boundary frame type ZnO devices operating in the piston mode, but also another narrow band mode suppression mechanism is found.

A plate wave dispersion based 2-D simulation scheme for laterally acoustically coupled BAW resonator filters is developed and employed in designing of experimental devices, which show both good agreement with the model predictions and a remarkable 4.9 % relative bandwidth.

Tiivistelmä

Pietsosähköisiin ohutkalvoihin perustuvia GHz-alueen mikroakustisia tilavuusaaltoresonaattoreita (BAW) ja niihin pohjautuvia suodattimia käytetään matkapuhelinteknologiassa kaikkein vaativimmissa suodatuskohteissa. Teknologian keskeiset edut ovat pieni koko ja hyvä suorituskyky korkeilla ($\geq$ 2 GHz) taajuuksilla. Tässä työssä on keskitytty BAW-resonaattoreiden karakterisointiin, suorituskyvyn optimointiin ja mallinnustekniikoihin.

Laserinterferometrimittauksia ja Lambin aaltojen dispersion mallinnusta käytetään yhdessä ohutkalvomateriaalin elastisten materiaaliparametrien määrittämiseen. Näin demonstroidaan menetelmä, jolla voidaan parantaa parantaa mm. mallinnuksen tarkkuutta paremman materiaaliparametritiedon kautta.

Resonaattorit substraatista erottavan akustisen peilin ominaisuuksia analysoidaan 1D-malleilla, 2D- elementtimenetelmällä sekä kokeellisesti sähköisin ja laserinterferometrimittauksin. Todetaan, että akustista peiliä parantamalla ei n. 2 GHz taajuudella toimivien resonaattorien hyvyyslukua saada parannettua juurikaan yli 2000:n.

Sivuresonanssien vaimennusta reunapaksunnosmenetelmällä ZnO-resonaattoreissa analysoidaan mallinnuksella ja mittauksin. Tulokset osoittavat, että sivuresonanssit saadaan vaimennettua laajalla kaistalla niiden ominaismuotojen heikkoon lineaariseen riippuvuuteen perustuen, mutta myös toinen kapeakaistainen vaimennusefekti havaitaan.

Laatta-aaltojen dispersio-ominaisuuksiin perustuen kehitetään tehokas 2D-mallinnusmenetelmä, jolla voidaan simuloida horisontaalisesti akustisesti kytkettyjä suodattimia. Mallia vertaillaan kokeellisiin suodattimiin hyvin tuloksin ja sen avulla suunniteltu kokeellinen suodatin saavuttaa 4.9 % suhteellisen kaistanleveyden 2 GHz:n taajuudella.

Preface

Development of thin film Bulk Acoustic Wave resonators and filters was started at VTT starting already in 1994 on the initiative of Nokia Mobile Phones, where Juha Ellä and Helena Pohjonen became the principal driving forces. I had the opportunity to join the highly talented team of VTT formed by Markku Ylilammi, Jyrki Kaitila, Jyrki Molarius and Meeri Partanen, and lead by Ilkka Suni, in 1998. I cannot overstate the value of that experience where I was introduced to physics, modeling, characterization, and fabrication of the BAW resonators and a highly innovative and focused way of working.

Great collaboration with the Materials Physics Laboratory of the Helsinki University of Technology in the fields of finite element modelling and interferometric vibration imaging was carried with Tapani Makkonen, Jouni Knuuttila and Prof. Martti M. Salomaa and others since the beginning of my work at VTT. The fruitful co-operation has continued since then in many projects and outside them with Kimmo Kokkonen, Olli Holmgren and others in the Optics and Photonics group at Aalto University. Their optical measurement expertise provides a magnificent direct view into the operation of the devices. I wish to thank Prof. M. Kaivola for supervising this work.

Most of the work presented in this thesis deals with optimization and deeper study of the thin film BAW technology and was carried out in the forms of both industrial co-operation and as academic collaboration. I want to thank the distinguished BAW team at Infineon Technologies for the excellent co-operation in the optimization of the resonators and the BAW team at Philips Semiconductors (later NXP Semiconductors) for very interesting work and fresh views, especially so in the field of acoustically coupled resonators.

In all of the work, the people, their knowledge, and infrastructure of the VTT Microelectronics has played an instrumental part. Close collaboration with my colleagues Johanna Meltaus, Tommi Riekkinen, James Dekker, Arto Nurmela, Mervi Hämäläinen and others over the years has made possible this thesis. I want to thank Ilkka Suni, Jouni Ahopelto and Hannu Kattelus for creating the atmosphere for a successful work.

Finally, thanks to my family for support. I should cite my oldest son Ilmari: "Mikä ihmeen väitöskirja? Väitetäänkö siinä että aikuisten pitää leikkiä enemmän lasten kanssa?"

Contents

Papers 1–6 are not included in the PDF version.
Please order the printed version to get the complete publication
(http://www.vtt.fi/publications/index.jsp).

LIST OF PAPERS

1. T. Makkonen, T. Pensala, J. Vartiainen, J.V. Knuuttila, J. Kaitila, and M.M. Salomaa, "Estimating Materials Parameters in Thin-Film BAW Resonators Using Measured Dispersion Curves", IEEE Trans. on Ultrasonics, Ferroelectrics and Frequency Control, vol. 51, 2004, pp. 42–51.

2. T. Pensala, R. Thalhammer, J. Dekker, and J. Kaitila, "Experimental Investigation of Acoustic Substrate Losses in 1850-MHz Thin Film BAW Resonator", IEEE Trans. on Ultrasonics, Ferroelectrics and Frequency Control, vol. 56, 2009, pp. 2544–2552.

3. K. Kokkonen, T. Pensala, and M. Kaivola, "Dispersion and Mirror Transmission Characteristics of Bulk Acoustic Wave Resonator ", IEEE Trans. on Ultrasonics, Ferroelectrics and Frequency Control, vol. 58, 2011, pp. 215–225.

4. T. Pensala and M. Ylilammi, "Spurious Resonance Suppression in Gigahertz-Range ZnO Thin-Film Bulk Acoustic Wave Resonators by the Boundary Frame Method: Modeling and Experiment", IEEE Trans. on Ultrasonics, Ferroelectrics and Frequency Control, vol. 56, 2009, pp. 1731–1744.

5. T. Pensala, J. Meltaus, K. Kokkonen and M. Ylilammi, "2-D Modeling of Laterally Acoustically Coupled Thin Film Bulk Acoustic Wave Resonator Filters", IEEE Trans. on Ultrasonics, Ferroelectrics and Frequency Control, vol. 57, 2010, pp. 2537–2549.

6. J. Meltaus, T. Pensala, K. Kokkonen and A. Jansman, "Laterally Coupled Solidly Mounted BAW Resonators at 1900 MHz", Proc. IEEE Ultrasonics Symposium, 2009, pp. 847–850.

Author's Contribution

The work was carried out at VTT Technical Research Centre of Finland during the years 2002–2010. Experiments of Paper 1 were planned by the author together with T. Makkonen and J. Knuuttila (Materials Physics Laboratory, Helsinki University of Technology). The author performed the analysis of the experimental samples apart from the interferometric measurements and wrote the corresponding parts of the paper. The study of Paper 2 was done in collaboration with Infineon Technologies GmbH. The author planned the experiment with the co-authors and performed the characterization and analysis of the samples and results and wrote the paper. The author planned the experiments of Paper 3 together with K. Kokkonen (Applied Physics, Helsinki University of Technology) and performed the simulations and analysis of the results. For Paper 4 the author performed the measurements, simulations and analysis and wrote the paper, while the samples were results of earlier collaboration by VTT and Nokia Oyj. The model of Paper 5 was developed by the author by extending on the earlier work of M. Ylilammi (VTT) while the experiments were planned and conducted in co-operation with J. Meltaus (VTT) and K. Kokkonen (Applied Physics, Helsinki University of Technology). In Paper 6 the author contributed to the design and modeling of the experimental devices.

1 Introduction

Thin film bulk acoustic wave (BAW) resonators and filters form one of the enabling technologies for the radio technology used in the mobile phones. They serve as GHz-range passband filters selecting the appropriate range of frequencies for the mobile phone radio to receive and transmit its communications signals, blocking out the other unwanted frequencies.

1.1 The Mobile Phone and Filtering

The mobile communications revolution started in the early 1990's, bringing a portable radio – the mobile phone – that could be used as an ordinary phone but practically anywhere into the reach of anyone in a matter of less than a decade. While the number of produced mobile phones increased at incredible yearly rates, the size and price of the devices were reduced in equally astonishing pace. This created a demand for new kinds of ultra-miniature, high performance, mass-producible and cheap components making the rapid development of the mobile phones possible.

A mobile phone uses certain defined frequency ranges to transmit and receive signals. For example, an early "900 MHz" Enhanced-GSM phone transmits in channels within the range 880–915 MHz and receives in the range 925–960 MHz [1]. When receiving, the mobile phone has to be able to pick up a weak signal from a base station possibly several kilometers away at the presence of other nearby phones and other kinds of radios transmitting powerful signals. At the air interface, the signal is picked up by the antenna, and must then be amplified by a component called the low-noise-amplifier, the LNA, for further processing. On the other hand, when transmitting, the mobile phone has to output a signal of significant power (even several watts) in order to reach the base station. This signal is produced by the power amplifier, known as the PA. The LNA is designed to work with very weak signals and it is critical to block interfering unwanted signals from entering in it by filtering. On the other hand, the PA is designed to blast out a powerful radio signal, and care must be taken to limit the signal to the allocated frequency range with the aid of band-pass filters. In a GSM phone, the reception and transmission are sequenced by division into successive time slots by a switch alternating between the receive and transmit paths. In spread spectrum systems such as the CDMA (for Code Division Multiple Access) and the WCDMA (Wideband-CDMA), the reception and transmission occur simultaneously without division into time slots in frequency bands typically very close to each other. Obviously, there is a need for very efficient isolation of the receive and transmit signals. This is realized by a high performance duplexer, a three port filter having the antenna at one port and the receive and transmit paths at the two remaining ports.

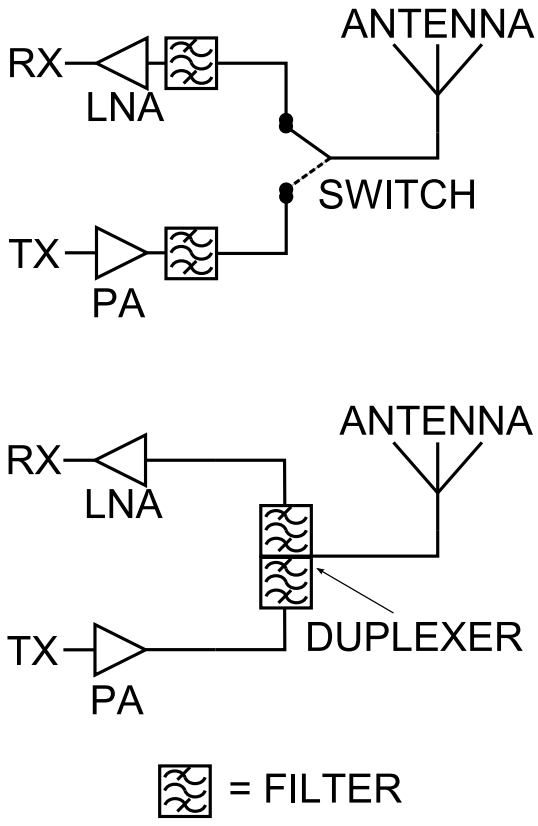

Figure 1: Illustration of usage of pass-band filters in the front-end of a GSM phone (top) and a CDMA phone (bottom). RX stands for receive path and TX for transmit path.

In the very simplest example, one filter is used for the receive path and another for the transmit path to select the desired frequencies and to suppress the undesired ones. The usage of band-pass filters in a GSM and in a CDMA phone radio front end is illustrated in Fig. 1 by simplified schematics. In actual mobile phones, more filters are needed but the detailed architectures of mobile radio systems are outside the scope of this work.

The development of the mobile phones has not only made them smaller and cheaper, but has increased their internal complexity vastly. A typical high end mobile phone can communicate in several GSM bands and several WCDMA bands. As an example, the Nokia N8 smartphone works in the GSM bands at 850, 900, 1800 and 1900 MHz and in WCDMA bands at 850, 900, 1700, 1900, and 2100 MHz [2]. In addition, the same device has WLAN, Bluetooth, and FM radios. A significant number of high performance filters are needed in extremely small form factor to facilitate realization of such a communications device.

1.2 Microacoustic Filters for Radio Frequencies

Filtering a radio signal requires structures that are comparable to the wavelength of the carrier wave. At 1 GHz, the wavelength of an electromagnetic wave in air is 30 cm and at 2 GHz half of that, both being larger than the dimensions of a mobile phone. The key to the extreme miniaturization of GHz range filters is transformation of the electromagnetic wave to an acoustic wave via the piezoelectric effect. The velocities of acoustic waves in solids are typically in the range of 3000–11000 m/s, which is five decades less than the velocity of an electromagnetic wave. The wavelength is reduced by the same fraction – into the micrometer range in case of GHz frequencies. This allows for fabrication of microacoustic filters for the GHz-range with sub-millimeter dimensions.

Practically all the filters in a mobile phone are nowadays of the microacoustic type. The dominating technology utilizes surface acoustic waves (SAW) traveling along the surface of a single crystal piezoelectric substrate such as $\mathrm{LiTaO_3}$, $\mathrm{LiNbO_3}$ or quartz [3]. The thin film BAW filters utilizing a longitudinal wave in the thickness direction of a vacuum-deposited polycrystalline piezoelectric thin film have been developed to extend the range of applicability of microacoustic filters.

The SAW filter technology is well applicable for frequencies up to 2 GHz, but above that the critical dimensions of the devices become so small that problems with economical manufacturing, robustness and power handling arise. Also, SAW filters suffer from fairly large temperature drift of frequency. Another drawback of the SAW devices is that the Q-values, translating directly to the steepness of passband skirts, remain below 1000. It is in the high frequency end, that the BAW filter technology provides advantages in Q-values, temperature stability, and power handling capability. In the low frequencies the BAW filters have as disadvantage a fairly large size. For a detailed comparison of SAW and BAW filter technologies, see [3].

The break-through application band of the thin film BAW technology was the US-PCS CDMA utilized in North America. The transmit band is at 1850–1910 MHz and the receive band at 1930–1990 MHz, leaving only 20 MHz (1.05 %) gap in between [1]. The filtering used to be done with a ceramic duplexer which was unimaginably large to be fit into a mobile phone of today. The SAW technology had great difficulties trying to bring about a microacoustic solution due to the low Q-values and large temperature drift leading to specification violations in the guard band between the receive and transmit bands. The thin film BAW technology, instead, managed to provide a duplexer with high performance and greatly reduced size. This was allowed mainly by the high Q and low temperature drift of the AlN resonators of Hewlett Packard Laboratories (later Agilent and Avago Technologies) [4]. Later, SAW duplexers for the same application were

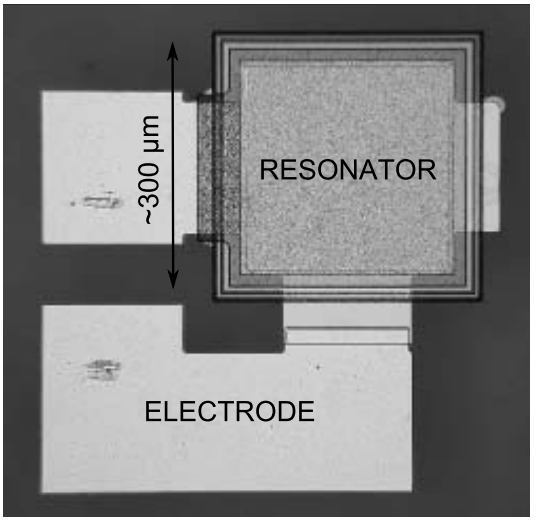

Figure 2: Photograph of a 932 MHz ZnO resonator based on a $\mathrm{SiO_2 - W}$ acoustic reflector on glass substrate. The active area (grainy square at top right) has an area of $300 \times 300\ \mu\mathrm{m}^2$.

developed [5], but the BAW filters have since established a position in the high performance and high frequency end of mobile phone filters, the US-PCS and some WCDMA bands being the main applications [3].

In this work, mainly the properties of a single BAW resonator (Fig. 2), which is a basic building block of a ladder filter ([6], Fig. 16), are considered. It is the characteristics of the individual resonators that dictate the achievable performance of the ladder filters. The field of ladder filter design itself is not entered but filters based on lateral acoustical coupling of adjacent resonators are discussed.

2 BAW Basics

2.1 The Crystal Resonator

A bulk acoustic wave crystal resonator consists of a thin slab of piezoelectric crystal which is metallized on both sides for applying an exciting voltage (Fig. 3). The plate exhibits a resonance whenever an integer multiple of half an acoustic wavelengths fits within the resonator thickness t, at frequencies

$$f_N = \frac{vN}{2t}, \tag{1}$$

where v is the acoustic velocity of the wave mode in question (shear or longitudinal), N an integer multiplier, and t the thickness of the crystal. Only odd values of N lead to piezoelectric coupling as even N correspond to antisymmetric modes. The electrical frequency response of the resonator is that of a capacitor except near a resonance, where it has in addition to a resonance (at f_r in Fig. 4) an anti-resonance (f_a), the frequency separation of which is a measure of the strength of the piezoelectric effect in the device. Resonators with very low losses, i.e. high Q-value, can be fabricated from for example quartz, yielding for highly frequency selective resonators. The traditional method of fabricating crystal oscillators include fabrication of bulk crystals, from which thin plates are diced, ground and polished down to a desired thickness. It is the dimensions produced by this manufacturing process that determine the resonance frequency of the resonators, followed by a possible trimming step. It is difficult to thin down a crystal plate down to the micrometer scale, limiting the quartz resonators' frequencies typically in the range below 200 MHz [7].

The crystal resonators can be connected to an active circuit to form an oscillator, or they can be connected in a ladder topology to form a passive filter (see Sec. 4.1). The most common material used for crystal resonators, quartz, exhibits only very weak piezoelectricity allowing for narrow band filters only [8].

The thin film BAW resonator technology is based on the same principal structure, but the piezoelectric material as well as the electrodes, are produced by vacuum deposition of thin films. Standard lithography and etching methods used in microelectronic circuit fabrication are employed to pattern the films into devices. This allows for micrometer-range dimensions and subsequently GHz-range resonance frequencies. Furthermore, the piezoelectric thin films such as ZnO and AlN exhibit a much stronger piezoelectric effect than quartz, yielding for a possibility to create passband filters with a relative bandwidth of several percent.

Thin film technology requires a substrate such as silicon or glass wafer to provide a mechanical support for the films. The vibration, however, needs to be contained within the thin film resonator structures. Two methods for providing

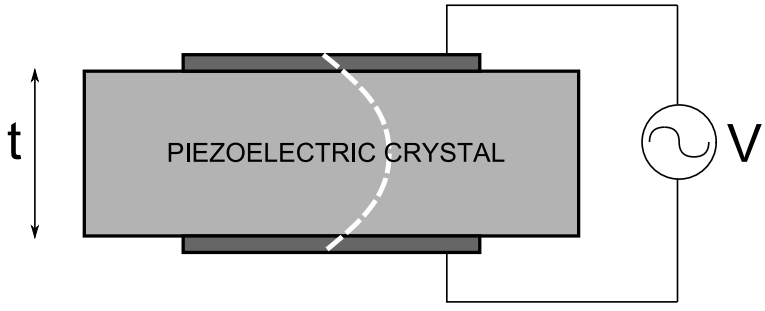

Figure 3: The structure of a crystal resonator. Stress distribution of the fundamental half-wavelength thickness resonance is illustrated with the dashed line.

this are used: 1) In membrane type resonators (often called FBAR) the substrate or a sacrificial layer between the resonator and the substrate is removed to generate an air interface at the lower surface of the resonator [9, 10]. 2) In Bragg reflector based resonators, suggested by Newell already in 1965 [11], often referred to as the solidly mounted resonators (SMR), an acoustic interference reflector consisting of alternating layers of high and low acoustic impedance each quarter of an acoustic wavelength in thickness, is fabricated between the resonator and the substrate. Both of these types are in industrial production [12, 13, 14]. The main variations of the air gap resonators are illustrated in the top row and the SMR type at the bottom of Fig. 5.

Aluminium nitride is the piezoelectric material used in all commercial applications of thin film BAW, although a fair amount of research has been conducted with ZnO-based technology [15, 16, 17, 18, 19]. The key properties of the two materials are compared in Table 1. The electromechanical coupling coefficient is slightly stronger in ZnO, which actually exhibits the strongest piezoeffect of all non-ferroelectric materials. This very desirable property for filter applications is somewhat eaten up by the twice as large temperature drift of frequency as compared to AlN. The dielectric permittivities of the two materials are very similar, close to $10 \cdot \varepsilon_0$. AlN exhibits very large sound velocities, leading to thicker layers for a given frequency. The acoustic impedances are of the same order, but the Poisson ratio differs significantly being very large for ZnO and fairly small for AlN.

The main reasons for AlN being the dominant material in the industry is that it

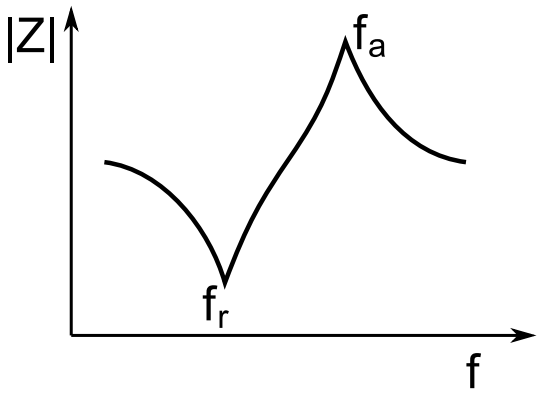

Figure 4: Magnitude of impedance of a piezoelectric crystal resonator showing resonance-antiresonance behavior.

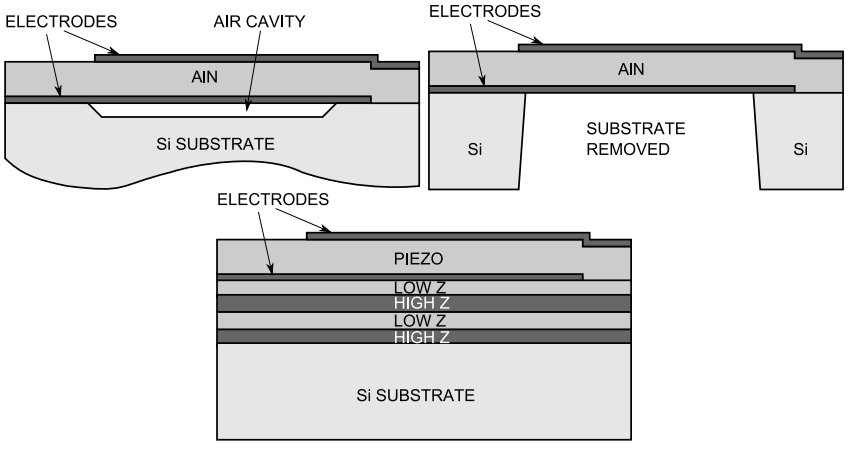

Figure 5: An air gap or FBAR type resonator structure fabricated by sacrificial layer etching (top left), a self supported membrane resonator fabricated by through-wafer etching (top right), and a Bragg reflector/SMR type resonator (bottom).

is compatible with integrated circuit (IC) fabrication processes unlike ZnO. This is important not because of the monolithic integration possibility of thin film BAW and active silicon circuits as visioned earlier [9], but because an IC facility can be used to fabricate AlN BAW devices removing the need for a dedicated facility [22]. Another key issue is the small temperature drift of AlN as compared to ZnO and especially as compared to SAW devices. AlN and ZnO are most often deposited by sputtering. In order to display piezoelectric effect of the same order as in bulk crystal, the piezofilms must be deposited under very well controlled conditions. A considerable effort in the development of such deposition processes had to take place before commercial manufacturing of thin film BAW devices was feasible.

Table 1: Comparison of ZnO and AlN properties relevant to wave propagation along the c-axis (aligned with z-axis) [20, 6, 21]. The definition $K^2 = \frac{e_{33}^2}{\varepsilon_{33} c_{33}^E}$ is used for the electromechanical coupling coefficient.

Material	AlN	ZnO
density ρ $(\mathrm{kg/m^3})$	3405.5	5680
longitudinal wave velocity v_l (m/s)	11250	6366
shear wave velocity v_s (m/s)	6329	2734
long. wave impedance Z_l $(\mathrm{kg/m^2/s} \cdot 10^6)$	38.3	36.2
shear wave impedance Z_s $(\mathrm{kg/m^2/s} \cdot 10^6)$	21.6	15.5
Poisson ratio ν	0.246	0.387
piezoelectric stress coefficient e_{33} $(\mathrm{C/m^2})$	1.5	1.32
dielectric permittivity ε_{33} (ε_0)	9.66	10.2
electromechanical coupling coefficient $K^2(\%)$	6.5	9.15
temperature coefficient of frequency TCF (ppm/K)	-25	-60
CMOS compatible	yes	no
crystal symmetry	6mm (hex.)	6mm (hex.)

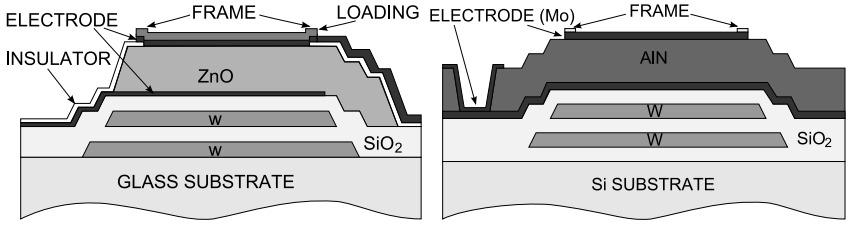

Figure 6: Structures of a two different solidly mounted ZnO resonators fabricated at VTT. The ZnO resonator (left) is based on glass substrate and mostly wet etching, while the AlN resonator one on the right uses a high-resistivity Si substrate and dry etching processes. Both employ a $\mathrm{W} - \mathrm{SiO_2}$ reflector and a boundary frame type spurious resonance suppression structure [23]. A mass loading layer for frequency shifting is shown on the ZnO resonator only but can be applied in the same manner also for the AlN resonators.

Detailed cross sectional structures of two different actual SMR BAW resonators fabricated at VTT are shown in Fig. 6. On the left is shown a ZnO resonator [23] of the kind studied in Papers 4 and 3, and on the right an AlN resonator.

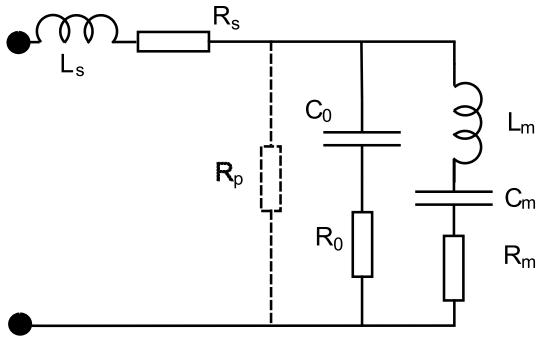

Figure 7: The modified Butterworth-van Dyke (mBvD) equivalent circuit representation of a piezoelectric resonator. The modifications consists of adding the loss resistors $R_{\rm s}$, R_0 and $R_{\rm p}$ to the standard BvD circuit. Additional series inductor $L_{\rm s}$ is also often used in series with $R_{\rm s}$.

2.2 The Equivalent Circuit Representation

Piezoelectric crystal and thin film resonators can be described with the Butterworth van Dyke (BvD) equivalent circuit [24]. The circuit, slightly modified from what is usually understood as the BvD circuit is shown in Fig. 7. The modifications by Larson *et al.* [25] include the addition of two loss resistors $(R_{\rm s}, R_0)$ to improve the match to real thin film BAW devices. A series inductance $L_{\rm s}$ is added to represent the inductance formed by the electrode layout of the resonator and the finite resistivity of the piezolayer can be described by the resistor $R_{\rm p}$, which is usually insignificant.

In its standard form, the BvD circuit consists of a mechanical resonance branch $(L_{\rm m}, C_{\rm m}, R_{\rm m})$ and a capacitance C_0 in parallel. The capacitance C_0 is simply the plate capacitance formed by the piezoelectric film or crystal sandwiched between the electrodes and is given by (ignoring fringing field contribution)

$$C_0 = \frac{A\varepsilon^S}{t}, \tag{2}$$

where A is the area of the resonator, ε^S is the permittivity of the piezolayer in constant strain, and t is the thickness of the piezolayer. Nominally, the series resistor $R_{\rm s}$ describes the resistance of the electrodes, the resistor R_0 the dielectric losses in the piezo-material, $R_{\rm m}$ the acoustic losses (viscous, radiative), and $R_{\rm p}$ the finite resistivity of the piezolayer.

Such a circuit exhibits a resonance-antiresonance behavior. In resonance, the reactance of the mechanical branch,

$$X_{\rm m} = \omega L_{\rm m} + \frac{1}{\omega C_{\rm m}}, \tag{3}$$

vanishes and current is drawn by the circuit through the mechanical branch, limited only by resistances R_s and R_m. The resonance frequency ω_r is thus obtained from

$$\omega_\mathrm{r}^2 = \frac{1}{L_\mathrm{m} C_\mathrm{m}}. \tag{4}$$

In anti-resonance, the reactance around the loop formed by the mechanical branch and the C_0-branch,

$$X_0 + X_\mathrm{m} = \frac{1}{\omega C_0} + \omega L_\mathrm{m} + \frac{1}{\omega C_\mathrm{m}}, \tag{5}$$

vanishes, leading to an anti-resonance frequency at

$$\omega_a^2 = \frac{L_\mathrm{m}(C_0 + C_\mathrm{m})}{C_0 C_\mathrm{m}}. \tag{6}$$

In the anti-resonance, very little current is drawn by the circuit, but a resonant current circulates around the loop formed by the plate capacitance C_0 and the mechanical branch. Electrically, the resonance and anti-resonance can be considered as the short circuit or series resonance and the open circuit or parallel resonance, respectively.

While the expression (6) is not exact, it is a very good approximation sufficient for all practical purposes. The exact resonance and antiresonance frequencies can be solved from the minimum and maximum, respectively, of the mBvD-circuit impedance

$$Z_\mathrm{mBvD} = j\omega L_\mathrm{s} + R_\mathrm{s} + \frac{1}{R_0 + \frac{1}{j\omega C_0} + \frac{1}{R_\mathrm{m} + \frac{1}{j\omega C_\mathrm{m}} + j\omega L_\mathrm{m}}}. \tag{7}$$

The relative difference of the resonance and antiresonance frequencies is an important figure of merit related to the effective coupling coefficient of the resonator. Using the definition

$$k_\mathrm{eff}^2 = \frac{\omega_\mathrm{a}^2 - \omega_\mathrm{r}^2}{\omega_\mathrm{a}^2}, \tag{8}$$

[26], one finds the direct connection to the equivalent circuit parameters

$$k_\mathrm{eff}^2 = \frac{C_\mathrm{m}}{C_0 + C_\mathrm{m}}. \tag{9}$$

It is to be noted that several different definitions for the coupling coefficient are being used in the literature (see Section 2.4 for a brief discussion).

The loss resistors of the circuit define the Q-values. A commonly used definition for the Q-value of an electrical circuit is

$$Q = \frac{\omega}{2} \left| \frac{d\phi}{d\omega} \right|_{\omega_0}, \tag{10}$$

where $\phi = \arg(Z_{\mathrm{in}})$ is the phase of the input impedance (7) of the circuit. For the mBvD circuit, which exhibits a resonance - anti-resonance (i.e. series and parallel resonance) behavior, this definition leads to the Q-values

$$Q_{\mathrm{r}} \approx \frac{\omega_r L_{\mathrm{m}}}{R_{\mathrm{s}} + R_{\mathrm{m}}} \tag{11}$$

and

$$Q_{\mathrm{a}} \approx \frac{\omega_a L_{\mathrm{m}}}{R_0 + R_{\mathrm{m}}} \tag{12}$$

at the resonance ω_{r} and at the antiresonance ω_{a}, respectively. It is seen that the Q_{r} is loaded by the electrical series resistance, whereas Q_{a} is defined by the internal losses only. This is important in measurement of actual devices since it implicates that the Q-value at the antiresonance is not affected by the electrode resistances nor by a possible contact resistance in the measurement. Further, one can define a purely mechanical Q-value as

$$Q_{\mathrm{mech.}} = \frac{\omega_{\mathrm{a}} L_{\mathrm{m}}}{R_{\mathrm{m}}}. \tag{13}$$

If one measures the complex input impedance $Z(\omega)$ of the resonator, one can extract the resonance frequencies ω_{r} and ω_{a} from e.g. the minimum and maximum of $|Z(\omega)|$ and calculate the Q-values (11) and (12). The plate capacitance C_0 can be either calculated based on the known geometry of the resonator or also extracted from a measurement. With this information one is able to fix the equivalent circuit parameters using the following associations:

$$C_{\mathrm{m}} = \frac{k_{\mathrm{eff}}^2}{1 - k_{\mathrm{eff}}^2} C_0, \tag{14}$$

$$L_{\mathrm{m}} = \frac{1}{\omega_{\mathrm{r}}^2 C_{\mathrm{m}}}, \tag{15}$$

$$R_{\mathrm{m}} = \frac{\omega_{\mathrm{r}} L_{\mathrm{m}}}{Q_{\mathrm{r}}}. \tag{16}$$

An actual resonator can exhibit more than a single mechanical resonance, such as higher harmonic resonances and spurious resonances near the main resonances

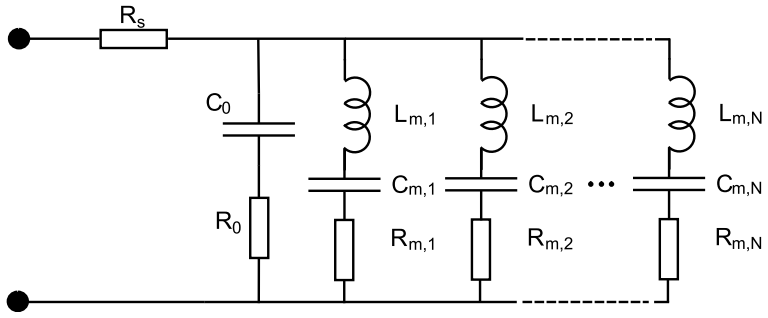

Figure 8: The many-mode modified Butterworth-van Dyke (mBvD) equivalent circuit representation of a piezoelectric resonator. Each mechanical branch corresponds to a single resonance.

[27]. The nature of these will be discussed later. Additional mechanical branches can be added in parallel to the the equivalent circuit to represent each mode [28].

The admittance of the multi-resonance circuit (Fig. 8) is (assuming for simplicity that R_s and R_0 are small enough to be neglected)

$$Y = j\omega C_0 + \sum_{p=1}^{N} \frac{1}{R_{\mathrm{m}p} + j\omega L_{\mathrm{m}p} + \frac{1}{j\omega C_{\mathrm{m}p}}}, \tag{17}$$

where the p indexes the resonance modes and ω_p refers to the resonance frequency of each mode.

With the connections (14)–(16) this can be expressed as

$$Y = j\omega C_0 + \sum_{p=1}^{N} \frac{k_p^2}{1-k_p^2} C_0 Q_p \omega_p \frac{1}{1 + \frac{Q_p(\omega_p^2 - \omega^2)}{j\omega\omega_p}} \tag{18}$$

emphasizing the fact that the parameter sets ($C_0, k_{\mathrm{eff},p}, Q_p, \omega_p$) suffice to define the response of the device. This expression is of importance in developing the models used for spurious resonances and lateral inter-resonator coupling in Papers 4 and 5.

The equivalent circuit elements can be obtained by 1) fitting the circuit response to a measured response of a resonator or 2) by using an acoustic model to simulate a resonator and derive its electrical response from the results. The former is typically used to reduce the measured frequency response of a resonator to a limited set of parameters that can be used to assess the resonator performance and to further calculate how a filter comprising such resonators would perform. The latter serves for the basic resonator design tasks.

2.3 Electrical Characterization of BAW Resonators

The thin film BAW resonators are typically characterized by measuring the scattering parameters S_{ij} of a resonator with a vector network analyzer (VNA) on wafer level with RF-probes. A resonator can either be fabricated as a one- or two-port device (Fig. 9 a) and b), respectively). To assess the performance of a single resonator it suffices to measure only the reflection coefficient S_{11} of a one-port configuration, but filters are obviously two-port devices.

The VNA is calibrated to the plane of the probe tips, indicated by the dashed line in Fig. 9. The device under test consists of everything beyond that plane. The remaining parasitic contributions from the measurement setup that are difficult to remove by any calibration include the contact resistance from the probes to the contact pads and the inductance of the loop formed by the electrodes from tip to another.

The VNA measurement is performed within the characteristic impedance $Z_0 = 50\ \Omega$ environment. From the measured S_{11}, the input impedance is obtained by

$$Z_{\mathrm{in}} = \frac{1 + S_{11}}{1 - S_{11}} Z_0. \tag{19}$$

One can directly compare this with the impedance of the mBvD equivalent circuit (7). Typically, a fit of the mBvD-equivalent circuit is performed to the measurement data in order to reduce it into a small set of descriptive parameters. In order to be able to make comparisons between resonators, the fitting procedure must be very stable even in the presence of noise, variation in contact resistance, and spurious resonances. In Paper 2, the difficulties in the fitting and extraction of the Q-value were discussed and it was concluded that in order to analyze small differences in the performance of resonators, direct comparison of raw data is also needed.

Within the same study, an equivalent circuit fitting procedure was constructed by improving the one developed earlier by Infineon Technologies GmbH. The main improvement achieved was the increased stability of the fitted Q-value in the presence of spurious ripple in the measurement data. The fitting algorithm is summarized below (for the definitions of the fitting parameters, see Section 2.2):

1. Make a first rough guess for the circuit parameters based on directly extracted $\omega_{\mathrm{r}}, \omega_{\mathrm{a}}, C_0, Q_{\mathrm{r}}$, and Q_{a}.

2. Fit C_0 and Q_{mech} using S_{11} data points with a large radius on the Smith chart (to avoid bias from spurious ripple).

3. Fit R_{s} and R_0 using input impedance phase data outside resonance with an asymmetric cost function that prevents from fitting too large an R_{s} (R_{p} defaults to $1\ \mathrm{M}\Omega$ unless detected to have a significantly small value).

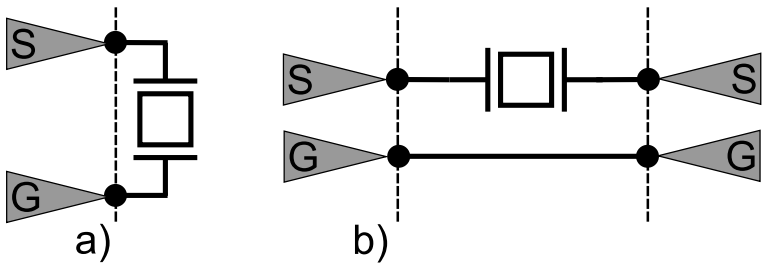

Figure 9: One-port (a) and two-port (b) configurations for electrical measurements of thin film BAW resonators. The RF-probes are represented by the gray triangles, S standing for signal and G for ground connection. The dashed line represents the plane of calibration.

4. Fit again C_0 and Q_{mech} using data points with a large radius on the Smith chart.

5. Refit ω_{r} and ω_{a} using data points with large radius on the Smith chart.

It is important to use a fitting procedure instead of direct extraction by equations (8), (10) etc. as noise and spurious resonances can cause large local deviations in the directly extracted ω_{r}, ω_{a}, and the derivative of the phase of the impedance not reflecting the actual overall performance of the device [29].

2.4 Definitions for Effective Coupling Coefficients

In the literature, several different definitions are being used for the effective electromechanical coupling coefficient of piezoelectric resonators (for a summary, see [29]). One of the most often used is

$$K^2 = \frac{\pi}{2}\frac{f_{\mathrm{s}}}{f_{\mathrm{p}}}\left[\tan\left(\frac{\pi}{2}\frac{f_{\mathrm{s}}}{f_{\mathrm{p}}}\right)\right]^{-1}, \tag{20}$$

where f_{s} and f_{p} are the series and parallel resonance frequencies, respectively. They stand for the resonance and anti-resonance frequencies and from here on the serial and parallel resonances are used synonymously with resonance and antiresonance, respectively.

Definition (20) has it origins in an analytical 1-D solution for a piezoelectric slab with infinitesimally thin electrodes. Approximations of this include

$$K^2 = \frac{\pi^2}{4}\frac{f_s}{f_p}\frac{f_\mathrm{p} - f_\mathrm{s}}{f_\mathrm{p}}, \tag{21}$$

and

$$K^2 = \frac{\pi^2}{4}\frac{f_\mathrm{p} - f_\mathrm{s}}{f_\mathrm{p}}. \tag{22}$$

Another version of the latter with f_p in the denominator replaced by f_s has also been used. The usage of several different definitions, reporting squared or non-squared values, makes comparison of reported resonator performances quite difficult. It is better to always report the exact resonance frequencies f_s and f_p along with an explicitly defined coupling coefficient in order to avoid misunderstandings.

The fundamental phenomenon to be measured is the effective electromechanical coupling coefficient which manifests itself in the relative frequency difference of f_s and f_p. This coefficient is in thin film BAW resonators affected by material parameters (piezoelectric film quality), electrodes, the rest of the layer stack (especially in the SMR type devices), lateral design, size of the resonator [30], and parasitic capacitances and inductances.

We have chosen to use the definition

$$k_\mathrm{eff} = \sqrt{\frac{f_\mathrm{p}^2 - f_\mathrm{s}^2}{f_\mathrm{p}^2}}, \tag{23}$$

from [26] due to its simplicity as a function of the resonance frequencies, and even more importantly, due to its direct connection to the equivalent circuit representation via (9):

$$k_\mathrm{eff}^2 = \frac{C_\mathrm{m}}{C_0 + C_\mathrm{m}}. \tag{24}$$

The fundamental meaning of the electromechanical coupling coefficient is to measure the efficiency of the piezoelectric device in converting electrical energy to mechanical energy and vice versa. This is clear in the definition of Berlincourt [31] for the coupling,

$$k^2 = \frac{U_\mathrm{m}^2}{U_\mathrm{e}U_\mathrm{d}} \tag{25}$$

where U_m is the so-called mutual energy (energy capable of conversion), U_e is the elastic energy, and U_d is the dielectric energy. Following Kaitila [23, 32], we assume that only vertically (z) directed stress and electric fields exist, but that the

fields have a lateral (x)-dependence of a separable form. The energy terms can be expressed as:

$$U_{\mathrm{m}} = \frac{1}{2} \int_v d_{zz} T_z E_z \, dv, \tag{26}$$

$$U_{\mathrm{e}} = \frac{1}{2} \int_v s^E_{zz} T_z^2 \, dv, \tag{27}$$

and

$$U_{\mathrm{d}} = \frac{1}{2} \int_v \varepsilon^T_{zz} E_z^2 \, dv. \tag{28}$$

Here d_{zz} is the piezoelectric strain constant for longitudinal z-directed strain, T_z is the longitudinal strain in the z-direction, E_z is the electric field in the z-direction, ε^T_{zz} is the corresponding permittivity, and s^E_{zz} is the compliance for longitudinal strain in the z-direction. The integration is performed over the volume of the device.

Now, following Kaitila [32], assume that in a vertical resonator with one lateral dimension (x) the stress field can be expressed as

$$T_z = T'_z(z) u(x), \tag{29}$$

and the electric field as

$$E_z = E'_z(z) E_0(x), \tag{30}$$

where $u(x)$ is a lateral shape function (mode shape) and $E_0(x)$ is the lateral distribution of the electric field (e.g. unity over electrode and zero elsewhere) and the primed variables are the z-dependent fields. Substitution of (29)–(30) into (26)–(28) leads to

$$U_{\mathrm{m}} = \frac{d_{zz}}{2} \int_z T'_z(z) E'_z(z) \, dz \int_x u(x) E_0(x) \, dx \tag{31}$$

$$U_{\mathrm{e}} = \frac{s^E_{zz}}{2} \int_z T'^2_z(z) \, dz \int_x u(x)^2 \, dx \tag{32}$$

$$U_{\mathrm{d}} = \frac{\varepsilon^T_{zz}}{2} \int_z E'^2_z(z) \, dv \int_x E_0^2(x) \, dx. \tag{33}$$

The Berlincourt formula (25) now gives

$$k^2 = \frac{d_{zz}^2}{s^E_{zz} \varepsilon^T_{zz}} \cdot \frac{\left[\int_z T'_z(z) E'_z(z) \, dz \right]^2}{\int_z T'^2_z(z) \, dz \int_z E'^2_z(z) \, dz} \cdot \frac{\left[\int_x E_0(x) u(x) \, dx \right]^2}{\int_x u^2(x) \, dx \int_x E_0^2(z) \, dx}. \tag{34}$$

The first two terms form the 1-D-coupling (or the Mason-model coupling) $k_{1\mathrm{D}}^2$, solely dependent on the vertical fields and the last term establishes the dependence on the lateral distribution of the fields,

$$k^2 = k_{1D}^2 \frac{\left[\int\limits_x E_0(x)u(x)\ dx\right]^2}{\int\limits_x u^2(x)\ dx \int\limits_x E_0^2(z)\ dx}. \tag{35}$$

This result is utilized in the modeling of the lateral effects in the BAW devices in Papers 4 and 5. It is to be noted that as the mutual energy (26) is an integral over the product of stress and electric field, no contribution to the coupling coefficient comes from areas where the electric field is zero. The important practical consequence of this is that vibration in areas where no electrical field is applied reduces the effective piezoelectric coupling of the resonator.

3 One Dimensional Picture of the BAW Resonator

3.1 One Dimensional Acoustic Model of the Resonator

The equivalent circuit of a BAW resonator does not contain any direct information of its operation physics if the circuit elements are not associated to the actual physical device. The work horse for the modeling of the BAW resonator is an electro-acoustic 1-D model applied in the wave propagation direction discarding the lateral dimensions. The model of Mason is often used for this purpose [33, 24]. It presents the acoustic layers as acoustic transmission lines and the piezoelectric layer with an additional electrical port via a transformer. Instead of the standard Mason model, a transfer matrix model formulated by M. Ylilammi [34] is used in this work. The transfer matrix model is equivalent to the Mason model but emphasizes the acoustics not resorting to electrical circuit description. As it serves to review the basic physics of piezoelectric resonators, the formulation of the transfer matrix method is outlined below.

Consider a stack of layers indexed by i, each of thickness t_i (Fig. 10). It is assumed that in each of the layers, there are two plane waves traveling up and down, with complex amplitudes A_i and B_i, respectively:

$$u_i(z) = A_i e^{-j\beta_i z} e^{j\omega t} + B_i e^{j\beta_i z} e^{j\omega t}. \tag{36}$$

Here $\beta_i = v_{\mathrm{ac.,i}}/\omega$ is the wave number in layer i, $v_{\mathrm{ac.,i}}$ being the acoustic wave

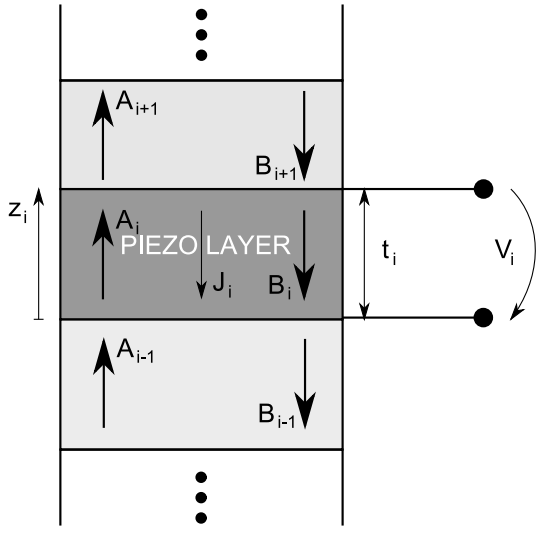

Figure 10: Geometry of the 1-D transfer matrix model for a multilayered BAW resonator.

velocity in that layer. The stress in the layers can be found by using the constitutive relations

$$T_i = c_i^E S_i - e_i E_i \tag{37}$$
$$D_i = \varepsilon_i^S E_i + e_i S_i, \tag{38}$$

where T_i is the stress, D_i the electric displacement field, c_i^E the stiffness in a constant electric field, e_i is the piezoelectric stress coefficient, $S_i = \partial u_i/\partial z$ is the strain, and E_i is the electric field. From (38) one can solve the electric field as E_i

$$E_i = -\frac{e_i}{\varepsilon_i^S} S_i - j\frac{J_i}{\varepsilon_i^S \omega}, \tag{39}$$

where the connection $J_i = j\omega D_i$ between the current density and the electric displacement field D_i has been used assuming harmonic time dependence of the fields. Substituting this into (38) one obtains

$$T_i = c_i \frac{\partial u_i}{\partial z} + j\frac{h_i J_i}{\omega}, \tag{40}$$

where $c_i = c_i^E + e_i^2/\varepsilon_i^S$ is the piezoelectrically stiffened stiffness, $h_i = e_i/\varepsilon_i^S$ is the piezoelectric coefficient, and J_i the current density trough the layer (excitation). For a non-piezoelectric layer with $e_i = 0$ the stress is simply

$$T_i = c_i^E \frac{\partial u_i}{\partial z}. \tag{41}$$

The boundary conditions at the layer interfaces require that that the displacement and the stress are continuous

$$u_{i+1}(z_{i+1} = 0) = u_i(z_i = t_i) \tag{42}$$
$$T_{i+1}(z_{i+1} = 0) = T_i(z_i = t_i). \tag{43}$$

Layer-wise z-coordinates extending from zero to the thickness of the layer t_i have been employed here.

Applying (42)–(43) and solving for the amplitudes A_{i+1}, B_{i+1} as function of those in the layer below A_i, B_i, one finds a layer transfer matrix M_i and a source term C_i to yield

$$\begin{bmatrix} A_{i+1} \\ B_{i+1} \end{bmatrix} = M_i \begin{bmatrix} A_i \\ B_i \end{bmatrix} + C_i. \tag{44}$$

The 2×2 matrix M_i is a function of the acoustic impedances Z_i of the layer materials, layer thicknesses and frequency/wave number $M_i = M_i(Z_i, Z_{i+1}, k_i, \omega, t_i)$, in detail

$$M_i = \frac{1}{2} \begin{bmatrix} e^{-j\beta_i t_i}\left(1 + \frac{Z_i}{Z_{i+1}}\right) & e^{j\beta_i t_i}\left(1 - \frac{Z_i}{Z_{i+1}}\right) \\ e^{-j\beta_i t_i}\left(1 - \frac{Z_i}{Z_{i+1}}\right) & e^{j\beta_i t_i}\left(1 + \frac{Z_i}{Z_{i+1}}\right) \end{bmatrix}. \tag{45}$$

The source term $C_i = C_i(h_{i,i-1}, J_{i,i-1}, \omega, Z_i)$ contains the piezoelectric contribution and is of the from

$$C_i = \frac{h_i J_i - h_{i-1} J_{i-1}}{2\omega^2 Z_i} \begin{bmatrix} 1 \\ -1 \end{bmatrix}, \tag{46}$$

but is calculated recursively as is evident from (44).

Possible boundary conditions at the extreme ends of the stack can be 1) vacuum interface, where the stress T must vanish or 2) infinite half-space of some material, where only outgoing waves exist (assuming that the excitation can only be done by driving current density J_{piezo} through the piezolayer).

For given boundary conditions, the amplitudes (A_i, B_i) can be calculated in each layer i of the 1-D stack as a response to a harmonic current density J_{piezo} present at the piezolayer. The vibration response of the stack, $u_i(z)$, is obtained via (36), the strain from $S_i = \partial u_i / \partial z$, and the stress from (40). The voltage over the piezolayer, V_{piezo}, is then obtained by integrating (39) over the thickness of the piezolayer t_{piezo} leading to

$$V_i = -j \frac{J_i t_{\text{i}}}{\varepsilon^S \omega} + \frac{e_i}{\varepsilon_i^S} \left[A_i (1 - e^{-j\beta_i t_i}) + B_i (1 - e^{j\beta_i t_i}) \right], \tag{47}$$

where index i refers to the piezolayer.

Equation 39 yields the electrical impedance Z_{in} of the device as the input impedance of the resonator is obtained from

$$Z_{\text{in}} = \frac{V_{\text{piezo}}}{A J_{\text{piezo}}}, \tag{48}$$

where A is the assumed area of the resonator. This scaling into two lateral dimensions is needed in order to compare the 1-D predictions with measurements. Here we have assumed constant current drive, but having obtained the input impedance, it is straightforward to use (48) to calculate the current density due to constant voltage drive and use that as excitation in a simulation again to obtain the vibration response to a constant voltage drive.

In the lossless case, the wavenumber β_i is given by

$$\beta_i = \frac{\omega}{v_i}. \tag{49}$$

Viscous losses can be incorporated in the model by employing a complex wavenumber $\hat{\beta}$ and acoustic impedance $\hat{Z}$ [24],

$$\hat{\beta}_i = \frac{\omega}{v_i} - i \frac{\eta_i \omega^2}{2 v_i^3 \rho_i} \tag{50}$$

and

$$\hat{Z}_i = \frac{c_i}{v_i} - i\frac{\eta_i \omega}{2v_i}. \tag{51}$$

Here η_i is the viscosity and ρ_i the density of the material of layer i.

With the 1-D model one can do the basic design of the resonators, such as to find the layer thicknesses that yield the desired resonance frequency, to optimize the layer stack for effective coupling coefficient, estimate the reflector-limited Q-value, etc. Practically all BAW resonator design starts with the 1-D model.

The 1-D model can be applied for longitudinal as well shear waves by just using the material parameters for the appropriate wave mode.

In Fig. 11, the at-resonance displacement, stress, and strain fields in a 932 MHz ZnO resonator with a $\mathrm{W} - \mathrm{SiO_2}$ reflector are shown. Such a resonator structure was studied in Papers 3 and 4. The half-wave resonance contained in the electrodes and the piezolayer (three leftmost layers) and the suppression of the amplitude towards the substrate (right) is evident.

3.2 Reflector Design by Transmission Line Analogy

In the reflector based resonators, it is instrumental to optimize the reflector structure in order to fabricate high performance devices. The simplest way of designing the acoustic Bragg reflector for a longitudinal mode resonator is to set the thickness of each reflector layer to be of a quarter of an acoustic wavelength, i.e.,

$$t_{\lambda/4} = \frac{v_{\mathrm{L}}}{4f_0}, \tag{52}$$

where v_{L} is the longitudinal bulk acoustic wave velocity and f_0 is the targeted operation frequency. This provides maximal reflection for a pure plane wave of frequency f_0 arriving at the reflector. To find out what the coefficient of reflection and bandwidth of operation of the reflector actually are, one can utilize an analogy to electrical transmission lines [11, 35]. One can use the expressions for electrical transmission lines for calculating the reflection and transmission of vertically propagating bulk acoustic plane waves in a 1-D layer stack simply just by replacing the electrical wave propagation parameters (impedance, wave velocity) by the acoustical ones.

A single section of transmission line of length t, acoustic impedance Z_c and sound propagation velocity v, terminated to an acoustic impedance Z_b is presented in Fig. 12. The impedance Z_a seen by an acoustic plane wave arriving from infinite half-space on the left is

$$Z_a = Z_c \frac{Z_b \cos(\beta t) + jZ_c \sin(\beta t)}{jZ_b \sin(\beta t) + Z_c \cos(\beta t)}, \tag{53}$$

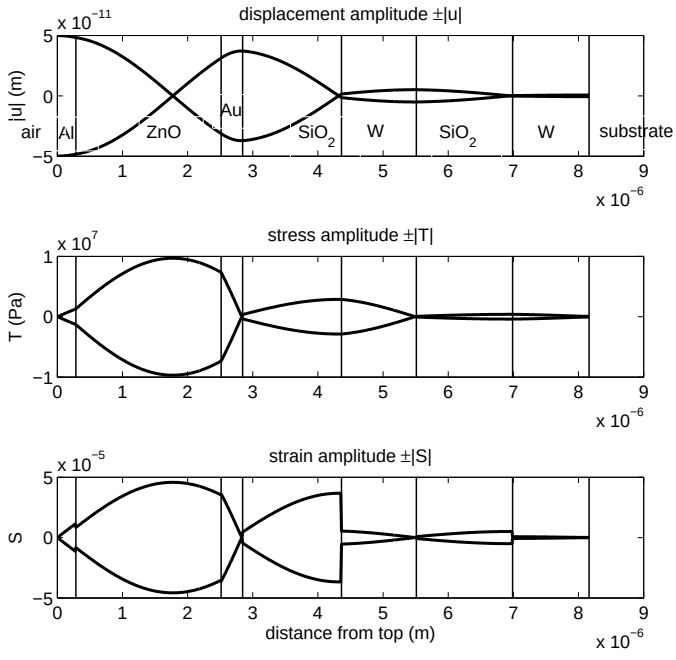

Figure 11: Displacement, stress, and strain amplitudes on a 932 MHz ZnO SMR calculated by the 1-D model at the series resonance frequency f_s. Air interface is on the left and substrate on the right. The layers are separated by vertical lines. The three leftmost layers are the top electrode, the piezolayer, and the bottom electrode, respectively.

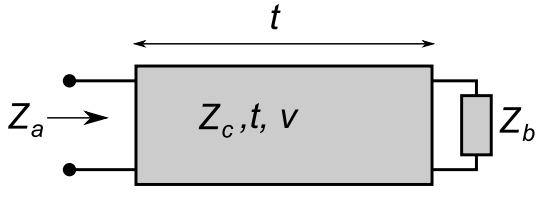

Figure 12: Transmission line principle for calculating the properties of an acoustic Bragg reflector.

where the wave number is given by

$$\beta = \frac{2\pi f}{v}. \tag{54}$$

Here Z_b may be a constant acoustic impedance if the termination is to an infinite half-space (or a thick substrate with a rough backside in practice), or to a

frequency dependent impedance of another transmission line structure. Equation (53) can be used iteratively to obtain the impedance seen by a plane wave incident upon a series of an arbitrary number of transmission line sections (i.e. thin film layers) by using the Z_a obtained in the previous step as a new terminating impedance Z_b. Having calculated the impedance Z_a for a layer stack, one can then calculate a reflection coefficient for a bulk plane wave arriving from an infinite half space having an acoustic impedance Z_{ref} from

$$r = \frac{Z_a - Z_{\mathrm{ref}}}{Z_a + Z_{\mathrm{ref}}}. \tag{55}$$

In the process of designing an acoustic Bragg reflector, the impedance Z_{ref} can be chosen to be either the impedance of the bottom electrode, or if the bottom electrode itself is considered to be a part of the reflector itself, the impedance of the piezolayer. It is to be noted that the same procedure allows calculating the transmission characteristics for longitudinal and shear waves by just choosing the appropriate propagation parameters (acoustic impedance and wave velocity). In [36] Marksteiner *et al.* discovered that the shear reflection characteristics of the Bragg reflector can indeed have profound effects on the Q-value of a longitudinal mode resonator. They also suggest inspecting a logarithmic transmittance of the form

$$T_{\mathrm{dB}} = 10 \log_{10}(1 - |r|^2) \tag{56}$$

instead of the reflection coefficient (55) to resolve small differences important for high-Q resonators. This practice is adopted here.

Comparison of Reflector Layer Stacks

In Table 2, the longitudinal wave acoustic impedance ratios of some typical materials used in the Bragg reflectors of thin film BAW devices are listed. Remarkably, W and $\mathrm{SiO_2}$ provide an impedance ratio of almost 8. With Mo and $\mathrm{SiO_2}$ one can reach a ratio of 5 while the ones using dielectric materials (AlN, ZnO, $\mathrm{Ta_2O_5}$) as the high-Z material offer ratios of 3 and below.

Transmittances of several different quarter wavelength reflector structures designed for 1 GHz operation frequency are shown in Fig. 13. The material pairs are implicated in the plot legends multiplied by a number indicating the number of layer pairs, $2.5 \times \mathrm{W} - \mathrm{SiO_2}$ for example standing for the layer sequence *substrate* - $\mathrm{SiO_2}$ - W -$\mathrm{SiO_2}$ - W - $\mathrm{SiO_2}$ - *resonator*. The longitudinal wave transmittances are shown in the upper part of Fig. 13 where one can observe that the impedance ratio determines the bandwidth of operation of the reflector, $2.5 \times \mathrm{W} - \mathrm{SiO_2}$ reflector being by far the widest. The shear wave transmittances are shown in the lower part of the plot, showing that most reflectors have a very high transmittance

Table 2: Acoustic impedance ratios of material pairs used in SMR reflectors.

Materials	Z_L-ratio
$\mathrm{W}-\mathrm{SiO_2}$	7.9
$\mathrm{Mo}-\mathrm{SiO_2}$	5.0
$\mathrm{AlN}-\mathrm{SiO_2}$	3.0
$\mathrm{ZnO}-\mathrm{SiO_2}$	2.8
$\mathrm{Ta_2O_5}-\mathrm{SiO_2}$	2.4

for shear waves at the operation frequency. The $\mathrm{ZnO}-\mathrm{SiO_2}$ reflector forms an exception – significant shear reflectance is provided. The wide shear reflection band of the $2.5\times\mathrm{W}-\mathrm{SiO_2}$ however reaches close to the operation frequency, yielding for possible manipulation of the shear transmission characteristics by slightly deviating from the quarter-wavelength thicknesses [36].

The minimum transmittances at f_0, defining the reflector-limited Q-values for the longitudinal wave show the fact that $2.5\times\mathrm{W}-\mathrm{SiO_2}$, $4.5\times\mathrm{AlN}-\mathrm{SiO_2}$ or $4.5\times\mathrm{ZnO}-\mathrm{SiO_2}$ reflectors can provide roughly equal minimum transmittance at the operation frequency. The $3.5\times\mathrm{Mo}-\mathrm{SiO_2}$ reflector provides a clearly lower minimum transmittance and the $4.5\times\mathrm{Ta_2O_5}$-$\mathrm{SiO_2}$ reflector is inferior to the others. In the shear transmittance plot (lower part of Fig. 13) the $\mathrm{ZnO}-\mathrm{SiO_2}$ stands out with its unique shear isolation property.

The minimum transmittance and thus the reflector-limited Q-value is determined by the number of layer pairs for a given impedance ratio. With a material selection having a lower impedance ratio, one has to use a larger number of layers to obtain a minimum transmittance equal to that provided by materials of higher impedance ratio. When using metals as the high-Z layers, the number must be minimized as they need to be patterned in order to prevent capacitive shunting along the metal layers. When using dielectrics only, no patterning is needed and it may be economical to deposit even a large number of layers. As will be discussed later, the transmittance of the reflector, however, does not alone determine the resonator performance.

The Q-value of a resonator is defined by [28]

$$Q=\omega_0\frac{E_{\mathrm{tot.,stored}}}{P_{\mathrm{loss,ave.}}}, \tag{57}$$

where $E_{\mathrm{tot.,stored}}$ is the total energy stored in the resonator and $P_{\mathrm{loss,ave.}}$ is the average loss power. If the losses are for example only in the form of energy transmitted to the substrate described by transmittance T, the Q-value takes the

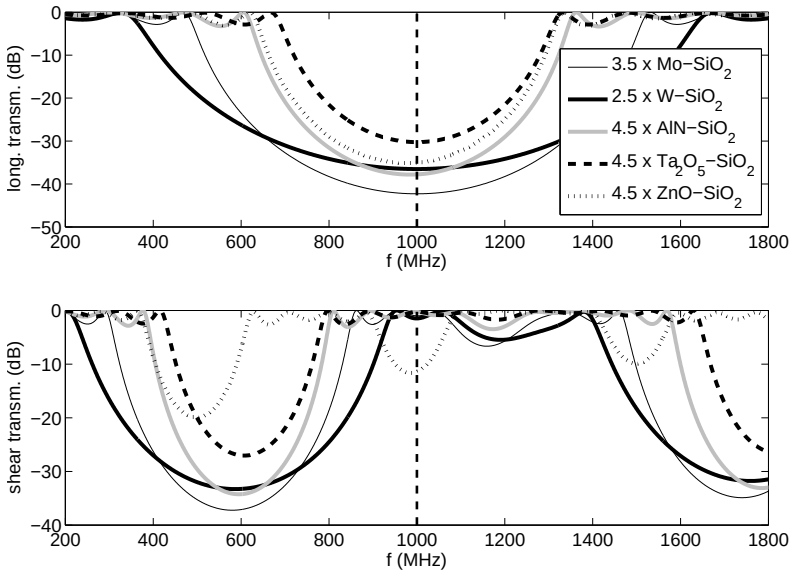

Figure 13: Transmittances (56) for longitudinal (top) and shear waves (bottom) for longitudinal mode quarter-wavelength reflectors of different materials. The $2.5 \times \mathrm{W} - \mathrm{SiO_2}$ reflector provides by far the widest bandwidth due to highest impedance ratio, the next widest being the $3.5 \times \mathrm{Mo} - \mathrm{SiO_2}$ reflector. The all-dielectric reflectors have clearly smaller bandwidths due to smaller impedance ratio. The $\mathrm{AlN} - \mathrm{SiO_2}$ and $\mathrm{ZnO} - \mathrm{SiO_2}$ reflectors with 3.5 pairs reach the same minimum transmittance as the $2.5 \times \mathrm{W} - \mathrm{SiO_2}$ reflector, while the $3.5 \times \mathrm{Mo} - \mathrm{SiO_2}$ is superior and $4.5 \times \mathrm{Ta_2O_5}$-$\mathrm{SiO_2}$ would require a layer pair more to reach the same level. For the shear waves, all but the $3.5 \times \mathrm{ZnO} - \mathrm{SiO_2}$ reflector show high transmissivity. However, the shear band edge of the $2.5 \times \mathrm{W} - \mathrm{SiO_2}$ reflector is near the operation frequency.

Table 3: Comparison of $2.5 \times \mathrm{W} - \mathrm{SiO_2}$, $5.5 \times \mathrm{Ta_2O_5} - \mathrm{SiO_2}$ and $5.5 \times \mathrm{Pt} - \mathrm{Ta_2O_5} - \mathrm{SiO_2}$ reflectors.

stack	k_{eff}	Q
$\mathrm{W} - \mathrm{SiO_2}$	0.2233	5500
$\mathrm{Ta_2O_5}$-$\mathrm{SiO_2}$	0.2159	5130
$\mathrm{Pt} - \mathrm{Ta_2O_5}$-$\mathrm{SiO_2}$	0.2228	6250

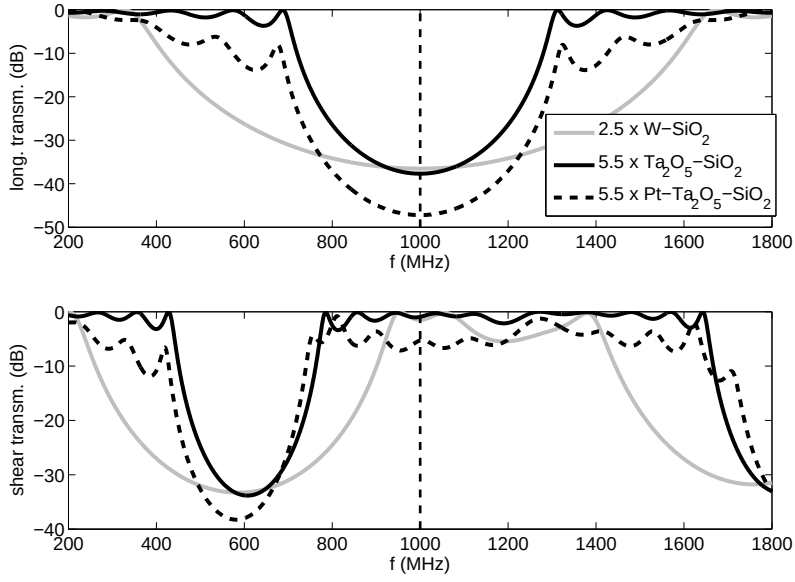

Figure 14: Calculated transmittances of $2.5 \times \mathrm{W} - \mathrm{SiO_2}$, $5.5 \times \mathrm{Ta_2O_5} - \mathrm{SiO_2}$ and $5.5 \times \mathrm{Pt} - \mathrm{Ta_2O_5} - \mathrm{SiO_2}$ reflectors. The bandwidth of the $5.5 \times \mathrm{Ta_2O_5} - \mathrm{SiO_2}$ reflector can be seen to be narrower than that of the $2.5 \times \mathrm{W} - \mathrm{SiO_2}$ reflector, but replacing just the topmost $\mathrm{Ta_2O_5}$ by Pt significantly widens it. The minimum transmittance of the first two are comparable, while the $5.5 \times \mathrm{Pt} - \mathrm{Ta_2O_5} - \mathrm{SiO_2}$ provides over 10 dB smaller transmittance and significantly reduces shear transmittance.

form

$$Q = \omega_0 \frac{E_{\mathrm{tot.,stored}}}{T \cdot E_{\mathrm{tot.,stored}}} = \frac{\omega_0}{T}. \tag{58}$$

This way one can translate the reflector transmittance into a Q-value. From the nature of the Q-value being inversely proportional to relative losses, it follows that

$$\frac{1}{Q_{\mathrm{tot}}} = \sum_i \frac{1}{Q_i}, \tag{59}$$

where the summation is over different loss mechanisms. Now, inspecting a single loss mechanism such as the reflector transmittance, we can interpret the resulting Q-values as the ones that the device would exhibit in case all other loss mechanisms where much smaller in magnitude. We can thus interpret the minimum transmittance resulting from the reflector simulations as the inverse of a 'reflector limited Q-value'.

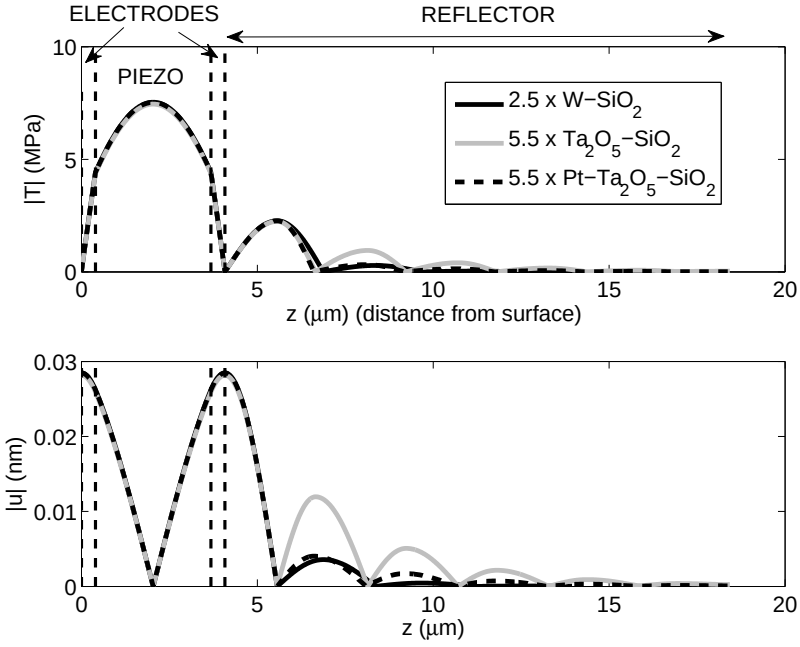

Figure 15: Comparison of acoustic fields at f_s for resonators utilizing a metal $2.5 \times \mathrm{W} - \mathrm{SiO_2}$, dielectric $5.5 \times \mathrm{Ta_2O_5} - \mathrm{SiO_2}$, and a composite $5.5 \times \mathrm{Pt} - \mathrm{Ta_2O_5} - \mathrm{SiO_2}$ reflector. The upper plot shows the stress distribution through the stack while the bottom plot shows the displacement. The all dielectric $5.5 \times \mathrm{Ta_2O_5} - \mathrm{SiO_2}$ reflector shows a much larger vibration outside the resonator (indicated by dashed lines) leading to reduced k_eff. This is in large part remedied by replacing the topmost layer of $\mathrm{Ta_2O_5}$ by Pt.

Hybrid $\mathrm{Pt} - \mathrm{Ta_2O_5} - \mathrm{SiO_2}$ **Reflector**

As an example differing from the mainstream, a reflector combining both dielectric and metal high-Z layers is discussed next.

The BAW technology of Philips Semiconductors (later NXP Semiconductors) used to be based on $\mathrm{Ta_2O_5} - \mathrm{SiO_2}$ all-dielectric reflector motivated by the economy of depositing all the layers in the same vacuum process and avoiding expensive patterning steps [37]. Also, a fully planar substrate is automatically provided for the subsequent resonator fabrication steps. However, neither the Q-value nor the coupling coefficient of the devices were sufficient for the aimed filter application.

In Fig. 14 it is shown that the all-dielectric $5.5 \times \mathrm{Ta_2O_5} - \mathrm{SiO_2}$ reflector provides a minimum transmittance comparable to the $2.5 \times \mathrm{W} - \mathrm{SiO_2}$ metal solution. However, the effect of transmittance on Q is not the only role that the acoustic

reflector has on the electrical performance of the resonator. As is already evident from the fact that more layer pairs are needed for lower acoustic impedance ratio materials, the vibration penetrates deeper into the reflector before being extinguished. This has a direct effect on the effective electromechanical coupling k_{eff} of the resonator. As concluded in Section 2.4, all the vibration energy outside the piezolayer sandwiched between the electrodes cannot contribute to the k_{eff} and thus reduce it. Thus, for maximizing the coupling coefficient of the resonator it is crucial to provide the reflection of the acoustic energy as near the resonator itself as possible.

Instead of completely switching to metallic high-Z layers, only the top-most high-Z $\mathrm{Ta_2O_5}$ can be replaced by platinum, a material already being used in the process for the bottom electrode, to form a hybrid metal-dielectric reflector involving only a single additional lithography step. Platinum as a high-impedance material provides an impedance ratio of 5.3 with $\mathrm{SiO_2}$. The performance improvement is clear in the prediction by the 1-D model shown in Table 3, where the $\mathrm{W-SiO_2}$ reflector provides a benchmark. Both the coupling coefficient and reflector-limited longitudinal wave Q-value are improved to values comparable with the $\mathrm{W-SiO_2}$ reflector. In order to facilitate comparison, simulations have been carried out with identical hypothetical resonator structures on top of the varied reflectors – symmetric 400 nm thick Mo electrodes and a 3.28 $\mu\mathrm{m}$ AlN piezolayer.

In the transmittance plots of Fig. 14, it can be observed that the hybrid $\mathrm{Pt-Ta_2O_5-SiO_2}$ reflector provides a clearly wider bandwidth than the all-dielectric reflector for longitudinal waves and that there is significantly reduced transmittance for the shear waves, too. The minimum transmittance is actually improved from the all-dielectric case and also as compared to the $\mathrm{W-SiO_2}$ benchmark. Results of a one-dimensional simulation of the vibration amplitude (stress and displacement) in the layer stacks are shown in Fig. 15, where the reason for the reduced coupling coefficient of the all-dielectric solution stands out as higher vibration amplitude in the reflector, outside the volume enclosed between the electrodes.

The BAW team at NXP Semiconductors further optimized this structure for the shear reflecting properties, the dispersion characteristics, and for the suppression of spurious resonances with the boundary frame method [23] – the work resulted in high performance spurious resonance free BAW resonators exhibiting a Q-value of over 2000 [38].

4 BAW Filters and Resonators

4.1 BAW Ladder Filters

The most commonly used method to build band pass filters from BAW resonators is to use two kinds of resonators shifted to slightly different frequencies (labeled HI and LO for higher and lower frequency resonators, respectively, in the illustrations) and of slightly different area (capacitance), and to connect them electrically in the ladder topology (Fig. 16). Simulated impedances of such individual resonators are shown in the upper part of Fig. 17, and the transmission (S_{21}) of a $3\frac{1}{2}$-stage filter (Fig. 16 c) comprising of such resonators in the lower part. A photograph of an actual ZnO-based 3-stage ladder filter fabricated at VTT for the E-GSM receive band is shown in Fig. 18.

The electrical performance of the individual resonators dictate the filter performance that can be obtained by the ladder filter constructed from them. Most importantly, the effective coupling coefficient of the resonators defines the obtainable flat passband width, as illustrated by simulation in Fig. 19. The resonator coupling coefficients represent a range from AlN quality obtainable from a suboptimal sputtering system and conditions ($k_{\mathrm{eff}} = 0.19$) to an industrial level optimized process ($k_{\mathrm{eff}} = 0.23$). The filter labeled 'overtuned' shows an attempt to generate a passband equal to that obtained with high coupling coefficient resonators with lower k_{eff} resonators by just increasing the frequency shifting between the higher and lower frequency resonators. The flatness of the passband is lost and a dent in the passband is generated. This demonstrates the fundamental limit set by the resonator coupling coefficient bandwidth of the ladder-type BAW filter.

The effect of the Q-value on the filter performance shows in a slightly more subtle way in the shape of the passband. It affects the minimum attenuation of the pass-band and the sharpness of the pass-band corners. The latter is often more critical for fulfilling industrial specifications. A simulation of this effect done by varying Q while keeping k_{eff} fixed is shown in Fig. 20.

Of the performance parameters, the coupling coefficient and the Q-value are of the highest importance for filter applications. A third very important performance criterium for the resonator is the amount of ripple present in the frequency response, a matter discussed in detail in the next sections. It is the optimization of the resonator performance for these three aspects that made possible the application of BAW technology in mobile phones and is also the main focus of this work.

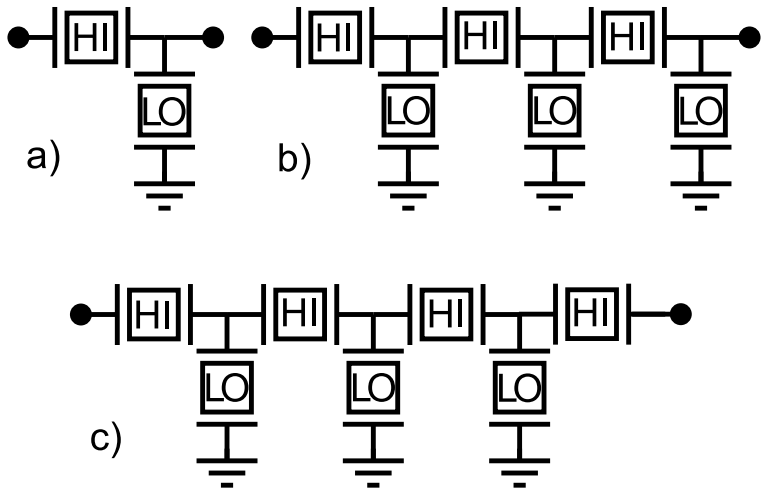

Figure 16: Topology of a ladder filter. The resonators with label HI are the series resonators having a higher frequency and the resonators with the label LO have a lower frequency. a) A single ladder stage forming the basic building block of such filters. b) a 3-stage ladder filter. c) $3\frac{1}{2}$-stage ladder filter.

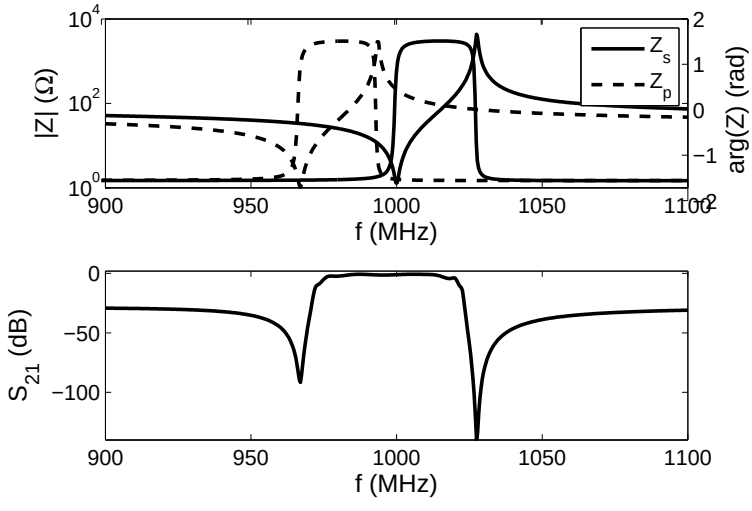

Figure 17: Impedances of individual resonators of a ladder filter (top) and S_{21} of a $3\frac{1}{2}$-stage ladder filter comprising of them. A slight overtuning,i.e. offset between the anti-resonance of the low frequency resonators and the resonance of the high frequency resonators, has been applied.

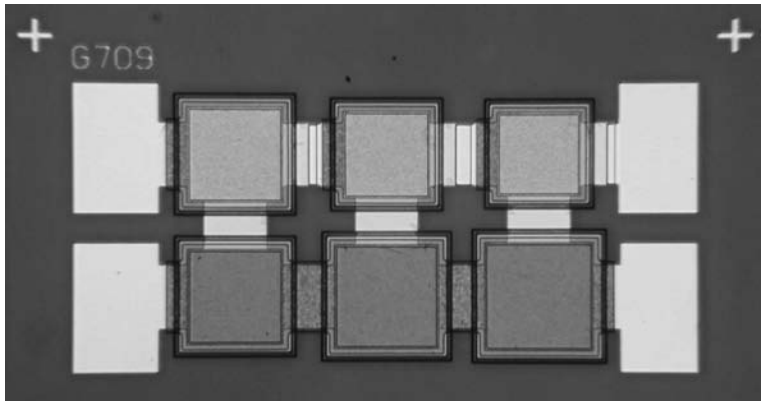

Figure 18: A photograph of a ZnO-based thin film BAW 3-stage ladder filter. The filter is aimed for the E-GSM receive band at 925-960 MHz. The upper row of resonators are the series resonators (HI) and the lower row resonators are the shunt resonators (LO) having a slightly lower center frequency. The width of the filter is roughly 1.5 mm.

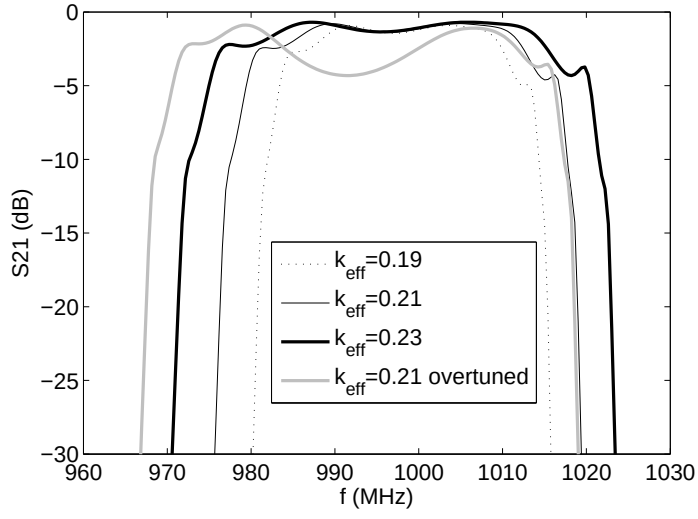

Figure 19: Calculated effect of $k_{\rm eff}$ for filter passband of a 3.5 stage ladder filter. A frequency shift of $1.2 \times (f_p - f_s)$ is applied for the LO resonators except the for the 'overtuned' case, where an attempt to compensate for the non-optimal $k_{\rm eff}$ has been done by a larger frequency shift resulting in a dent at the passband.)

4.2 Response of a Real BAW Resonator and Filter

In Figures 21–22 the measured input impedance of an actual ZnO BAW resonator and the scattering parameter S_{11} (reflection coefficient) are shown together with a

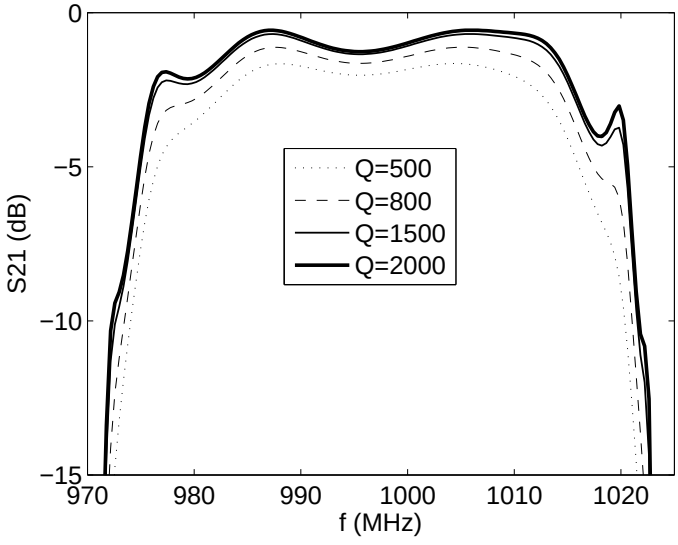

Figure 20: Calculated effect of resonator Q-value for the filter passband of a $3\frac{1}{2}$-stage ladder filter. The increase of the Q-value can be seen to reduce the minimum passband attenuation and make the passband shape more sharp-cornered, which is often most critical for meeting specifications.

1-D simulation result and a fit of the mBvD equivalent circuit to the measurement. The most striking difference of the experimental results to those simulated by the 1-D model and the equivalent circuit fit is the ripple above f_s with a period of a few MHz. Visible at the bottom near the capacitive $50\ \Omega$ point in the Smith chart plot of Fig. 22 are also additional ripples forming small circles.

The magnitude of the impedance (upper plot in Fig. 21) is quite well predicted by the 1-D model, except for the fact that the minimum and maximum values are exaggerated. These are a consequence of unrealistically high Q-values, i.e., low losses in the 1-D model. In the phase plot the same effect is seen as steeper phase transitions at f_s and f_p. Also to be noted is the fact that the phase transitions are equally steep as predicted by the 1-D model, indicating equal Q-values at f_s and f_p. In the measurement, Q at f_s is lower due to a significant series resistance absent in the 1-D model.

The mBVD circuit fitted to the measurement shows a good match to the magnitude of Z_in. The spurious undulations are almost within the linewidth of the plot. However, in the phase of Z_in the unability of the single resonance mBVD-circuit to follow the spurious response is clearer. In the Smith chart plot of Fig. 22 it can be seen that the 1-D model that overestimates the Q-values forms an unrealistically large circle, while the mBVD fit neatly encircles the measured curve so that

the spurious dips deviate only towards the center of the Smith chart.

There is one type of ripple present in the SMR type resonators that the 1-D model can explain: the so called backside reflections which result from standing wave resonances within the full thickness of the substrate. This effect is discussed in Paper 2.

The other type of ripple present in both SMR and FBAR type devices responsible for that present in Figs. 21–22 is typically a stronger effect. There the frequency spacing is not constant, depends on the the lateral shape of the resonators, and decreases with increasing lateral dimensions of the resonator. This ripple is caused by laterally standing wave resonances – a phenomenon associated with lateral propagation of plate wave or Lamb wave modes [39, 40, 23, 41]. Understanding the origin and being able to suppress these lateral spurious modes has been one of the major issues in the successful development of thin film BAW resonator filters for commercial use in mobile phones. The origin of the spurious modes, a method for their suppression, and simulation techniques are discussed in Section 5 and in Paper 4. To underline the importance of effective suppression of the spurious modes, Fig. 23 shows the measured transmission characteristics of two filters, one being constructed of resonators with ripple free responses and the other one suffering from significant spurious resonances.

A measured wide band response from extending from 50 MHz to 5 GHz is also presented in Fig. 24 (thick line). A total of 10 resonances are observed, two below (very close to each other) and 7 above the fundamental resonance. All of these are thickness resonances in nature that are readily predicted by the 1-D model (dashed line). There is some deviation in the predicted and observed resonances, especially towards the higher frequencies. This is due to inaccuracies in the thicknesses and material parameters of the layers. A method for extracting elastic material parameters for the thin films is presented in Paper 1.

The discrepancy in the background levels of $|Z_{\mathrm{in}}|$ and $\arg(Z_{\mathrm{in}})$ is due to a series inductance present in the actual devices.

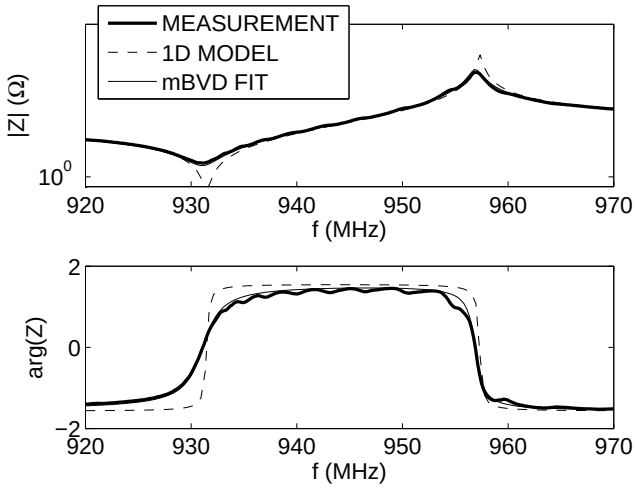

Figure 21: Measurement, 1-D model prediction, and equivalent circuit fit of the input impedance (magnitude and phase) of a ZnO BAW resonator. The measurement shows ripple caused by the spurious lateral resonances and reduced Q-values, especially so at f_{s}, as compared to the 1-D model.

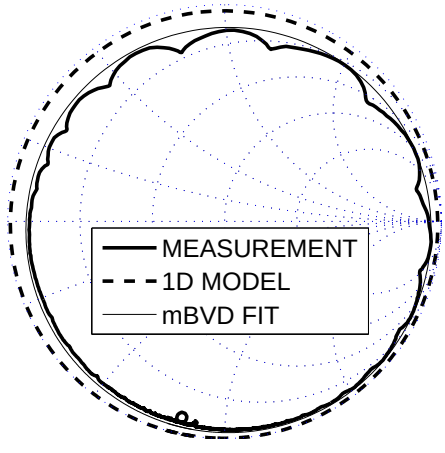

Figure 22: Measurement, 1-D model prediction, and equivalent circuit fit of the reflection coefficient S_{11} of a ZnO BAW resonator on the Smith chart. Measurement shows the undulation caused by the spurious resonances while the 1-D model predicts a clean circle, the radius of which is larger than that measured due to higher Q. The equivalent circuit fit encloses the measurement tightly.

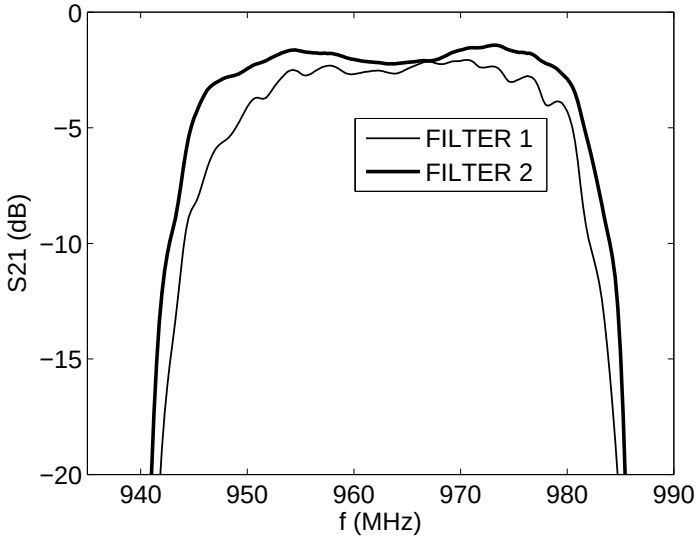

Figure 23: Measured transmissions (S_{21}) of two 3-stage ladder filters such as the one shown in Fig. 18. Filter 1 (thin line) has strong spurious resonances and a low Q-value, whereas Filter 2 (thick line) has weak spurious resonances and a high Q-value.

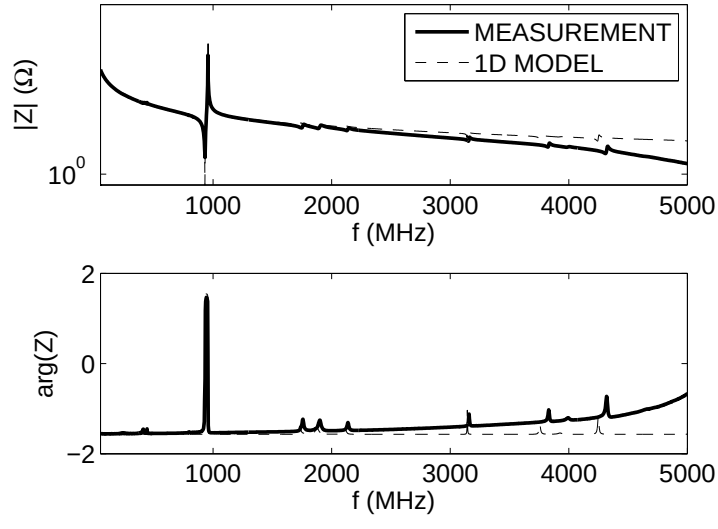

Figure 24: Wideband measurement and 1-D simulation of the input impedance of a ZnO BAW resonator showing a multitude of thickness resonances in addition to the main resonance at 930 MHz. The 1-D model (dashed line) predicts all resonances observed in the measurement, but with some deviation in actual frequencies.

5 Lateral Effects in Thin Film BAW Resonators

Ideally, one would like a BAW resonator to be practically one-dimensional in its operation and use the lateral dimensions only to achieve proper matching to the required impedance level and to tailor the stop band rejection in ladder filters. The practical devices have a width to thickness ratio on the order of 100, but still the finite lateral dimensions and the mechanical boundary conditions at the edges do have profound effects on the resonator performance. First, the vibration needs to be trapped within the resonator in the lateral dimensions as well as in the vertical direction. Otherwise a high-Q resonance is not supported. Secondly, the ripple caused by lateral resonances needs to be suppressed in order to obtain clean frequency response. Both of these issues are connected to the fact that acoustic vibration excited in the thickness direction of the resonator can propagate laterally as plate waves. The understanding and controlling of the lateral propagation characteristics of the plate waves, i.e. plate wave dispersion, plays a key role in the design of BAW resonators.

5.1 Plate Waves and Dispersion

A thin film bulk acoustic wave resonator consists essentially of a stack of plates with different acoustic properties. Propagation of sound waves in such structures has been studied in detail already since the 19th century in connections ranging from vibrations of the crust of the earth to industrial non-destructive ultrasonic inspection of sheet materials.

In the bulk, three different vibration modes can propagate: a longitudinal mode and two differently polarized shear modes. The longitudinal mode is characterized by compression and elongation in the direction of the propagation, whereas the shear modes consist of motion perpendicular to the direction of propagation with no local change of volume. The propagation characteristics of the three bulk modes depend on the material properties and propagation direction respective to the crystal axis orientations. For a discussion of bulk propagation characteristics, see for example [21] and [24]. In the following, we limit the discussion to one longitudinal and one shear mode for simplicity.

When a propagating bulk wave encounters an interface with another material with different material properties, transmitted and reflected waves are generated. In such an event, a pure bulk mode is reflected as a pure bulk mode of the same type only in exact normal incidence [28]. Generally, the stress and particle continuity conditions at the interface require an incident wave to be reflected and transmitted as a combination of all bulk modes propagating in different angles. The phenomenon is called mode conversion and is governed by Snell's Law, which

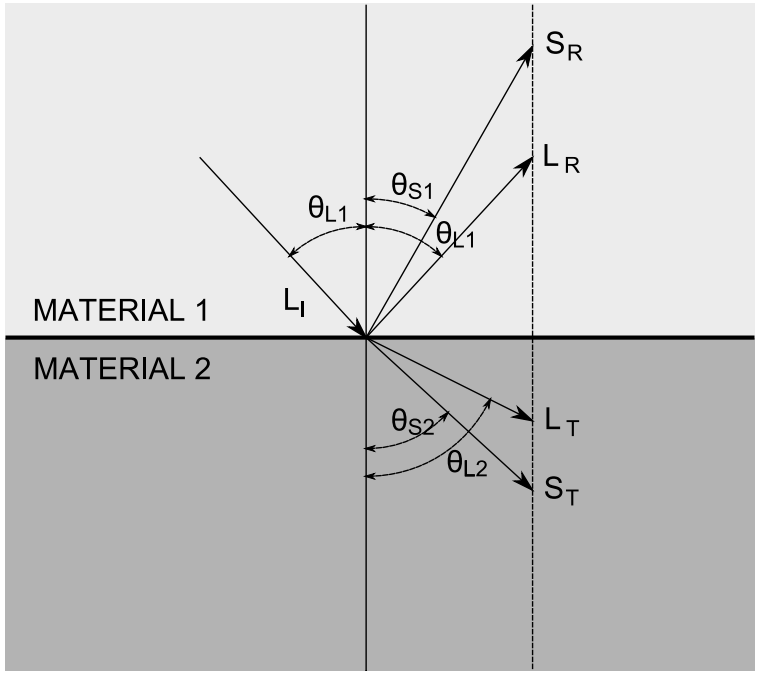

Figure 25: Illustration of the general case of acoustic reflection and transmission/refraction for an interface of two isotropic materials. A longitudinal wave $\mathrm{L_I}$ arrives at the interface with an angle of incidence of θ_{L1} giving rise to a reflected longitudinal wave $\mathrm{L_R}$ with an angle of reflection of equal magnitude θ_{L1}. Additionally, a reflected shear wave $\mathrm{S_R}$ is generated with a different angle of reflection θ_{S1}. Transmitted waves of longitudinal and shear type $\mathrm{L_T}$, $\mathrm{S_T}$ are generated with angles of refraction θ_{L2} and θ_{S2}. The lengths of the arrows represent the wave number. The continuity conditions require that the component of the wave vector along the interface must be equal for all five waves.

for an interface of two isotropic acoustic materials is

$$\frac{\omega}{v_{\mathrm{L1}}}\sin\theta_{\mathrm{L1}} = \frac{\omega}{v_{\mathrm{S1}}}\sin\theta_{\mathrm{S1}} = \frac{\omega}{v_{\mathrm{L2}}}\sin\theta_{\mathrm{L2}} = \frac{\omega}{v_{\mathrm{S2}}}\sin\theta_{\mathrm{S2}}, \tag{60}$$

where ω is the angular frequency of the wave, $v_{\mathrm{L1}}, v_{\mathrm{S1}}, v_{\mathrm{L2}}, v_{\mathrm{S2}}$ are the wave velocities for longitudinal and shear waves in material 1 and in material 2, respectively [28]. The angles $\theta_{\mathrm{L1,S1,L2,S2}}$ are illustrated in Fig. 25. In the case of anisotropic materials, Snell's law takes a more complicated form.

The discussion is limited now to two dimensional structures having one vertical dimension (z) and a single horizontal dimension (x). In a structure formed of a finite number of stacked plates (Fig. 26), pure bulk modes can propagate and form standing wave resonances in the (z)-direction perpendicular to the layer

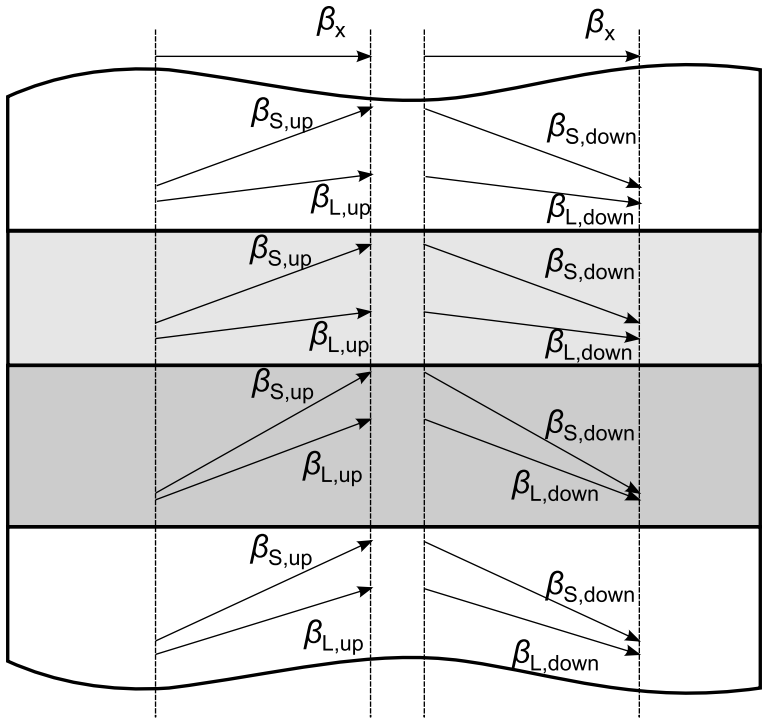

Figure 26: Laterally propagating plate waves in a multilayer stack are formed by such combinations of partial bulk shear and longitudinal waves that can fulfil the continuity conditions at the layer interfaces and boundary conditions at the top and bottom of the stack.

interfaces. If, however, the wave propagation direction of any of the bulk wave components, defined by the wave vector $\vec{\beta}$, deviates from perpendicular, mode conversion according to Snell's law takes place at every interface. It turns out that with certain combinations of propagation directions, repeating mode conversion at reflections at the interfaces reproduces the original field in a periodical manner in the lateral x-direction [28]. This kind of wave modes propagating in the x-direction are called plate wave modes or Lamb waves, some basic types of which are illustrated in Fig. 27 for a single plate. The laterally finite BAW resonator operation is actually defined by the characteristics of these waves as such a resonator practically never can really resonate in a pure bulk wave mode. The presence of laterally propagating waves in vertically stacked layer structures has the important consequence that the operation of the intended vertical-mode resonators becomes sensitive to the lateral boundary conditions and geometry of the device as reflections of these waves from lateral discontinuities will occur.

It is of crucial importance to be able to simulate and measure the lateral propagation characteristics, i.e. the plate wave dispersion relations, in the BAW devices

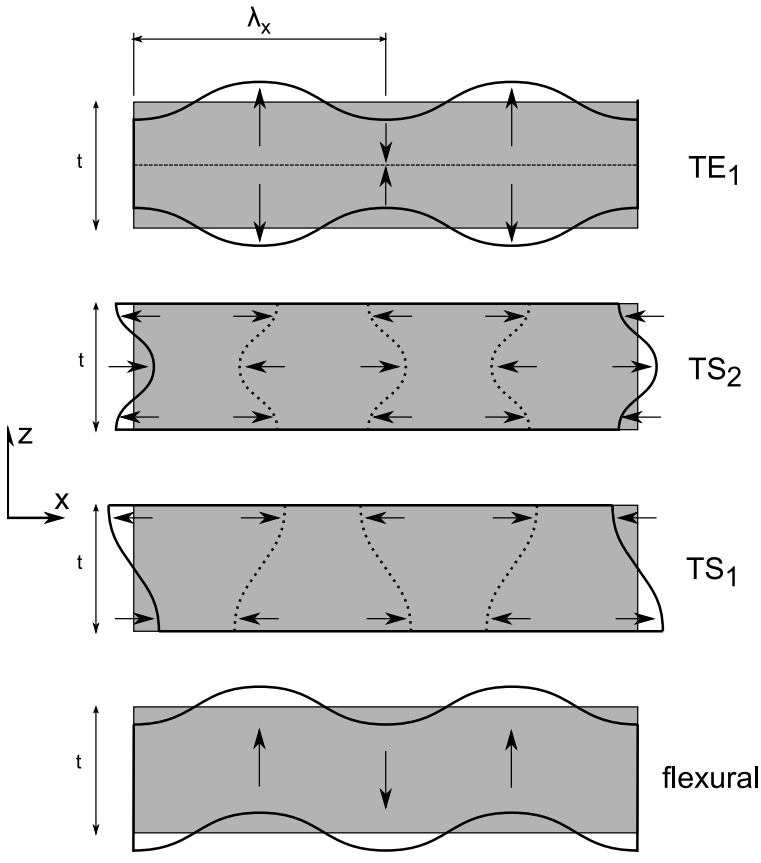

Figure 27: Illustration of some plate wave modes for a single plate: the 1st thickness extensional (TE_1), the 2nd thickness shear (TS_2), the 1st thickness shear (TS_1), and flexural modes, from top to bottom, respectively. Two full lateral wavelengths are shown for each mode. The frequency increases from bottom to top with the exception that the order of TE_1 and TS_2 depends on the Poisson ratio of the plate material.

in order to be able to design high performance devices. The dispersion of the plate wave modes can be calculated for example by matrix methods, some of which are reviewed by Lowe in [42]. In Fig. 28, the dispersion curves calculated by the Thomson-Haskell matrix method (numerical implementation by the author) for a single plate of ZnO are shown. The dispersion curves are presented as a plot of frequency against the horizontal component β_x of the wave vector of the bulk waves, as it is an invariant of the system – at a given frequency all bulk wave components at all layers in solid contact must have the same β_x. This is illustrated in Fig. 26 by the fact that while the wave vectors of partial bulk waves have differ-

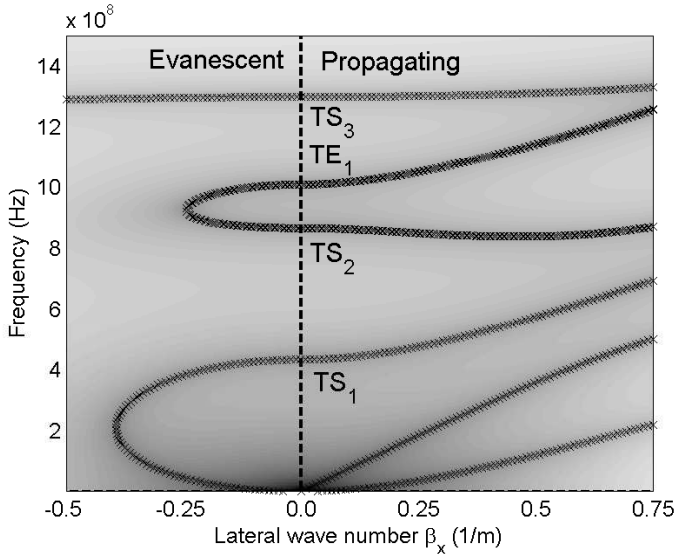

Figure 28: An example of dispersion curves calculated with the Thomson-Haskell matrix method for a single 3 μm thick ZnO plate. The first, second and third thickness shear modes $(\mathrm{TS}_{1...3})$are indicated, together with the fundamental thickness extensional mode (TE_1). See Fig. 27 for the nature of the waves.

ent lengths and directions in layers of different materials, they all share the same x-component and thus lateral wavelength.

The dispersion diagram of Fig. 28 shows the possible combinations of the lateral component of the wave number β_x against frequency as dark lines. It is a typical case that the dispersion curves form smooth continuous lines. The positive values of β_x stand for real valued wave number, but the negative side of the axis is used to represent imaginary values of β_x.

The lateral wave number β_x is real for a laterally propagating loss-less mode. For the plate modes, the out-of-plane component of the displacement at a given level in the layer stack, for example on the surface, is given by an expression of the form

$$u_z = A_z e^{i(\beta_x x - \omega t)}, \tag{61}$$

where A_z is a complex amplitude. For a real valued β_x this is a plane wave propagating in the direction of the x-axis. If, however, β_x is imaginary, say

$$\beta_x = iB, \tag{62}$$

where B is real, we find

$$u_z = A_z e^{-Bx} e^{-i\omega t} \tag{63}$$

which is an evanescent wave. Thus the evanescent branches of the dispersion curves represent non-propagating, non-energy carrying vibration. The evanescent waves have an important role in designing proper boundary conditions in actual devices.

In a loss-less layered structure surrounded by vacuum, the plate modes have either purely real or purely imaginary β_x. However, if viscous losses are present or a wave mode radiates energy into bulk waves of an infinite half-space at either end of the layer stack, the lateral wave number of the plate modes becomes complex. These modes are no more true loss-less vibration modes but propagating modes the amplitude of which decays unless energy enters the system in a form of an exciting force. Handling of complex wave numbers in dispersion calculation is desirable for assessing the bulk leakage that is indeed present in real SMR type BAW devices, but adds a significant amount of complexity in the calculation. Complex wave number simulations have been employed for example in [43]. In this work, we have limited to pure real or imaginary loss-less wave modes. The approximation is appropriate for practical cases of SMRs with a high-performance reflector.

5.2 Lateral Energy Trapping

In a BAW resonator, the vibration needs to be contained in the resonator volume not only in the vertical direction, where it is done by the Bragg reflector or an air interface, but also in the lateral direction. This can be accomplished by designing the resonator so that at the resonance frequency, and in a sufficiently wide band around it, the surroundings support only an evanescent wave. The method is familiar already from the quartz resonator technology [44].

An important matter to note here is that there are two main types of dispersion that the thickness extensional resonator can exhibit. The first, often called Type I, is exhibited by resonators based on ZnO. There the dispersion curve $f = f(\beta_x)$ of the TE_1 mode is monotonically increasing from the cutoff frequency $f_{\mathbf{cutoff}}$, defined by the frequency at which the dispersion curve crosses to the imaginary side (Fig. 29). This means, quite intuitively, that the shorter the lateral wavelength, the higher the frequency. In such material, the energy trapping can simply be provided by thinning the outside of the resonator to bring the $f_{\mathbf{cutoff}}$-frequency of the surroundings higher than that of the resonator, leading to evanescent wave behavior outside the resonator. The thinning can very simply be done by having a patterned electrode to define the resonator (Fig. 31, left).

It turns out, however, that the other case called Type II dispersion is much more common. Especially the most important material of the thin film BAW technology, AlN, exhibits Type II dispersion. In this case, the TE_1 dispersion curve has a negative slope (Fig. 30) meaning slightly counter-intuitively that the

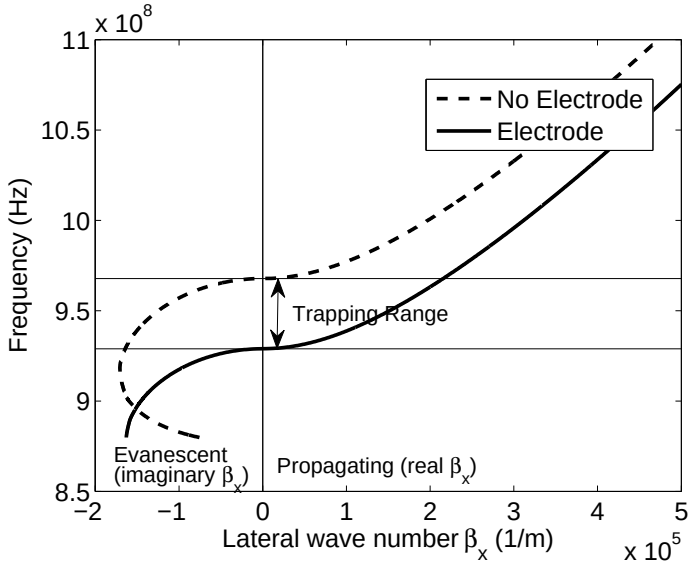

Figure 29: Energy trapping illustrated for a Type I resonator provided by patterned metal electrode. The horizontal lines show the cutoff frequencies for the electroded and non-electroded areas.

frequency increases when wavelength decreases. In order to bring evanescent wave behavior to the outside region for such a resonator actually would means thickening or mass loading the outside area (Fig. 31, right).

Here we have assumed that it is the very same mode inside and outside the resonator that will with an imaginary wave number provide the energy trapping boundary condition. This is the case when the thickness/cutoff offset between the resonator and the outside region is small. If a large step-like discontinuity is created at the resonator edge, it may bring a completely different plate mode of the external region to the resonance frequency range, which may also be used to provide the energy trapping. When the discontinuity is small, the modes in and out are coupled well together since their vertical shape is almost identical. However, in the case of a large step and modes of different nature, the situation is more complex.

The dispersion type for a single plate of certain material is defined by its Poisson ratio, or in other terms, by the ratio of the shear bulk wave velocity to the longitudinal bulk wave velocity $r = v_{\mathrm{S}}/v_{\mathrm{L}}$. If this ratio less than 0.5, the material exhibits Type I dispersion ($r_{\mathrm{ZnO}} = 0.43$), and if it is higher than 0.5, Type II dispersion ($r_{\mathrm{AlN}} = 0.56$). A ratio of exactly 0.5 leads to a special case of equal cutoff frequency for the TE_1 and TS_2 modes.

In Fig. 29 dispersion curves for a simple Type-I structure of Fig. 31 are shown. Energy trapping is provided by the evanescent wave in the non-electroded region

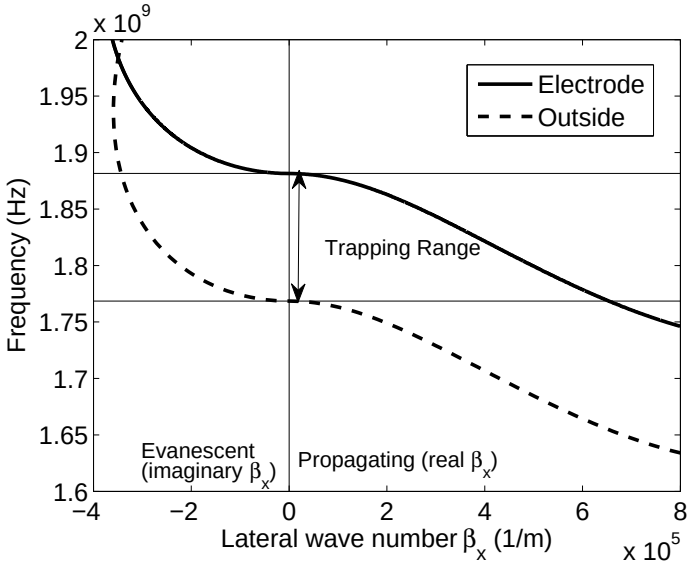

Figure 30: Energy trapping illustrated for a Type II resonator provided by a mass loaded outside region. The horizontal lines show the cutoff frequencies for the electroded and non-electroded areas.

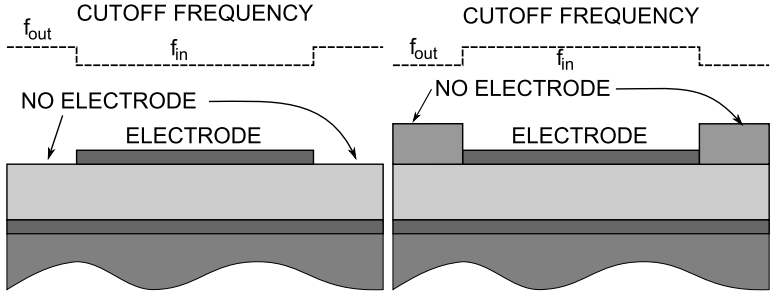

Figure 31: Left: Two region resonator structure of dispersion Type I where the patterning of the electrode provides energy trapping. Right: Two region structure of Type II dispersion where a thickened surrounding is needed for energy trapping.

between the cutoff of the electrode region at about 930 MHz and the cutoff of the non-electroded region at about 970 MHz indicated as 'trapping range'. Below that range, there is no propagating wave either in the electrode or outside it. Above it, the vibration energy is not trapped within the electrode and can radiate to the surroundings – the device does not function as a high-Q resonator but rather as a transducer. In the trapping range, there is in principle a perfect reflection of acoustic energy at the electrode edges, as the evanescent wave outside does not carry energy out of the resonator. Thus, high-Q standing wave resonance modes can

be formed within the electrode with such lateral wavenumbers that can fulfil the boundary conditions. Considering a hypothetical case of having a fixed boundary condition $u_z = 0$ at the resonator edges, the standing wave resonances would occur on the dispersion curve with lateral wave numbers

$$\beta_x = \frac{n\pi}{W}, \quad n = 1, 2, 3, ... \tag{64}$$

with W being the resonator width. In practical devices such a simple boundary condition cannot be realized, and the dispersion characteristics on both sides of the resonator edge must be considered in order to find the lateral resonances. A transfer matrix model developed for this purpose by M. Ylilammi at VTT for a single resonator [34] was adopted for the simulations of Paper 4. The model was further developed to account for the lateral acoustical coupling of adjacent resonators and for calculating harmonic response of such laterally acoustically coupled multiport devices in Papers 5 and 6. An overview of the model is given in the next section. A detailed description of the multi-port model is given in Paper 5.

Only a single plate wave mode inside and outside the resonator has been considered here. In reality, there are always other modes with real wave number of higher magnitude present at any frequency, as is evident from the dispersion diagrams of Figs. 37 and 53. These modes will constitute a loss mechanism and source of additional spurious ripple.

5.3 2-D Modeling of BAW Resonators

It is assumed that the vibration modes of a resonator structure consisting of several lateral regions i with known dispersion relations can be presented by an out-of-plane displacement of the form

$$u_i(x_i) = A_i e^{-j\beta_i x_i} + B_i e^{j\beta_i x_i}, \tag{65}$$

where A_i and B_i are the amplitudes of right and left propagating waves, respectively, β_i is related to frequency by the known dispersion relations $\beta_i = \beta_i(f)$. By requiring continuity of the displacement u_i and its derivative $\frac{\partial u_i}{\partial x_i}$ (stress) over the region boundaries, one can form a transfer matrix

$$\begin{bmatrix} A_{i+1} \\ B_{i+1} \end{bmatrix} = M_i \begin{bmatrix} A_i \\ B_i \end{bmatrix} \tag{66}$$

to relate the displacement amplitudes in adjacent regions. This allows for a numerical solution of the laterally standing wave resonances $u_p(x)$ of the structure. The set of eigenmodes $u_p(x)$, p indexing the modes by eigenfrequency ω_p, is used

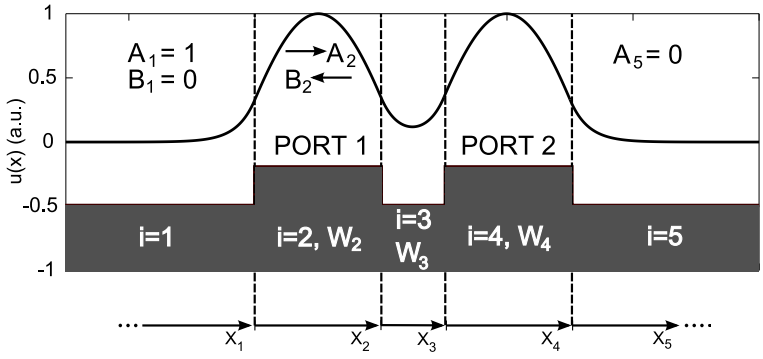

Figure 32: Illustration of an exemplary 2-D model geometry for a five region acoustic device having two electrical ports. The gray area at the bottom reflects the topology: the elevated regions $(i = 2, 4)$ have electrodes and their dispersion characteristics are described by the curve labeled 'Electrode' in Fig. 29, whereas the other regions $(i = 1, 3, 5)$ are described by the curve labeled 'No Electrode'. The electroded region 2 is defined to form the electrical port 1 and region 4 port 2. The boundary conditions for the amplitudes of the energy trapped modes are shown.

as a basis function set to describe the harmonic response of the system. In Fig. 32 an exemplary five-region resonator illustrating the model setup is shown. It is to be noted that within this model, the eigenmodes depend only on the dispersion characteristics and geometry of the regions, while the electrical drive conditions can be freely set by simply choosing regions that represent the electrodes. Several electrical ports can be considered simultaneously.

The electromechanical coupling coefficient k_p of a mode u_p can be calculated with respect to a driving voltage present at regions i that belong to an electrical port m from

$$k_{p,m}^2 = k_{1\mathrm{D}}^2 \frac{\left| \sum_{i \in \text{port } m} \int\limits_{W_i} u_p(x)\, dx \right|^2}{W_{x,\text{port } m} \int\limits_{-\infty}^{+\infty} |u_p(x)|^2\, dx}, \tag{67}$$

where $k_{1\mathrm{D}}$ is the effective coupling coefficient of the resonator obtained from 1-D simulation, $W_{x,\text{port } m}$ is the total width of the electrode(s) belonging to port m. Equation (67) follows from (35) with the assumption of constant electric field over the electrode of port m.

Having solved the eigenmodes u_p and their coupling coefficients, assuming realistic Q-values for the modes (Q-values do not emerge from this model), one can calculate the harmonic response of the system as an eigenmode superposition.

Furthermore, this can be done considering any defined region or set of regions acting as the driving electrical port allowing for simulation of the characteristics of an N-port device with acoustic coupling between the ports. The detailed derivation of the harmonic response is presented in Paper 5 while the main results are summarized below.

The harmonic vibration response of the device to a driving voltage V present at port m of the device is

$$u_{x,m}(x,\omega) = \sum_p \alpha_{p,m} F_p(\omega,\omega_p) u_p(x), \tag{68}$$

where $F_p(\omega,\omega_p)$ is the shape of the modal frequency response

$$F_p(\omega,\omega_p) = \frac{1}{1+\frac{Q_p(\omega_p^2-\omega^2)}{j\omega\omega_p}}, \tag{69}$$

from (18) and $\alpha_{p,m}$ is the modal superposition coefficient

$$\alpha_{p,m} = \frac{V K_{p,m}^2 Q_p W_{x,\text{port }m}\varepsilon^S}{je\int_{W_{\text{port }m}} u_p(x)\,dx}. \tag{70}$$

Here Q_p is the Q-value associated to mode u_p, V is the driving voltage, $K_{p,m}^2 = k_{p,m}^2/(1-k_{p,m}^2)$ is the coupling of mode p to port m, $W_{x,\text{port }m}$ is the total width of the electrodes of port m, and e and ε^S are the piezoelectric stress coefficient and the permittivity of the piezolayer, respectively. Integration is over all electroded regions belonging to port m.

On the other hand, if one knows the vibration response $u_{x,m}(x,\omega)$ resulting from a harmonic driving voltage V at port m, the current trough port n is obtained from

$$I_{nm} = j\omega V C_{0,n}\delta_{nm} + \frac{j\omega e W_{y,n}}{t}\int\limits_{W_{x,n}} u_{x,m}(x,\omega)\,dx. \tag{71}$$

Here $C_{0,n}$ is the plate capacitance formed by port n, W_y is the width of the electrode in the truncated dimension and t the thickness of the piezolayer. The driving voltage V is assumed to be zero at all other ports than the driving one (hence the Kronecker delta δ_{mn}), i.e., they are short circuited. This allows for the extraction of the N-port Y-parameters of the device

$$Y_{nm} = \frac{I_{nm}}{V_m}. \tag{72}$$

This constitutes a full electrical description of the acoustic device with multiple acoustically coupled electrical ports

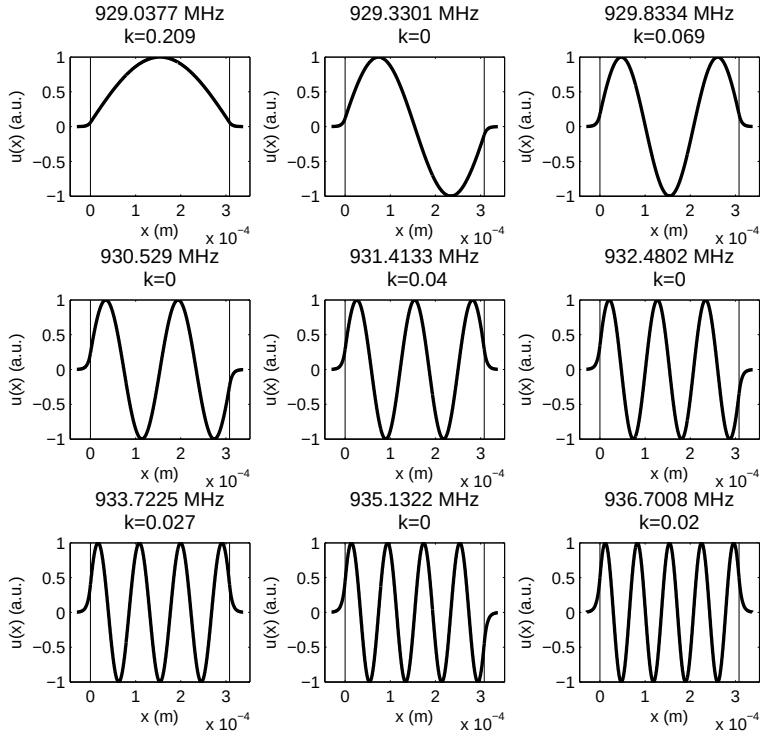

Figure 33: The first 9 eigenmodes of a simple ZnO resonator where only the electrode is patterned to be 308 μm wide. The large width of the resonator leads to closely spaced resonance modes. The coupling to the antisymmetric modes is zero.

As an example, the first 9 eigenmodes of a 932 MHz one-port resonator such as the one presented in Fig. 31 are shown Fig. 33. In total, such a wide resonator supports a total of 22 eigenmodes in its trapping range, of which 11 are symmetric and have non-zero coupling. The energy trapping is evident from the exponentially decaying vibration amplitude at the outer regions. In Fig. 34, the eigenfrequencies of an otherwise identical but only 150 μm wide resonator are indicated on the dispersion diagram and on the input impedance obtained from the harmonic response calculation. It can be seen that the eigenfrequencies corresponding to symmetric modes coincide with local minima in the impedance while the antisymmetric ones do not affect it. The smaller width of the resonator has been chosen in order to make the spurious ripple spectrum more sparse for illustrative purposes.

The described 2-D model gives a strongly simplified picture of the resonator. It

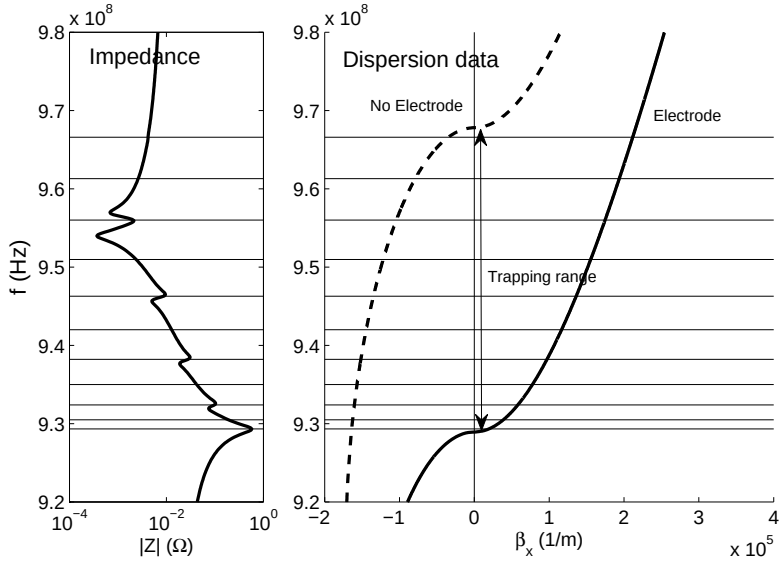

Figure 34: Calculated eigenmode frequencies (horizontal lines), dispersion diagram (right), and magnitude of input impedance (left) of a simple ZnO resonator where only the electrode is patterned to be 150 μm wide. A total of 11 modes are supported in the trapping range between the dispersion curves. The eigenfrequencies of the symmetric modes are associated with local minima in the impedance.

considers only the vertical displacement of a single plate mode, and is based on the requirement of continuity of the displacement and its first derivative. This limits its applicability to structures with only small discontinuities between the lateral regions. It omits the fact that proper continuity conditions should be dealt with along the vertical interface between regions through the entire layer stack, as is done by Milsom *et al.* in [43]. It is expected that this model is not realistic enough for example in the case of heavy electrodes causing large acoustic discontinuity at the edges. The advantage of the this 2-D model is that it is very fast and intuitive and it has shown its usefulness in rough analysis of the principles of the device operation. The 2-D model can also be extended to two lateral dimensions with the aid of numerical eigenmode solution [45].

5.4 FEM Modeling of Thin Film BAW Devices

Fully numerical solution of electro-acoustic equations by for example the Finite Element Method (FEM) allows one to abandon many of the simplifying assumptions used in the 1-D and 2-D models discussed in Sections 3.1 and 5.3.

In Papers 3 and 4, the finite element software developed specifically for the

thin film BAW acoustic devices by T. Makkonen *et al.* (Materials Physics Laboratory, Helsinki University of Technology) called BAWFEM [46] was used.

Advantages of FEM over the simpler models are numerous. First of all, more realistic resonator geometries can be modeled. A FEM model also intrinsically contains the dispersion characteristics for all plate modes that the applied element mesh can represent. The vertical boundaries between regions of the resonator having different layer stacks are handled naturally without simplifying assumptions, even in the case of large discontinuities. The electrical excitation can be defined realistically and the effects of the fringing fields are included. Coupling to different plate modes and shear waves arises naturally. Also, full anisotropy and viscous losses of the materials can be handled. Ohmic losses in the electrodes can also be modeled by FEM [47], but this has not been implemented in BAWFEM nor employed in this work. As will be discussed later, it is actually in the modeling of losses where the greatest difficulties and drawbacks of FEM are encountered.

The computation with FEM becomes easily quite heavy. In the typical models for 1–2 GHz frequency range thin film BAW resonators, the element size needs to be around 1 $\mu\mathrm{m}$ in the lateral direction and even smaller in the vertical direction in order to be able to represent effects related to the high-lateral-wave-number plate modes. While this is fairly easily managed for 2-D models, realistic 3-D modeling becomes extremely heavy.

In Fig. 35 the geometry of a 2-D FEM model of the vertical cross-section of a ZnO resonator employed in Papers 4 and 3 is illustrated. The degrees of freedom to be solved are the displacement components (u_x, u_z) and the electric potential ϕ, for which the boundary conditions have also to be specified.

Symmetry is utilized, so that only the left half of the cross section of the resonator is included in the model. The symmetry condition is applied by setting the lateral displacement to $u_x = 0$ at the symmetry edge. At the top surface, no conditions are set for the displacements, i.e., the surface is free. At the bottom the free condition is also used, but this is realistic for a device sitting on a substrate only when the model is truncated at the lower edge with a high-Z material. This creates a stress node at the interface, which is a good approximation to a free surface. However, no energy at all can leak out of the bottom in the finite model, so the finite reflectivity of the reflector cannot be analyzed by this kind of boundary conditions. At the left edge outside the resonator, the layer structure is truncated at a distance large enough for the exponentially damped tails of wave modes trapped by the electrode to diminish. There both u_x and u_z are clamped to zero. For the trapped wave modes the boundary condition makes no difference, but for the non-trapped high-β_x modes visible in Figs. 37 and 53, it does have a large effect. This is a source of error in the simulations.

The electrical potential ϕ has to be specified in all of the conductors of the model. The excitation is specified via having a harmonic voltage of 1V in the

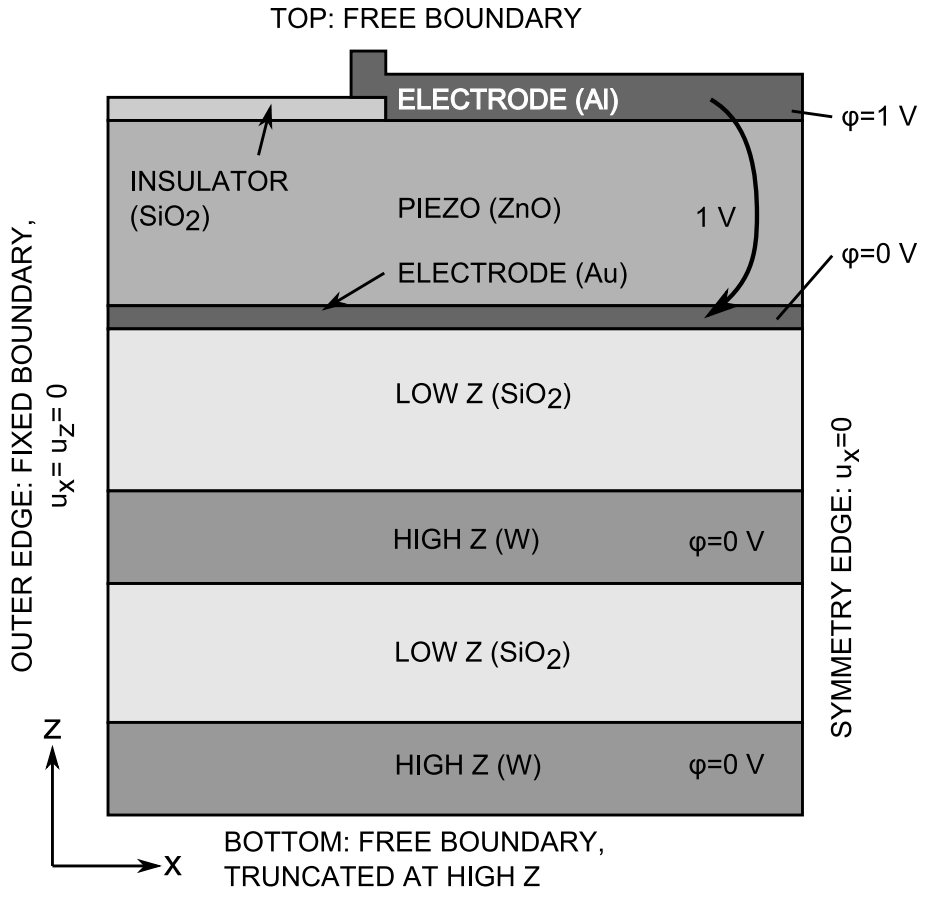

Figure 35: An example of a 2-D FEM model of an ZnO SMR. The model consists of the left half of the resonator, utilizing symmetry condition at the right edge. The boundary condition assumes that there is free space on the top of the resonator as well as at the bottom. Truncating the model at a high-Z layer makes the latter a good approximation to the real situation. At the left edge, i.e. outside the resonator, a fixed boundary condition is used. For wave modes trapped in the electroded region, this boundary condition makes no difference, but for non-trapped waves it is of significance. Excitation is provided by a voltage difference between the electrodes.

upper electrode and the lower electrode grounded. The metals in the reflector are in this case defined grounded but they could as well be left floating with the condition that the potential is constant over any connected metal region.

The material parameters are specified via the stiffness matrix c_{ij}^E, density, dielectric permittivity ε^S, and piezoelectric stress matrix e_{ij}, and a viscosity matrix η_{ij}. If the full anisotropic matrices are not known, an isotropic approximation is

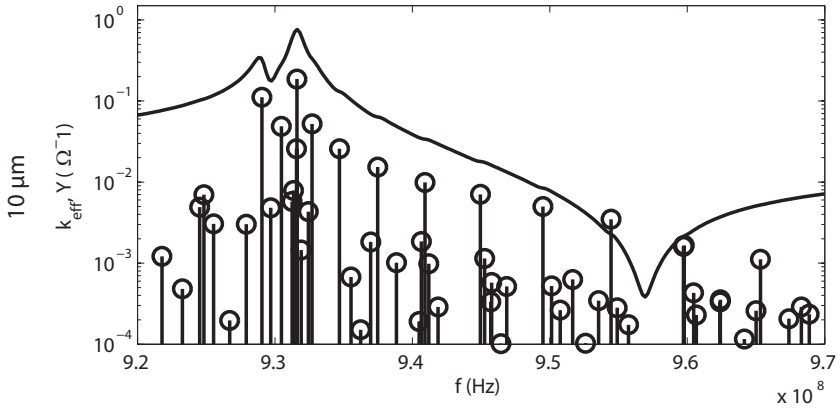

Figure 36: FEM-simulated eigenmode spectrum ($k_{\mathrm{eff},p}$ vs. f_p) and corresponding resonator admittance $Y(f)$ for ZnO SMR model such as the one presented in Fig. 35. The FEM calculation resolves the same modes as the 2-D model but also a large number of additional modes.

easy to construct based on acoustic wave velocities v_L, v_S and density ρ.

There are two methods of solution for the specified FEM problem: In the modal analysis the loss-less eigenmodes of the system are solved and in harmonic analysis the response of the system to harmonic driving (typically voltage applied over the electrodes) at any specified frequency is calculated.

The modal analysis results in free eigenmodes with no attenuation. Each mode is associated with a solution for the field variables $u_x(x, y)$, $u_z(x, y)$, $\phi(x, y)$, and the eigenfrequency ω_p together with a modal constant describing the coupling coefficient of the mode to the specified exciting electrodes. The modal constants are calculated by integrating the accumulated charge over the interface of a specified electrode and the piezoelectric layer for each eigenmode. If one additionally assigns each mode a Q-value (which does not result from loss-less modal analysis), one can via the equivalent circuit analogy extract the harmonic electrical response of the resonator provided that a large enough number of eigenmodes have been solved.

This yields for a computationally efficient method for computing the harmonic response via modal analysis with the drawback that the viscous losses are not incorporated properly. This, however, is not as large a drawback as it may first seem.

In Paper 4, the modal analysis was utilized together with the 2-D model to analyze the spurious resonance suppression in ZnO resonators. An example of a FEM-calculated eigenmode spectrum and the resulting frequency response are

shown in Fig. 36. The 2-D FEM predicts the same strong modes as the 2-D model, but also a large number of additional modes (See Paper 4 for a detailed comparison).

The harmonic analysis incorporates losses via the viscosity of the materials. This improvement over the lossless modal analysis, however, turns out not to be so significant. The Q-value of the typical devices does not seem to be dominated by the viscous losses, and the dissipation properties of the thin film materials at GHz range frequencies are poorly known anyway. The harmonic analysis, however, allows one to calculate the vibration field $\vec{u}(x, y) = [u_x(x, y), u_z(x, y)]$ and the potential field $\phi(x, y)$ at any frequency which corresponds to the actual situation of driving such a resonator under, for example, a vector network analyzer or laser interferometric measurement.

An interesting post-processed result allowed by the harmonic analysis is the extraction of the dispersion characteristics by Fourier techniques in the same manner as for the laser interferometric measurements described in Section 6. An example of such FEM-simulated dispersion characteristics is presented in Fig. 37. This was utilized in Paper 3 for comparing simulation and measurement of the reflector transmission characteristics as function of frequency and wave number.

The most important source of error as compared to real devices comes from the boundary conditions at the model edges. The FEM model is necessarily finite in size, and some conditions must be fixed for the acoustic fields at the outer boundaries. In real devices, some acoustic energy can escape the resonator in the form of acoustic radiation. The finite FEM model on the other hand cannot lose any energy except in viscous dissipation. The acoustic leakage, which is in practice a more important factor for defining the Q-value than the viscous losses, is then not modeled at all leading to unrealistically high Q-values predicted by FEM modeling (unless viscous loss dominates). This problem has been tried to be solved by creating a padding of viscous material around the resonator in an attempt to absorb most acoustic radiation from the active resonator model [48]. A profile ramping the viscosity up over a distance must be used in order not to create reflections from abruptly changing viscosity. In the vertical direction, where the vibration is close to being purely longitudinal, the method has been rather successfully applied. Problems arise when trying to generate a viscous profile in the lateral direction, that would work simultaneously for all wave modes and lateral wavelengths propagating along the layers. This method also makes the models larger and thus computationally heavier.

A special kind of mathematically modified computation element attempting to suppress the boundary reflections called the perfectly matched layer (PML) is available in some FEM simulation software. Mayer *et al.* report in [49] on the usage of the PML in the case of SAW simulation and find it superior to the absorbing boundaries. The simulation of SAW devices is slightly simpler than

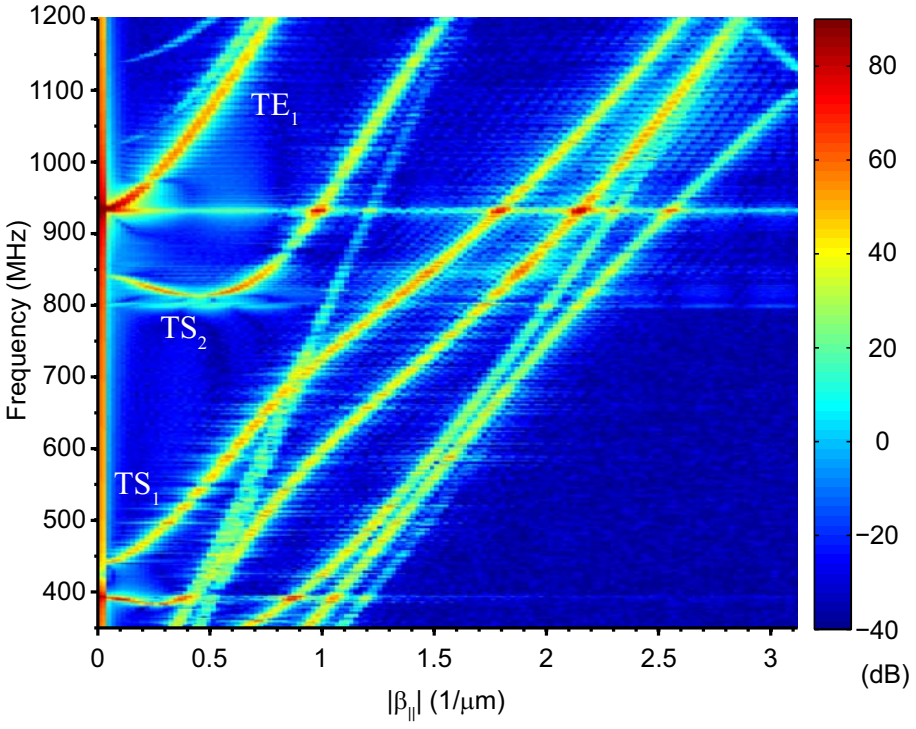

Figure 37: The dispersion diagram calculated from the out-of-plane surface displacement simulated by 2-D FEM harmonic analysis for a ZnO SMR resonator. The first thickness shear (TS_1), second thickness shear (TS_2) and the first thickness extensional (TE_1) mode branches are indicated in the plot.

that of BAW devices since there periodicity can be utilized - the PML needs only be applied in the vertical direction.

A third kind of approach is to use a combination of FEM and the boundary element method (BEM), where the whole substrate or chip can be incorporated as in BEM only the outer boundary of the model is discretized, thus keeping the computational size of the substrate-containing model manageable [50]. The FEM-BEM is, however, computationally much more involved than plain FEM [49]. It also seems that the FEM-BEM is difficult to set up for the lateral edges of the resonator. To the author's best knowledge, no perfect solution exists for the boundary conditions in the numerical simulation of BAW resonators, but the developments related to using the PML seem quite promising.

Despite the difficulties in obtaining high level of realism in the FEM calculation due to the issues discussed above, 2-D FEM has been very useful in the practical work for optimizing resonator performance – mainly in the analysis of spurious resonance behavior. Qualitative agreement with experiment is good enough to fa-

cilitate the use of FEM in a numerical experiment to verify various designs before entering sample fabrication. Often the improvements to the designs have come from simpler ideas and models such the dispersion simulation, or 2-D simulation, and the final test before experiment is performed by FEM.

5.5 Spurious Resonance Suppression

Spurious ripple due to standing wave resonances of laterally propagating plate waves is a direct consequence of lateral energy trapping. A filter constructed of resonators showing such spurious response will have unacceptable ripple in the passband (see Fig. 41).

Several methods exist for manipulating the spectrum of spurious resonances. First, the lateral dimensions affect the spurious spectrum so that the smaller the resonator width, the larger the frequency spacing of the resonances. In principle, the resonator can be made so small that only the principal mode fits in the trapping range. However, for practical applications the required impedance level (typ. 50 Ω) sets a strict requirement for C_0 and thus the area of the resonators making this not an option. Making the resonator size very small would also lead to trade-off in coupling and the Q-value due to a significant fraction of vibration energy lying in the evanescent fields outside the electrode-covered area and increasing perimeter to area ratio, respectively.

Secondly, one can reduce the lateral symmetry of the resonator since obviously the resonances are most pronounced in resonators of high symmetry such as circular or square resonators. In [51], a method of spurious resonance suppression based on symmetry reduction, or 'apodization', is presented. The effect is to make the spectrum of the modes to split into a large number of weakly coupled modes instead of a smaller number of strongly coupled modes. Elliptic shape has also been reported as advantageous for spurious suppression [52]. This has also been studied in [45] by investigating the spurious resonance spectra of ellipses with varying aspect ratio.

A third possibility is to engineer the resonator to have a very flat dispersion profile where all the spurious resonances would be spaced very close to each other in frequency, practically merging together in the electrical response [53], [54]. The dispersion engineering is quite demanding to realize, as there are many optimization goals to be reached simultaneously and not very much freedom in the choices of materials and their thicknesses.

In [23] another method for spurious resonance suppression based on modification of the lateral acoustic boundary condition is presented. This method, the boundary frame method, is very effective provided that the dispersion characteristics of the resonator can be tailored to make it applicable. It is based on modifying the spurious resonance modes so that only the principal mode can couple to the

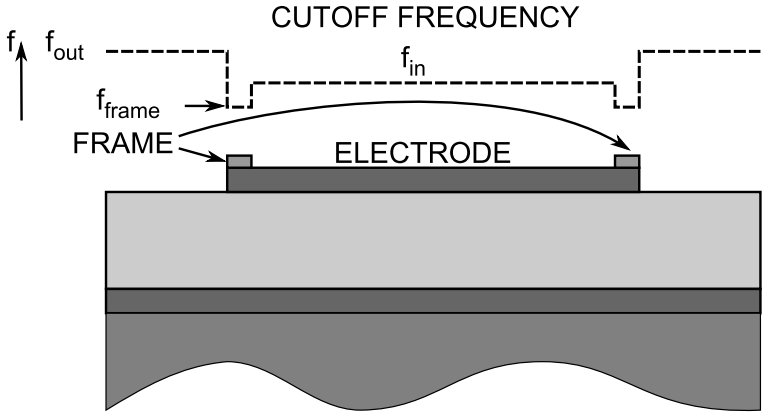

Figure 38: Cross section of a resonator with the boundary frame structure for spurious resonance suppression. The dashed line on top of the resonator shows the cutoff frequency at each region of the resonator.

driving field and the others are extremely weakly coupled to it. A detailed study of ZnO resonators employing this method and comparison to 2-D and 2-D FEM models was conducted in Paper 4 to analyze the boundary frame method in depth.

In the boundary frame method one creates a thickened frame of a certain width (see Fig. 38) with a lowered cutoff frequency at the resonator edge so that a free boundary condition is simulated – the boundary region acts as a matching structure between the resonator and the surroundings. Calculated dispersion characteristics for such a resonator are presented in Fig. 39. As a result, the fundamental mode takes a shape with constant amplitude over the resonator which closely matches to the shape of the driving electrical field. If the higher order lateral modes are orthogonal to the fundamental mode, a property indeed often encountered in eigenvalue problems, the fundamental mode will be the only mode coupled to the driving field.

The boundary frame dimensions have to be optimal for given dispersion characteristics of the outside area, resonator area, and the frame area itself. In Fig. 40 electrical measurements of varying boundary frame widths for a 930 MHz ZnO resonator are shown. A drastic reduction on the spurious ripple is observed for a certain width. Measurements of pass band transmission in filters consisting of similar resonators having a varied frame width are shown in Fig. 41. The advantage of using an optimal boundary frame is evident in the plots labeled 9 μm and 11 μm, indicating the frame width. The resonators of these filters are slightly different in design than those in Fig. 40, thus the difference in frame widths.

The more detailed structure of the resonator of this study was presented in Fig. 6 (left), where it can be seen that the boundary frame is formed by letting the bottom electrode and an insulator layer to overlap slightly.

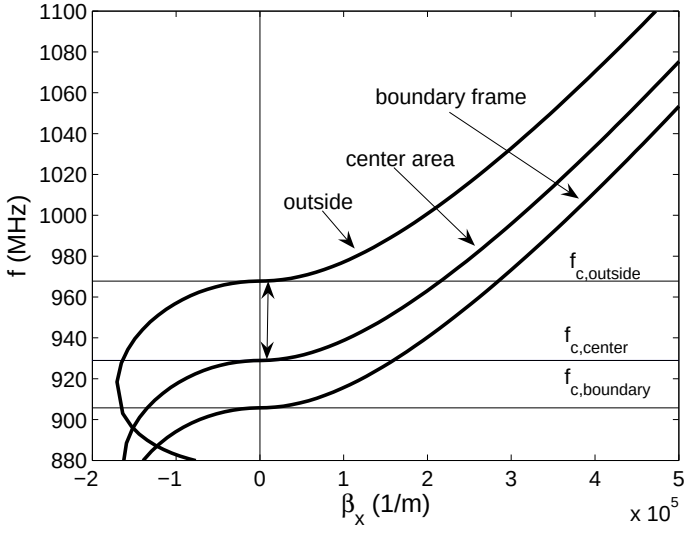

Figure 39: Calculated dispersions for a 930 MHz ZnO resonator utilizing the boundary frame method. The energy trapping range is indicated by a vertical arrow next to the $\beta_x = 0$ axis. The boundary frame supports a propagating wave throughout the trapping range and acts as a matching element between the outside and the resonator center area.

To confirm that the mechanism behind the suppression of spurious resonances is indeed the one described above, the mode spectrum obtained by the 2-D model and 2-D FEM was studied in Paper 4. It was observed that when a piston mode type mode emerges as one of the lateral modes, the coupling of the others is indeed reduced on a wide frequency range. However, the coupling coefficients of the spurious modes do not reduce to zero neither in the 2-D nor the FEM model. A calculation of the inner products among the eigenmodes of the 2-D simulation shows that the modes have a very small level of linear interdependence but no perfect orthogonality. A likely reason for the lack of orthogonality is that the boundary condition for the eigenmodes is not constant over the frequency range due to dispersion but is slightly different for each mode. Another effects was found to affect the spurious mode content. Depending on the frame width, a single mode was strongly suppressed while others were not. It was found that this 'missing mode' effect is due to the frame region and the center region forming for a certain frequency a symmetric modeshape for which the coupling becomes close to zero similarly to the antisymmetric modes. The minimum amount of ripple results from the interplay of the two effects and does not necessarily coincide exactly with the piston mode operation point but is typically very close to that.

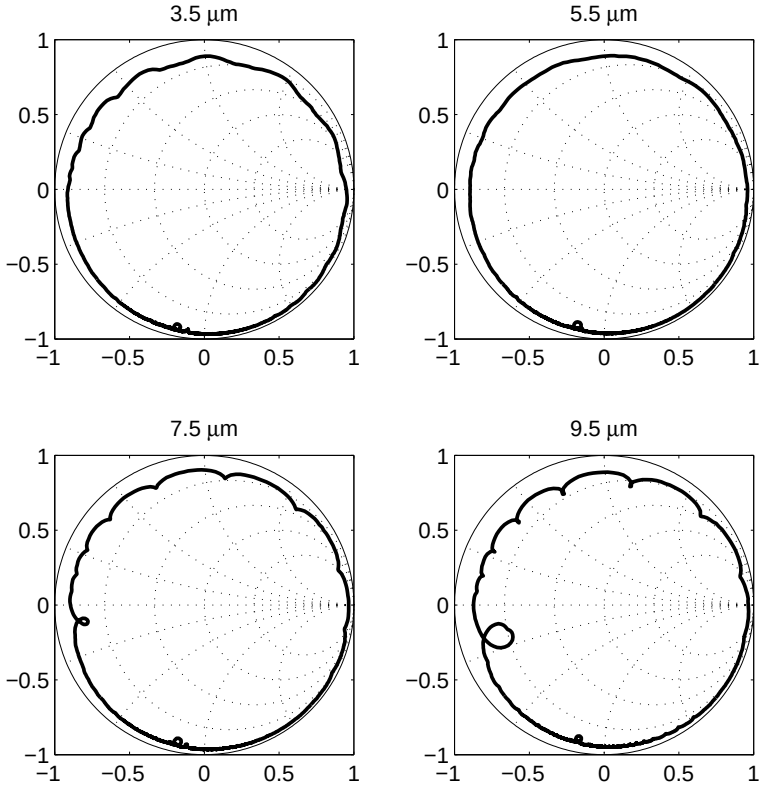

Figure 40: Measured scattering parameter S_{11} on the Smith chart for ZnO resonators with varied boundary frame width. The frame width is indicated on top of each chart. The resonator with 5.5 μm frame shows almost perfectly smooth response except for at near the bottom of the chart.

In Fig. 42, the harmonic vibration response of a resonator simulated with the 2-D model is presented as a function of frequency for a resonator with no boundary frame (top) and for a resonator with an optimal boundary frame (bottom). The flat amplitude at resonance ($f_\mathrm{s} = 930$ MHz) and clearly smaller contribution of spurious modes above f_s is evident in the latter.

The discussion has concentrated on resonators exhibiting so called Type I dispersion only. Type I dispersion refers to ZnO-type behavior where the TE_1 dispersion curve has a positive slope, i.e., the lateral wavenumber increases with frequency. Most materials, especially AlN, show intrinsically just the opposite behavior – the TE_1 dispersion curve has a negative slope when starting from the $\beta_x = 0$ axis for a certain region, before turning upwards. In this case the bound-

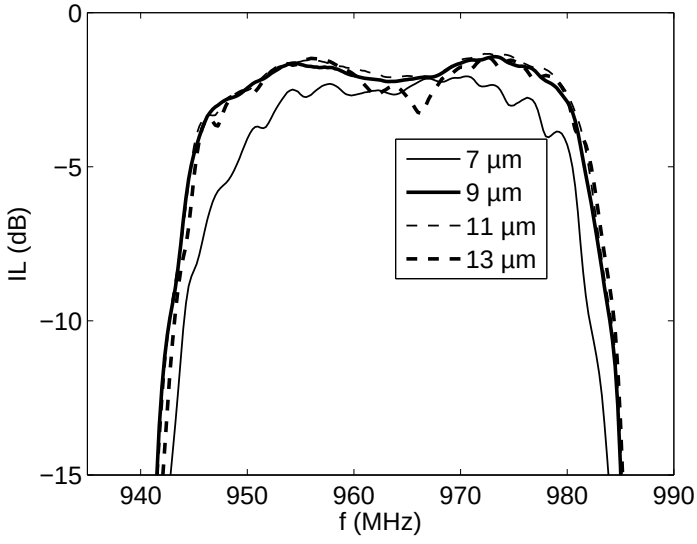

Figure 41: Three-stage ladder filters comprising of resonators with different frame widths. Both 9 and 11 μm-cases show very smooth passband, whereas on the 7 and 13 μm curves significant ripple is observed.

ary frame structure must be inverted, i.e., a recessed trench must be created in the place of the frame (Fig. 43). To avoid practical difficulties associated with this, a method of dispersion flipping in the SMR devices was developed by Infineon Technologies GmbH for making AlN-resonators to behave like ZnO-resonators and to apply the boundary frame [55]. The boundary frame method is nowadays being used in some form by most of the major industrial manufactures of BAW resonators.

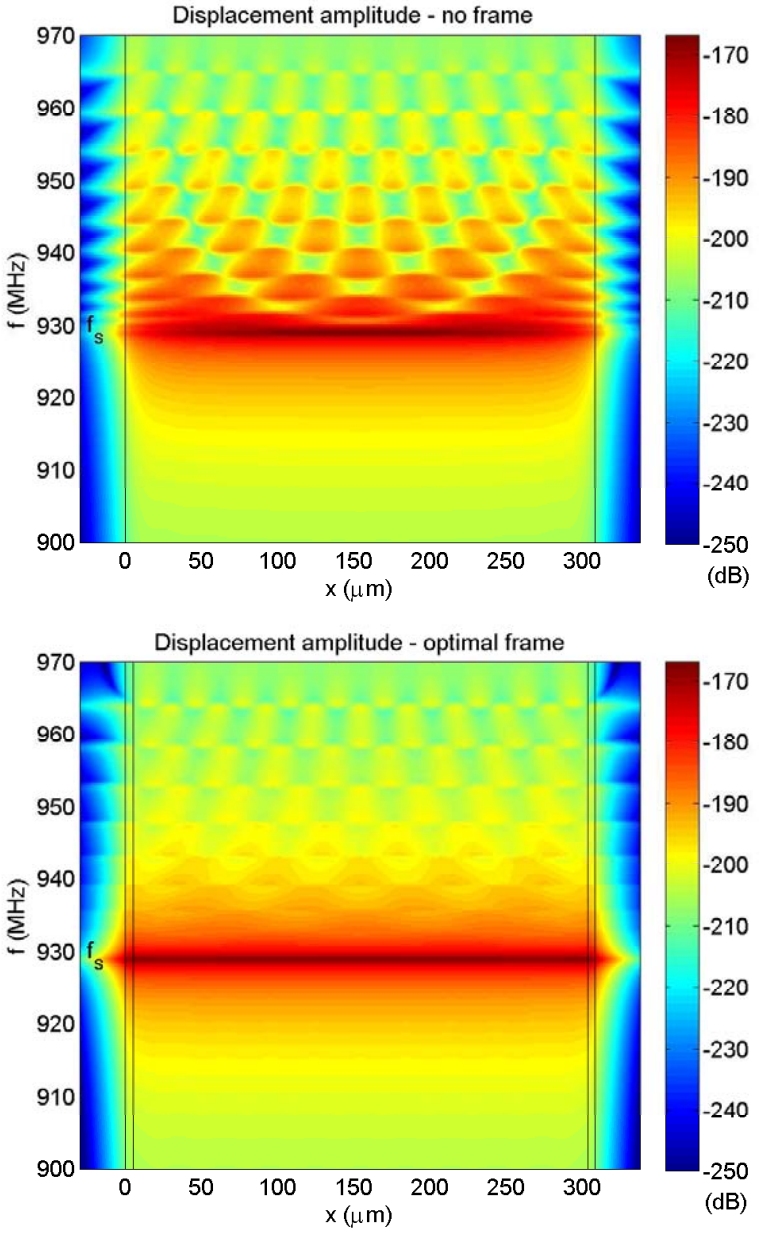

Figure 42: Logaritmic plot of the vertical displacement vs. frequency simulated by the 2-D model for a resonator without a boundary frame (top) and a resonator with a piston-mode producing boundary frame (bottom). Each horizontal line of the plot represents the vertical displacement amplitude vs. lateral position along the surface of the resonator. Thin vertical lines show the electrode edges (top) and the boundary frame (bottom).

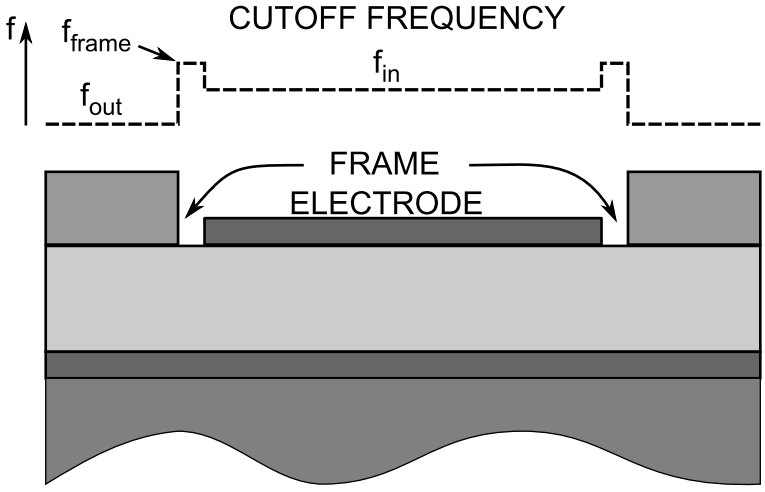

Figure 43: Cross section of an exemplary realization of the boundary frame method for a Type II resonator. The dashed line on top of the resonator shows the cutoff frequency at each region of the resonator.

5.6 Laterally Acoustically Coupled Resonator Filters

In Fig. 44 the fundamental and the only trapped resonance mode of a rather small resonator is shown. The vibration is energy-trapped by the electrode-induced cut-off frequency difference and the evanescent tail extending to the surrounding region is clearly visible. Consider bringing two such resonators in such a close proximity to each other, that their evanescent tails extend to the other resonators region with significant amplitude. The two resonators will form a coupled-resonator system supporting a symmetric and an antisymmetric mode (Fig. 45). The device acts as a pass-band filter with acoustical signal coupling, the width of the pass-band being defined by the frequencies of the two modes. It is exactly this kind of devices that motivated the development of the multiport 2-D model development discussed in Section 5.3 and in Papers 5 and 6.

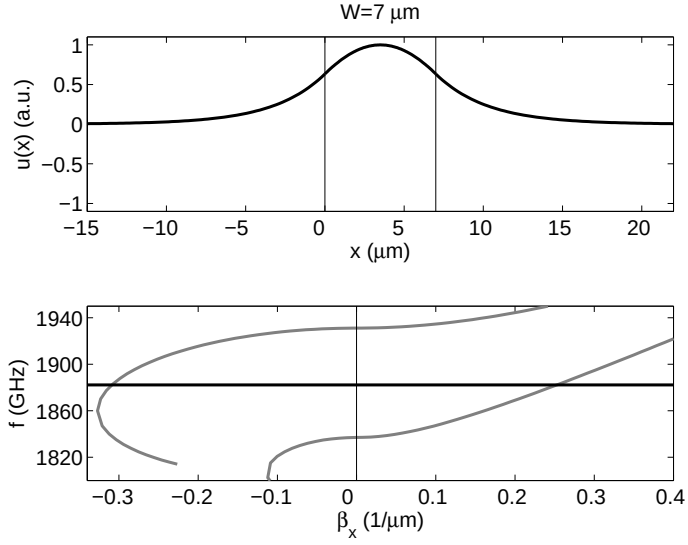

Figure 44: Simulated displacement (top) and frequency of the sole eigenmode and dispersion characteristics (bottom) of an isolated narrow resonator. In the displacement plot the vertical lines indicate the limits of the electroded area. In the dispersion plot the resonance frequency is indicated by a horizontal black line. The upper gray curve is the dispersion curve of the non-electroded outside region and the lower curve is for the electroded central region.

The acoustical coupling of adjacent resonators, referred to as the monolithic crystal filters (MCF, Fig. 46 A) has been utilized in quartz-crystal based technology already since 1960's to form narrow-band filters up to frequencies of some tens of MHz with galvanically isolated input and output [56, 8]. Another possibil-

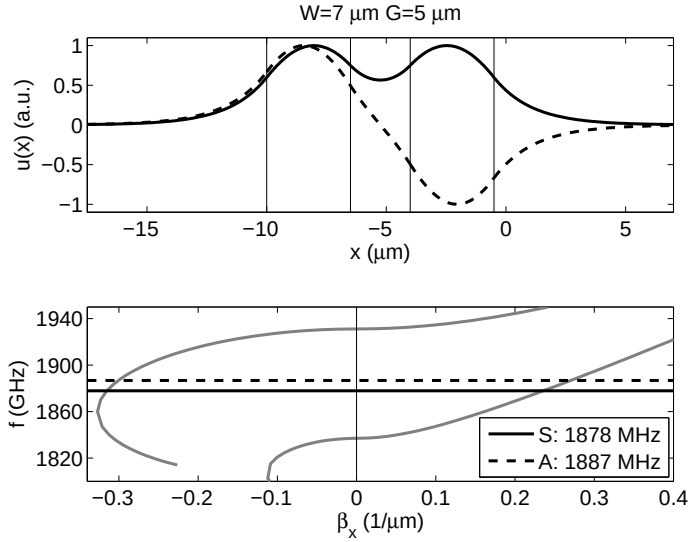

Figure 45: Simulated displacement (top) and frequency of the two eigenmodes and dispersion characteristics (bottom) of system of two narrow electrode regions in close proximity so that the resonators are coupled acoustically via the evanescent wave in the gap between them. In the displacement plot the vertical lines indicate the limits of the electroded areas. In the dispersion plot the resonance frequencies are indicated by horizontal black lines. The upper gray curve is the dispersion curve of the non-electroded outside and gap region and the lower curve is for the electroded resonator regions.

ity to realize an acoustically coupled filter is to stack two resonators on top of each other to form a stacked crystal filter (SCF, Fig. 46 B), and a further development of this, the coupled resonator filter (CRF, Fig. 46 C) having a layer or layers in between the two resonators to control the amount of inter-coupling for the resonators and providing means for galvanic isolation. The SCF and the CRF have been realized utilizing AlN thin film based BAW technology by several groups [57, 58, 59, 60, 61] motivated by the wide bandwidth, very small footprint, and possibility for balanced-unbalanced conversion. The fabrication of the vertically stacked thin film BAW resonators is, however, difficult to do economically due to process complexity and extreme tolerance requirements of fabrication.

The laterally coupled thin film BAW resonator filters [62, 63, 64, 65] (Fig. 46 D), a direct analogy of the MCF, are an attempt to obtain the benefits of the SCF and CRF with a simplified manufacturing technology and less stringent fabrication tolerances.

In its simplest form, the LBAW filter is formed by just two electrode areas

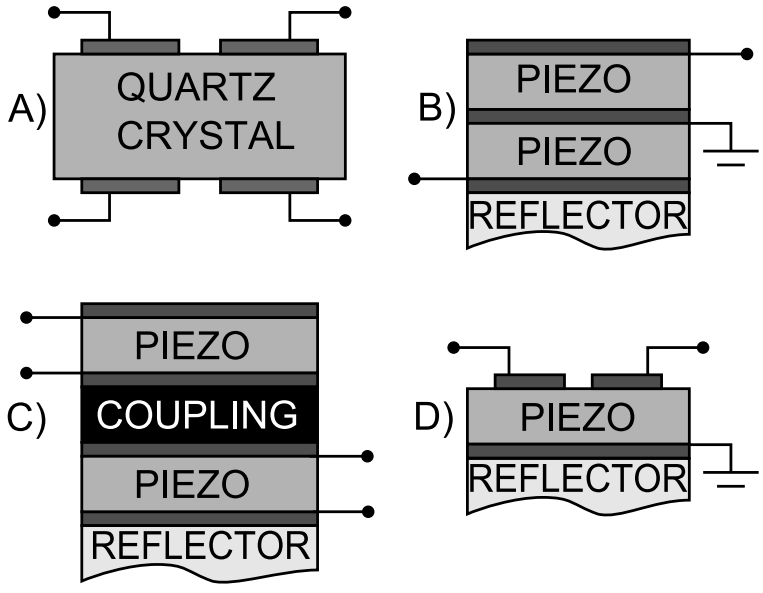

Figure 46: Illustrations of some acoustically coupled resonator filters: A) the monolithic crystal filter (MCF) B) the stacked crystal filter (SCF) C) the coupled resonator filter (CRF) and D) the laterally acoustically coupled filter (LBAW).

with a narrow gap between them. A study of this kind of a filter prototype was conducted in Paper 5. The bandwidth of the filter can be affected by the geometry (widths of the electrodes and the gap between them). To maximize the bandwidth, one must try to make the symmetric mode to have as low frequency as possible and the antisymmetric mode as high frequency as possible (we limit the discussion to Type I dispersion here). This is achieved by making the electrodes and the gap as narrow as possible while still supporting the two modes. The hard-wall limit for the frequency difference is the width of the energy trapping range. Insertion losses of two-electrode filters with varied geometry are presented in Fig. 47.

By a very simple two-resonator design fabricated by a single lithography process, pass band filters can be demonstrated, but with a modest pass band width (up to 1.45 %) and parasitic effects such a spurious pass band below the intended one (Papers 5 and 6). A photograph of such experimental device is shown in Fig. 48. In order to create filters with pass bands wide enough to be useful for e.g. the modern mobile communications devices, one can multiply the number of electrodes creating an interdigital type of structure similar to that in SAW devices. The effect of this is to press down the frequency of the symmetric mode as it is dependant on the total width of the device. The frequency of the antisymmetric mode is meanwhile increased as compared to that of the two-electrode basic ele-

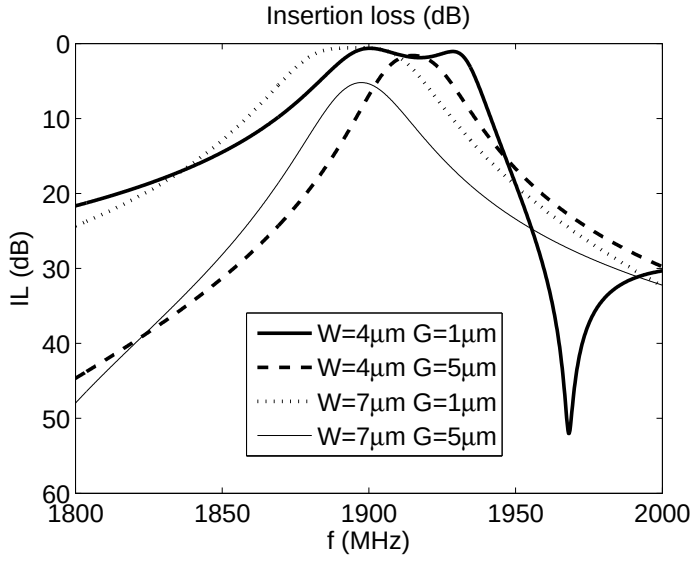

Figure 47: Insertion losses calculated for a two-electrode LBAW filter with various widths of the electrodes and gap. The combination of narrow fingers ($W = 4\mu\mathrm{m}$) and narrow gap ($G = 1\mu\mathrm{m}$) yield the widest bandwidth.

ment as the wavelength is determined to a higher extent by the periodicity of the electrode structure and less by the evanescent fields outside the filter. In between the two main modes, intermediate modes are also supported. A photograph of a 31 finger device is presented in Fig. 49 and the insertion loss of the device in Fig. 50. Post-measurement matching by with 120 Ω system impedance and 5 nH parallel inductances at both ports has been applied.

The device designed by J. Meltaus at VTT with the simulation tool developed in Paper 5 is remarkable for the following reasons:

- It shows a pass band with a relative width of 4.9 % which is competitive with commercial SAW and BAW microacoustic filters.
- It has steep passband edges as required by the mobile communications applications.
- It utilizes standard SMR BAW fabrication technology for the layer stack and just a single lithography with dimensions much more relaxed than in SAW at similar frequency range.
- Its footprint is merely that of a single BAW resonator used in ladder filters.

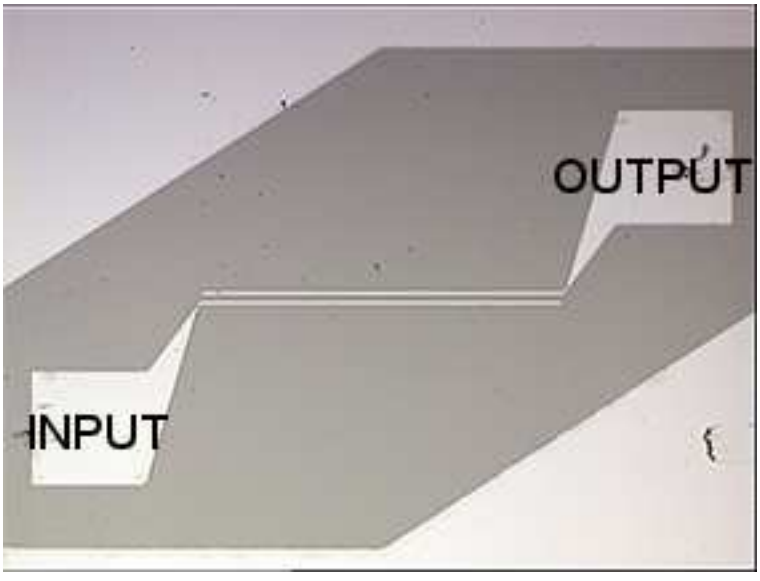

Figure 48: Photograph of a two finger LBAW filter.

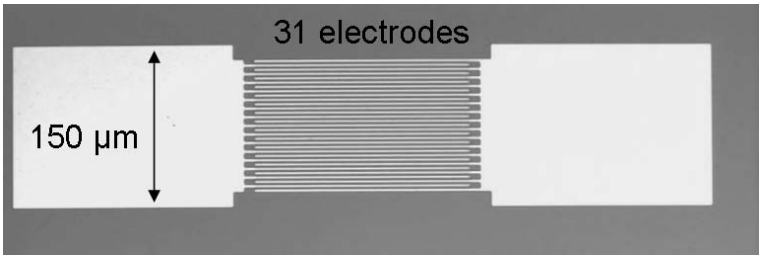

Figure 49: Photograph of a 31 finger LBAW filter.

Challenges remaining for the LBAW technology include removing the ripple in the passband, suppressing the parasitic passband, improving the stopband attenuation and designing the filters so that they can be matched to 50 Ω. These improvements will most likely require more mask layers to be added in the process, but on the other hand it seems feasible that the LBAW technology could allow for balun functionality and bandwidths even wider than 5 %. These demonstrated, the LBAW has potential to become a disruptive technology for RF filtering.

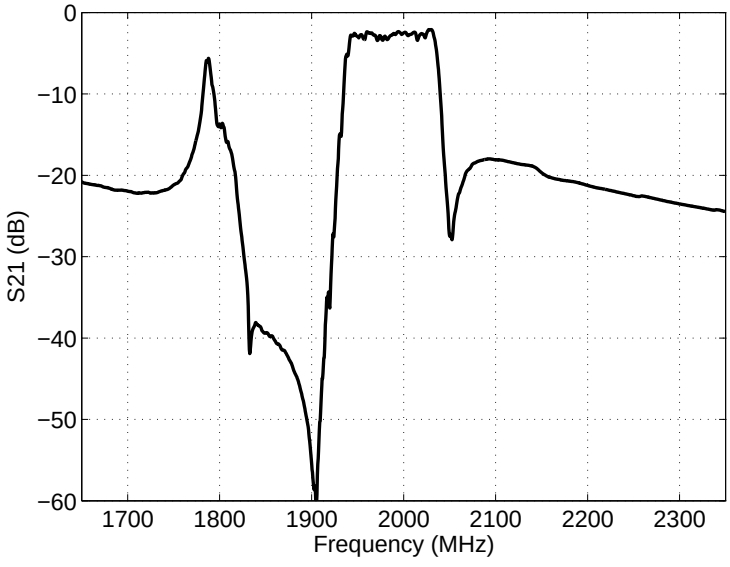

Figure 50: Transmission S_{21} of a 31 finger LBAW filter based on AlN SMR technology and just a single lithography step. Post-measurement matching with 120 Ω system impedance and 5 nH parallel inductances at both ports has been applied.

6 Interferometric Imaging of BAW Resonators

Scanning laser interferometry provides a method to image surface vibrations of microacoustic devices with high sensitivity and dynamic range [66, 67, 68, 69, 70]. The method is based on splitting a laser beam into two paths, of which the first one is reflected from the vibrating surface of the microacoustic device and the other one serves as the reference beam. The interference of the recombined beams is used to obtain information on the surface vibration. The sample is scanned relative to the fixed laser beam that is focused to a small spot roughly 1μm in size, yielding for a 2-D map of the vibration field. The technique has been intensively developed at the Helsinki University of Technology since the 1990's. Two different setups have been employed in the papers of this work: a Michelson-type interferometer [71] capable of measuring the amplitude of vibration and a later development, a heterodyne interferometer [72] yielding for both absolute amplitude and phase data of the out-of plane vibration. As small as 1 pm amplitudes can be detected, the applicable frequency ranging up to 6 GHz. The heterodyne setup is presented in Fig. 51.

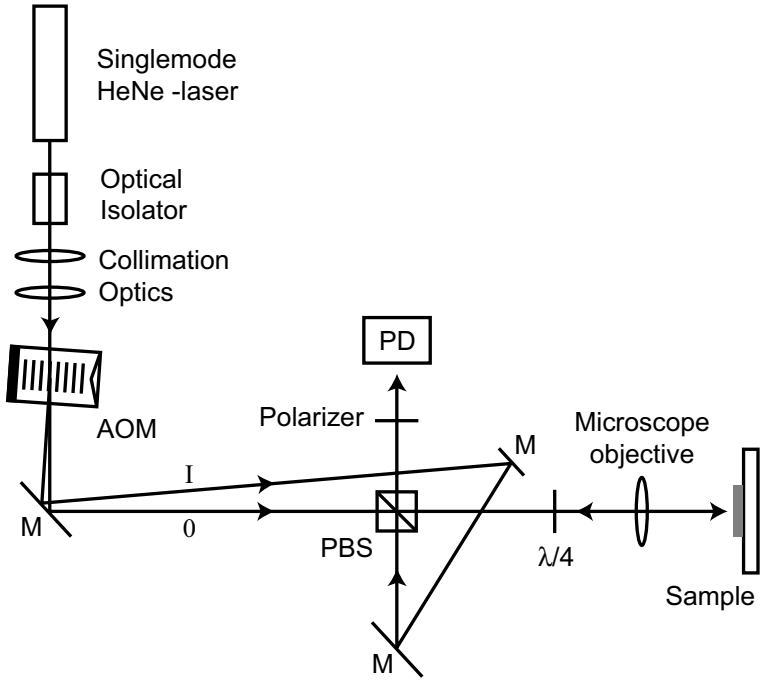

Figure 51: Schematic of the scanning heterodyne interferometer used for imaging acoustic vibrations of GHz frequency devices. The sample is scanned in front of the measurement beam in order to form a spatial map of the vibration fields [72].

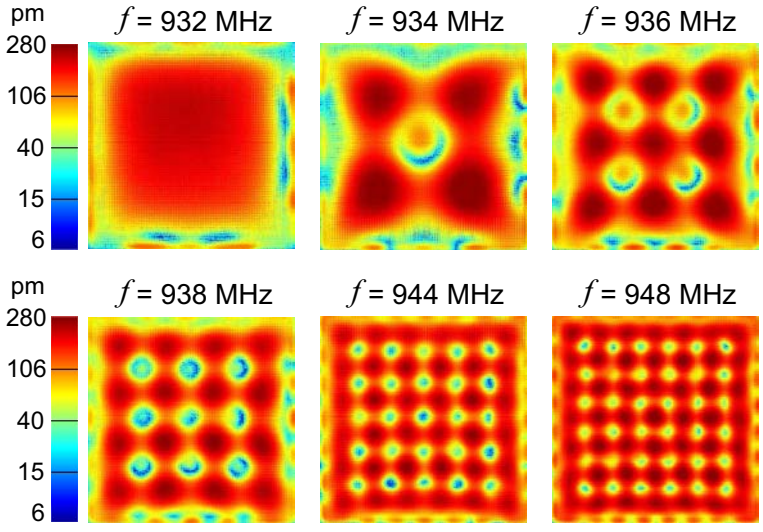

Figure 52: Interferometrically measured out-of-plane vibration amplitudes of a 932 MHz ZnO SMR at the series resonance frequency and at selected frequencies above it. The laterally standing wave resonances are pronounced at the higher frequency scans. Image courtesy of Kimmo Kokkonen, Aalto University.

The interferometer can be used to image direct spatial wave fields in order to study the vibration modes of the BAW resonators. It can be used to verify that the devices are operating as designed and modeled such as in Paper 5, and to analyze spurious modes. In Fig. 52, measured vibration fields of a 932 MHz ZnO BAW resonator at the series resonance frequency and at some selected frequencies above it, coinciding with spurious oscillations, are presented.

By measuring the vibration fields on the surface of the device as a function of frequency, one can extract the lateral dispersion characteristics by using Fourier techniques [73]. This includes first windowing the measured 2-D displacement field $u(x, y; f)$, applying 2-D discrete Fourier transformation to yield a spatial spectrum $U(\beta_x, \beta_y; f)$, where β_x and β_y are the components of the lateral wavenumber, and then reducing the data to a single wavenumber dimension $U(\beta_{||}, f)$ for example by averaging along circles of radius $\beta_{||} = \sqrt{\beta_x^2 + \beta_y^2}$. An example of a high resolution dispersion diagram measured by laser interferometry is shown in Fig. 53.

In [74] the correspondence of the ripple in the electrical response and interferometrically observed mechanical response, integrated over $\beta_{||}$ to yield a power spectrum was presented, proving experimentally the connection of the laterally standing wave modes and the spurious ripple in the electrical response (Fig. 54).

In Paper 1, the measured dispersion curves were used to find information on

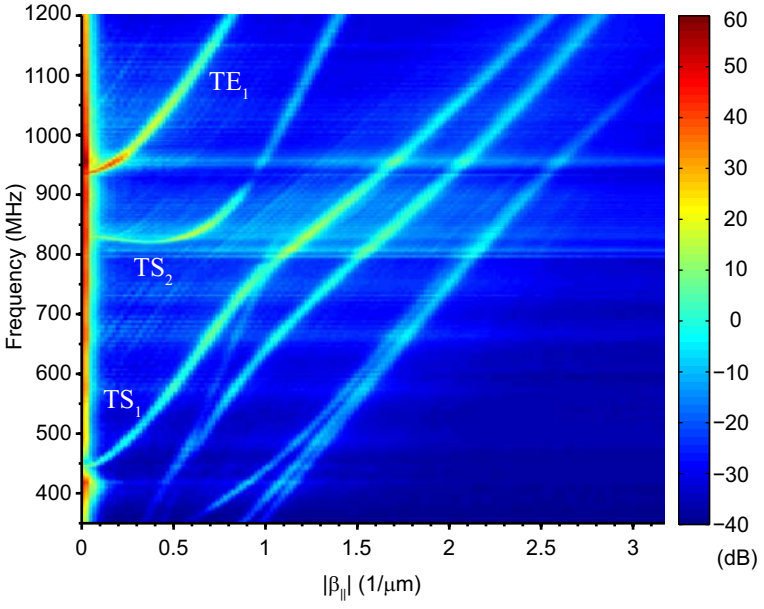

Figure 53: Dispersion diagram measured by a laser interferometer from a ZnO SMR device. Image courtesy of Kimmo Kokkonen, Aalto University.

the material parameters of the thin films used in the device by fitting a dispersion model to the measurement. This allows in principle the extraction of full material parameters for both longitudinal and shear wave modes, provided that the film thicknesses are known accurately. While the initial attempt was in the quantitative sense not so successful, most likely due to inaccuracy in the layer thicknesses, the method was later quite successfully adopted by A. Link *et al.* in [75].

In optimizing the performance of BAW resonators and devices, the accurate knowledge and control of dispersion characteristics is a key issue. While the dispersion can in principle be modeled rather easily, it requires accurate knowledge of material parameters and layer thicknesses. Interferometric measurement provides a way to directly measure whether the design and modeling has succeeded and give feedback to the selection of the model parameters. Dispersion measurement can also be used as diagnosis tool for ill-working resonators.

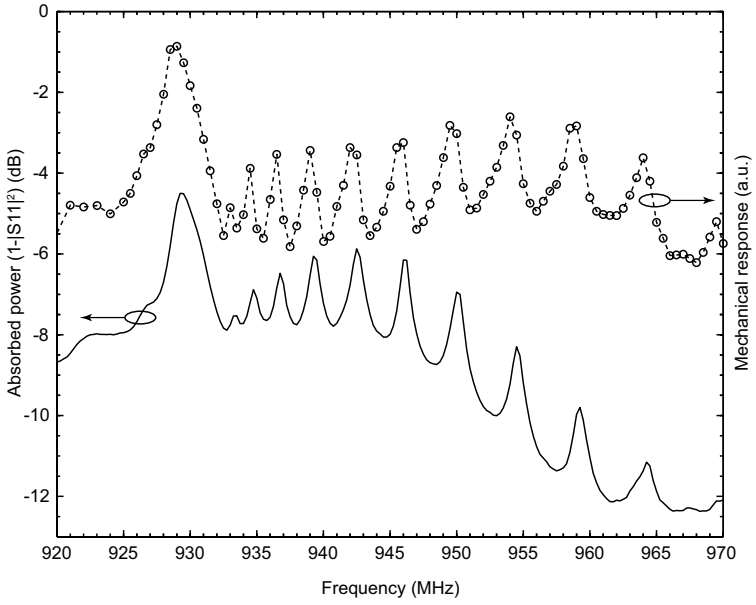

Figure 54: Comparison of absorbed electrical power $1 - |S_{11}|^2$ (solid line) and mechanical response integrated over spatial wave number (dashed line) both showing the spurious oscillations with high level of correlation [74].

7 Loss Mechanisms in a BAW Resonator

The loss mechanisms in the thin film BAW resonators include leakage to the substrate, laterally escaping waves, ohmic losses, viscous losses, dielectric losses, and wave scattering. Also mentioned in the literature are eddy current losses [6] and losses due to formation of conducting channels in the high resistivity Si substrate – SiO_2 interface [76].

Acoustic leakage to the substrate is characteristic to the SMR type devices and is almost non-existent in FBARs suspended on air. This is due to the acoustic reflector having only finite reflectivity as compared to the practically perfect substrate isolation of FBAR type devices.

Laterally escaping waves are observed in the interferometric measurements and FEM simulations [6, 75]. They arise from excitation of higher β_x plate wave modes that are not trapped within the resonator. The reason for their excitation is most likely the discontinuity at the resonator edge.

The ohmic losses include the resistance of the electrodes but also ohmic dissipation of locally induced charge concentrations associated with the vibration patterns of the spurious modes. Utilizing low resistivity materials such as Au or Al in the electrodes with high enough thickness reduces ohmic losses, but resistivity must be co-optimized with other properties such as the coupling coefficient and this easily leads to trade-offs [77, 32].

Viscous losses are intrinsic to the materials used in the devices. Apart from the choices of materials, not much can be done about them. Among the acoustic materials typically used in BAW devices, SiO_2 and Al have largest losses, while AlN, Mo, and W are all rather low-loss materials. Viscous dissipation is proportional to the space derivative of strain, so one may try to design the acoustic structure in order to avoid high strain rates of change within the lossy material layers.

7.1 Experimental Determination of the Reflector Performance

In Papers 2 and 3, the reflector leakage was studied in detail. Marksteiner *et al.* found out in [36] that a significant improvement in Q-values of SMR devices can be obtained by providing shear reflectivity simultaneously with the primary longitudinal reflectivity – something not achieved by a standard quarter-wavelength reflector. Resonators with such a shear optimized reflector fabricated by Infineon Technologies GmbH showing a Q-value approaching 2000 at 1850 MHz were post-processed so that the substrate was removed under the reflector. For the removal of the substrate, the Si substrate was first thinned and polished to facilitate performing lithography on the backside of the wafers. Then the substrate was removed under some, but not all of the resonators. Resonators where electrically characterized both before and after the substrate release leading to having

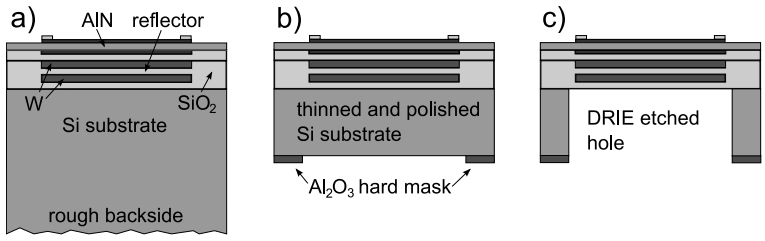

Figure 55: Experiment performed in Paper 2. a) shows the unprocessed resonators which have roughened backside of the wafer, b) shows the resonators that have polished and thinned Si substrate under the reflector, and c) shows the resonators that have no substrate under the reflector at all.

measurement of three different kind of resonators to compare (Fig. 55): a) untouched resonators with thick and roughened substrate underneath, b) resonators on thinned and polished Si substrate, and c) suspended resonators with no substrate at all.

It was found out that in the resonators with substrate remaining underneath the reflector but having been polished on the backside, a set of new spurious resonances with regular frequency spacing arose in the electrical response (Fig. 56 'after'). This frequency spacing matches that of standing wave resonances in the substrate. In the resonators where the substrate was removed, these backside reflections disappear.

In the Q-values of the resonators, no significant change could be confirmed as a result of the rework (see Table 4). It was thus concluded that while acoustic energy clearly leaks to the substrate through the reflector as shown by the existence of the backside reflections, it is not the limiting factor to Q-value at these devices. Some other mechanisms of loss are to be dealt with before further optimization of the reflector can yield improvement in the Q-value. A likely candidate for a Q-limiting mechanism are the laterally leaking waves, although others must be considered too [22, 6].

The approach of Marksteiner *et al.* in [36] to model the effect of having the acoustic reflector to provide both longitudinal and shear reflectivity is based on separately calculating longitudinal and shear transmittances of the reflector in 1-D, and then assuming a constant fraction of the energy to be in the shear waves. Thus they calculate a composite Q-value combining losses due to longitudinal and shear wave leakages, that is to be maximized with minimal trade off with effective coupling coefficient. While clearly very successful in practice, this picture is a very rough oversimplification of the actual situation. To study the matter in more depth, an analysis of the reflector transmission characteristics by laser

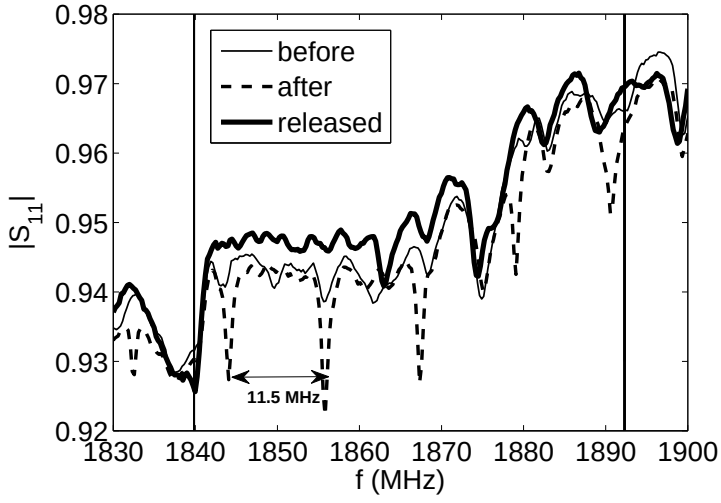

Figure 56: Magnitude of S_{11} measured from resonators before any rework ('before'), with substrate thinned and polished ('after'), and substrate removed ('released'). The vertical lines indicate average f_{s} and f_{p} values. The 11.5 MHz spacing of the dips in the 'after' -data correspond to backside reflections in the substrate. This individual resonator shows increased $|S_{11}|$ after releasing but the effect is not systematically present in all devices.

Table 4: Q-value data over all measured devices. B = before processing, A = after processing, R = released resonators. Three methods of extracting the Q-values were compared: Q_{p} is a direct evaluation of Eq. (12), $Q_{\mathrm{mech.}}$ is Eq. (13) resulting from fit procedure described in Section 2.3, and $Q_{\mathrm{Bode,MAX}}$ is calculated according to method of Feld *et al.* [78]. For more details, see Paper 2.

	Condition	Range	Spread
Q_{p}	B	950-1370	420
	A	800-1280	480
	R	1080-1340	260
$Q_{\mathrm{mech.}}$	B	1770-1910	140
	A	1800-2010	210
	R	2050-2200	150
$Q_{\mathrm{Bode,MAX}}$	B	1530-1840	310
	A	1500-1700	200
	R	1590-1970	280

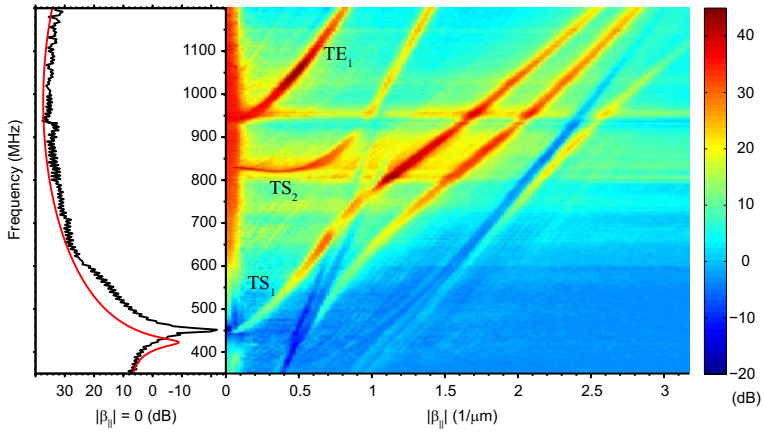

Figure 57: Measured reflector attenuation (73) (right) and 1-D simulation of reflector attenuation (red line) compared to that extracted from the measurement (black noisy line) along $\beta_{||} = 0$.

interferometric measurements of vibration amplitude both on the surface of the resonator and at the reflector-substrate interface was performed in Paper 3. This was allowed by a transparent glass substrate used in the samples. The measurement results were compared with predictions of the 1-D transfer matrix model and the 2-D FEM model. Utilizing Fourier techniques, the reflector transmittance characteristics were determined as functions of both frequency and lateral wave number over a wide range.

The measured reflector attenuation shown in Fig. 57 is defined by

$$M_{\mathrm{attn}}(\beta_{||}, f) = 20 \log_{10} \frac{D_{\mathrm{top}}(\beta_{||}, f)}{D_{\mathrm{bot}}(\beta_{||}, f)}, \tag{73}$$

where $D_{\mathrm{top}}(\beta_{||}, f)$ and $D_{\mathrm{bot}}(\beta_{||}, f)$ are the Fourier transformations of the out of plane vibration amplitude measured at the top and bottom of the device, respectively, and $\beta_{||}$ is the circularly averaged wavenumber component along the surface of the resonator. The line plots on the left of the attenuation, compare the 1-D simulated reflector attenuation (smooth line) defined by

$$M_{\mathrm{attn}}(f) = 20 \log_{10} \frac{u_{\mathrm{top}}(f)}{u_{\mathrm{bot}}(f)}, \tag{74}$$

where $u_{\mathrm{top}}(f)$ and $u_{\mathrm{bot}}(f)$ are the displacements extracted from the top and bottom of the 1-D layer stack as response to constant voltage drive, and the measured attenuation along the $\beta_{||} = 0$ axis (i.e. at the long lateral wavelength limit). These data constitute a direct measurement of the reflector performance. It was found out that in the $\beta_{||} = 0$ limit, the longitudinal 1-D model predicts the behavior of

the reflector very well. The simulated and measured attenuations agree within 2 dB in magnitude and the shapes of the frequency responses match closely.

Interesting features are observed in the $(\beta_{||}, f)$-domain, including a strong attenuation maximum on the TE_1 curve not coinciding with the operation point of the resonator and sudden notches in the attenuation on some dispersion curves. The 2-D FEM modeling was able to reproduce many of the features observed in $(\beta_{||}, f)$-domain measurements, but it is evident that for quantitatively accurate predictions one must employ absorbing boundary conditions which work for all wave modes simultaneously at the lateral and bottom edges of the model. That provided, 2-D FEM would form a powerful tool for Q-value optimization of the BAW devices.

8 Discussion

Based on high quality AlN piezoelectric thin film and careful design, industrial state-of-the-art SMR BAW resonators can reach Q-values of around 2600 in the 2 GHz frequency range and effective coupling coefficient K^2 of 6.30 % (using definition (20)) [79]. In this kind of devices, both lateral and vertical energy trapping must be co-optimized extremely well, the first being influenced by the dispersion characteristics and the boundary structures of the resonator and the latter by the longitudinal and shear wave transmission properties of the reflector. The reflector performance and the dispersion characteristics are both determined by the layer thicknesses and material properties of the complete layer stack, the control of and accurate knowledge of which are crucial. State-of-the-art resonators of the air-gap (FBAR) type not suffering from any kind of acoustic leakage to the substrate, show Q-values up to 3700 [79] at 2 GHz and effective coupling coefficient K^2 reaching 7 % (definition (20)). In the industrial devices, spurious resonance suppression is based on both boundary frame method and apodization. This work has concentrated on the investigation and optimization of part of the basic building blocks that enable realization of high performance BAW resonators.

The state-of-the-art BAW resonators allow for fabrication of high performance GHz range pass-band filters for the mobile phone radio systems. BAW filters complement the dominating SAW filter technology in the high frequency (>2 GHz) applications that are most demanding in the insertion loss, pass-band skirt steepness, and temperature stability requirements. Examples of such applications are the US-PCS duplexer and some WCDMA bands. The AlN BAW ladder filter is fairly limited in application range due to its pass band width being strictly limited by the electromechanical coupling coefficient of AlN and due to the lack of an economical way of providing balanced-unbalanced conversion, which SAW filters can readily offer. Thus BAW is much less versatile as compared to SAW as a general filter technology platform. In its present state, the BAW filter technology does not seem to be on a path to replace a significant portion of the SAW filter market, but is a necessary component in order to enable fabrication of modern mobile phones that operate almost anywhere in the world.

The availability of high-Q BAW resonators has raised interest in their usage in applications other than RF filters. For example, a BAW resonator can serve as a frequency reference in an oscillator, facilitated by the fact that it is rather straightforward to fabricate resonators that are temperature stable to the first order [20, 80, 81]. Thin film BAW resonators coated with a chemically active layer have also been used as chemical sensors due to the extreme sensitivity for surface mass loading [82, 83]. No significant commercial success, however, exists yet outside the field of mobile phone RF filters.

The present 3G and the upcoming 4G/LTE mobile phones will continue to

add to the complexity of the radio systems and number of frequency bands at use. The requirements for the filter performance in bandwidth, pass-band edge steepness, linearity, and temperature stability are high. A large number of filters and duplexers need to be fitted into a small footprint and produced in a highly economical way. A characteristic feature of both SAW and BAW technologies is their vibrating surface requiring a hermetic package which increases cost and size of the systems.

For expanding the application range of the thin film BAW technology, the laterally coupled BAW (LBAW) filter is a promising development. The obtainable filter bandwidth may be much larger than in the ladder filters and balanced-unbalanced functionality seems to be feasible with a reasonable amount of added complication in the fabrication process.

Another path of further development of the BAW technology would be the introduction of new low-loss thin film materials exhibiting piezoelectric effect significantly stronger than that of AlN. Availability of, for example, high quality industrial level $\mathrm{LiNbO_3}$ thin film deposition process, would open up a completely new range of possibilities for miroacoustics. Recently, Kadota *et al.* have reported microacoustic devices based on chemical vapor deposition of $\mathrm{LiNbO_3}$ thin films [84]. A very interesting finding reported in [85] is that ScAlN exhibits up to 400 % increased piezoelectric coefficients as compared to plain AlN.

An interesting development arising from the field of SAW filters is the piezoelectric boundary wave devices [86]. Filters with attractive performance have been realized by employing a wave mode concentrated at the interface of a piezoelectric crystal and another material, where an interdigitated electrode similar to that used in SAW filters is employed [87]. Perhaps the most remarkable feature of these devices is that the vibration does not reach the outer surfaces of the device and thus they do not require a hermetic package like traditional SAW and BAW components.

In the complicated multi-band mobile phones, it would be highly desirable to have a software controlled filter, which can adjust to the band or bands (or even channels within the bands) at use at a given moment. Technology allowing for that does not exist at the moment – at least with a form factor that could be imagined to fit into a mobile phone. The frequency of microacoustic filters cannot be effectively tuned, as it would require the change of dimensions or material properties of solid materials. The latter is possible to some extent in ferroelectric materials and very strong piezoelectrics, which unfortunately often exhibit large losses. In principle, a filter could be based on tunable capacitors and inductors, but at GHz-frequencies their Q-values are low and size fairly large. Digital filtering would require very high computation power at the GHz range and result in high power consumption. At the present, it cannot be foreseen if a tunable filter technology will emerge, and what the technology would be based on, but there certainly will

be efforts to realize one in the coming years. Meanwhile, microacoustic filters consisting of SAW, BAW, boundary wave, and possibly laterally coupled BAW devices will be the dominant technology for mobile phone RF filters.

9 Summary

The performance of a thin film BAW resonator depends most critically on the quality of the piezoelectric thin film it is based on. Provided a high quality piezomaterial is available, the next design issues of utmost importance are the optimization of the energy trapping efficiency in both vertical and lateral directions and the control of the laterally standing wave resonances. The former is instrumental for achieving high Q-value resonators and the latter for avoiding spurious ripple in the resonator and filter responses.

The design, modeling and performance optimization of thin film BAW resonators of the SMR type based on acoustic Bragg reflectors were addressed in this work. The modeling tools used were the 1-D electro-acoustic transfer matrix model for the resonator, a transmission line model for the reflector stack, the Thomson-Haskell matrix method for plate wave dispersion characteristics, and 2-D FEM. A dispersion based model for lateral eigenmodes and acoustical intercoupling of adjacent resonators allowing for acoustically coupled filter design were developed. For the characterization of resonators, electrical measurements and interferometric measurements of vibration fields at the devices, combined with Fourier techniques to yield dispersion characteristics, were used.

For all modeling, accurate knowledge of the material parameters is crucial. In order to predict the effects that depend on the dispersion characteristics, it is necessary to know not only the longitudinal wave parameters but also the shear wave parameters, which are difficult to measure. In Paper 1, extraction of the full set of elastic parameters from a thin film material by fitting a dispersion model to interferometrically measured dispersion curves was demonstrated.

The design of Bragg reflectors of the SMR type devices based on different materials were discussed in Section 3.2. The industrially successful $\mathrm{W} - \mathrm{SiO_2}$ reflector, requiring two lithography steps, provides good performance based on its superior impedance ratio over all-dielectric reflectors and metal-dielectric reflectors using metals lighter than W. It was shown, however, that with a hybrid reflector consisting of several layer pairs of $\mathrm{Ta_2O_5}$ and $\mathrm{SiO_2}$ and only a single layer of Pt requiring a single lithography, high performance SMRs can be realized.

In Paper 2, an experiment was conducted to find out whether the Q-value of a 2 GHz SMR having a shear-optimized reflector can still be improved from around 2000, but it was found out that the leakage through reflector, although clearly present, was not the Q-limiting factor in those devices – other loss mechanisms have to be sought for further improvement. To study the reflector performance in more detail, a laser interferometric measurement of vibration fields on top and at the bottom of an SMR on a transparent substrate was conducted in Paper 3. The 1-D model was found to agree with the experimental reflector performance at

the long lateral wavelength limit very well, but features depending on the lateral wavelength were discovered. From comparison of measurement and 2-D FEM modeling results, it was concluded that with improvements in handling of acoustic leakage at the boundaries, the 2-D FEM could be used as a powerful tool for advanced reflector optimization.

The most important lateral plate wave dispersion-related effects in BAW resonators are the lateral energy trapping and laterally standing plate wave resonances, the spurious resonances. The suppression of the lateral resonances by the boundary frame method was studied in detail by dispersion based 2-D and 2-D FEM modeling and a comparison to actual devices in Paper 4, where it was found out that two suppression effects are present in such structures – a narrow band single-mode suppression and a wide band suppression, the latter being related to the approximate orthogonality of the eigenmodes.

The dispersion based modeling of laterally standing waves was further developed to facilitate simulation of harmonic response of devices consisting of an arbitrary number of acoustically coupled adjacent resonators forming an electrical N-port (Paper 5). This allowed for design of experimental laterally coupled BAW filters (Paper 6, Figs. 49–50), which shows promise as a new type of microacoustic filter combining desired features of both SAW and BAW technologies.

References

[1] 3rd Generation Partnership Project (3GPP), "Technical Specification 05.05 V8.20.0 (2005-11)," 2005.

[2] Nokia Oyj, http://www.nokia.fi/tuotteet/kaikki-puhelimet/nokia-n8/tarkka-tuoteseloste, August 2010.

[3] R. Aigner, "SAW and BAW technologies for RF filter applications: A review of the relative strengths and weaknesses," in *Proc. IEEE Ultrasonics Symposium*, 2008, pp. 582–589.

[4] I. Larson, J.D., R. Ruby, P. Bradley, and Y. Oshmyansky, "A BAW Antenna Duplexer for the 1900 MHz PCS Band," in *Proc. IEEE Ultrasonics Symposium*, 1999, pp. 887–890.

[5] M. Kadota, T. Nakao, N. Taniguchi, E. Takata, M. Mimura, K. Nishiyama, T. Hada, and T. Komura, "Surface Acoustic Wave Duplexer for US Personal Communication Services with Good Temperature Characteristics," *Japanese Journal of Applied Physics*, vol. 44, no. 6B, pp. 4527–4531, 2005.

[6] K.-Y. Hashimoto, Ed., *RF Bulk Acoustic Wave Filters for Communications*. Artech House, 2009.

[7] C. Lam, "A review of the recent development of MEMS and crystal oscillators and their impacts on the frequency control products industry," in *Proc. IEEE Ultrasonics Symposium*, 2008, pp. 694–704.

[8] R. Kinsman, "A history of crystal filters," in *Proc. IEEE Frequency Control Symposium*, 1998, pp. 563–570.

[9] K. Lakin, J. Wang, G. Kline, A. Landin, Y. Chen, and J. Hunt, "Thin Film Resonators and Filters," in *Proc. IEEE Ultrasonics Symposium*, 1982, pp. 466–475.

[10] R. Ruby, "Micromachined cellular filters," in *IEEE MTT-S Microwave Symposium Digest*, 1996, pp. 1149–1152.

[11] W. E. Newell, "Face-mounted piezoelectric resonators," in *Proceedings of the IEEE*, vol. 53, no. 6, 1965, pp. 575–581.

[12] P. Bradley, R. Ruby, A. Barfknecht, F. Geefay, C. Han, G. Gan, Y. Oshmyansky, and I. Larson, J.D., "A 5 mm $\times$ 5 mm $\times$ 1.37 mm hermetic FBAR duplexer for PCS handsets with wafer-scale packaging," in *Proc. IEEE Ultrasonics Symposium*, 2002, pp. 931–934.

[13] G. Fattinger, A. Volatier, R. Aigner, and F. Dumont, "BAW PCS-Duplexer Chipset and Duplexer Applications," in *Proc. IEEE Ultrasonics Symposium*, 2008, pp. 602–606.

[14] E. Schmidhammer, H. Heinze, M. Schmiedgen, M. Mayer, and A. Link, "High Volume Production of a Fully Matched 5050 PCS-CDMA-BAW Duplexer," in *Proc. IEEE Ultrasonics Symposium*, 2006, pp. 329–332.

[15] K. M. Lakin and J. S. Wang, "Acoustic bulk wave composite resonators," *Applied Physics Letters*, vol. 38, no. 3, pp. 125–127, 1981.

[16] G. Perluzzo, C. Jen, and E. Adler, "Characteristics of reactive magnetron sputtered ZnO films," in *Proc. IEEE Ultrasonics Symposium*, 1989, pp. 373–376.

[17] C. Vale, J. Rosenbaum, S. Horwitz, S. Krishnaswamy, and R. Moore, "FBAR filters at GHz frequencies," 1990, pp. 332–336.

[18] P. Osbond, C. Beck, C. Brierley, M. Cox, S. Marsh, and N. Shorrocks, "The influence of ZnO and electrode thickness on the performance of thin film bulk acoustic wave resonators," in *Proc. IEEE Ultrasonics Symposium*, 1999, pp. 911–914.

[19] J. Molarius, J. Kaitila, T. Pensala, and M. Ylilammi, "Piezoelectric ZnO films by r.f. sputtering," *Journal of Materials Science: Materials in Electronics*, vol. 14, no. 5, pp. 431–435, 2003.

[20] K. Lakin, K. McCarron, and J. McDonald, "Temperature compensated bulk acoustic thin film resonators," in *Proc. IEEE Ultrasonics Symposium*, 2000, pp. 855–858.

[21] B. Auld, *Acoustic Fields and Waves in Solids*, 2nd ed. Robert E. Krieger Publishing Company, 1990, vol. I.

[22] R. Ruby, "Review and Comparison of Bulk Acoustic Wave FBAR, SMR Technology," in *Proc. IEEE Ultrasonics Symposium*, 2007, pp. 1029–1040.

[23] J. Kaitila, M. Ylilammi, J. Ella, and R. Aigner, "Spurious resonance free bulk acoustic wave resonators," in *Proc. IEEE Ultrasonics Symposium*, 2003, pp. 84–87.

[24] J. Rosenbaum, *Bulk Acoustic Wave Theory and Devices*. Artech House, 1988.

[25] J. Larson, P. Bradley, S. Wartenberg, and R. Ruby, "Modified Butterworth-Van Dyke circuit for FBAR resonators and automated measurement system," in *Proc. IEEE Ultrasonics Symposium*, 2000, pp. 863–868.

[26] *IEEE Standard on Piezoelectricity, Std 176-1987*. ANSI/IEEE, 1987, p. 51.

[27] K. Yoo, H. Uberall, and J. Williams, W., "Spurious Resonances in Bulk Acoustic Wave Resonators," in *Proc. IEEE Ultrasonics Symposium*, 1982, pp. 490–493.

[28] B. Auld, *Acoustic Fields and Waves in Solids*, 2nd ed. Robert E. Krieger Publishing Company, 1990, vol. II.

[29] R. Aigner, "Bringing BAW technology into volume production: The ten commandments and the seven deadly sins," in *Proc. 3rd International Symposium on Acoustic Wave Devices for Future Mobile Communication Systems*, 2007.

[30] T. Pensala, M. Ylilammi, J. Meltaus, and K. Kokkonen, "Area and Dispersion Dependence of Vibration Shape and Coupling Coefficient in Thin Film BAW Resonators," in *Proc. IEEE Ultrasonics Symposium*, 2007, pp. 1661–1664.

[31] S. Chang, N. Rogacheva, and C. Chou, "Analysis of methods for determining electromechanical coupling coefficients of piezoelectric elements," *IEEE Trans. on Ultrasonics, Ferroelectrics, and Frequency Control*, vol. 42, no. 4, pp. 630–640, 1995.

[32] J. Kaitila, "Review of Wave Propagation in BAW Thin Film Devices – Progress and Prospects," in *Proc. IEEE Ultrasonics Symposium*, 2007, pp. 120–129.

[33] W. P. Mason, *Piezoelectric Crystals and Their Applications to Ultrasonics*. D. Van Nostrand, 1950.

[34] M. Ylilammi, "Handbook of Bulk Acoustic Wave Resonators and Filters," 2000, VTT Internal report.

[35] E. Voipio, *Siirtojohtojen teoria*. Otakustantamo, 1973.

[36] S. Marksteiner, J. Kaitila, G. Fattinger, and R. Aigner, "Optimization of Acoustic Mirrors for Solidly Mounted BAW Resonators," in *Proc. IEEE Ultrasonics Symposium*, 2005, pp. 329–332.

[37] A. Jansman, F. Vanhelmont, R. Milsom, J. Ruigrok, F. de Bruijn, R. Lufting, and J.-W. Lobeek, "Bulk acoustic wave resonators and filters – 2D modelling and industrialization aspects," in *Proc. IEEE Ultrasonics Symposium*, vol. 1, 2005, pp. 97–100.

[38] J.-W. Lobeek, R. Strijbos, A. Jansman, N. X. Li, A. Smolders, and N. Pulsford, "High-Q BAW Resonator on Pt/Ta2O5/SiO2-based Reflector Stack," in *IEEE MTT-S Microwave Symposium Digest*, 2007, pp. 2047–2050.

[39] R. Milsom, "Two-Dimensional Theory of Thin-Film ZnO Resonators on Silicon," in *Proc. IEEE Ultrasonics Symposium*, 1982, pp. 484–489.

[40] K. Lakin, "Numerical analysis of two dimensional thin film resonators," *Proc. IEEE International Frequency Control Symposium*, pp. 502–508, 1993.

[41] R. Ruby, J. Larson, R. Fazzio, and C. Feng, "Performance degradation effects in FBAR filters and resonators due to lamb wave modes," in *Proc. IEEE Ultrasonics Symposium*, 2005, pp. 1832–1835.

[42] M. Lowe, "Matrix Techniques for Modeling Ultrasonic Waves in Multilayered Media," *IEEE Trans. on Ultrasonics, Ferroelectrics, and Frequency Control*, vol. 42, no. 4, pp. 525–541, 1995.

[43] R. Milsom, H.-P. Lobl, C. Metzmacher, P. Lok, A. Tuinhout, and F. van Straten, "2D model of solidly-mounted and membrane BAW devices," in *Proc. IEEE Ultrasonics Symposium*, 2003, pp. 1802–1807.

[44] W. Shockley, D. Curran, and D. Koneval, "Energy Trapping and Related Studies of Multiple Electrode Filter Crystals," in *Proc. 17th Annual Symposium on Frequency Control*, 1963, pp. 88–126.

[45] J. Meltaus, T. Pensala, and K. Kokkonen, "Modelling of 2-D lateral modes in solidly-mounted BAW resonators," in *Proc. IEEE Ultrasonics Symposium*, 2008, pp. 1544–1547.

[46] T. Makkonen, A. Holappa, J. Ella, and M. Salomaa, "Finite element simulations of thin-film composite BAW resonators ," *IEEE Trans. on Ultrasonics, Ferroelectrics, and Frequency Control*, vol. 48, no. 5, pp. 1241–1258, 2001.

[47] R. Thalhammer, G. Fattinger, M. Handtmann, and S. Marksteiner, "Ohmic effects in BAW-resonators," in *IEEE MTT-S Microwave Symposium Digest*, 2006, pp. 390–393.

[48] R. Thalhammer, J. Kaitila, R. Aigner, and S. Marksteiner, "Prediction of BAW resonator performance using experimental and numerical methods," in *Proc. IEEE Ultrasonics Symposium*, 2004, pp. 282–285.

[49] M. Mayer, S. Zaglmayr, K. Wagner, and J. Schoberl, "Perfectly Matched Layer Finite Element Simulation of Parasitic Acoustic Wave Radiation in Microacoustic Devices," in *Proc. IEEE Ultrasonics Symposium*, 2007, pp. 702–706.

[50] D. Ekeom, B. Dubus, and A. Volatier, "Solidly Mounted Resonator (SMR) FEM-BEM Simulation," in *Proc. IEEE Ultrasonics Symposium*, 2006, pp. 1474–1477.

[51] J. D. L. III, R. C. Ruby, and P. Bradley, *U.S. Patent 6 215 375 B1*, Apr. 10 2001.

[52] D. Rosen, J. Bjurstrom, and I. Katardjiev, "Suppression of spurious lateral modes in thickness-excited FBAR resonators," *IEEE Trans on. Ultrasonics, Ferroelectrics and Frequency Control*, vol. 52, no. 7, pp. 1189–1192, 2005.

[53] A. Link, E. Schmidhammer, H. Heinze, M. Mayer, B. Bader, and R. Weigel, "Appropriate Methods to Suppress Spurious FBAR Modes in Volume Production," in *IEEE MTT-S Microwave Symposium Digest*, 2006, pp. 394–397.

[54] T. Pensala, M. Ylilammi, J. Meltaus, and K. Kokkonen, "Area and Dispersion Dependence of Vibration Shape and Coupling Coefficient in Thin Film BAW Resonators," in *Proc. IEEE Ultrasonics Symposium*, 2007, pp. 1661–1664.

[55] G. Fattinger, S. Marksteiner, J. Kaitila, and R. Aigner, "Optimization of acoustic dispersion for high performance thin film BAW resonators," in *Proc. IEEE Ultrasonics Symposium*, vol. 2, 2005, pp. 1175–1178.

[56] R. Sykes and W. Beaver, "High Frequency Monolithlc Crystal Filters with Posslble Application to Single Frequency and Single Side Band Use," in *Proc. 20th Annual Symposium on Frequency Control*, 1966, pp. 288–308.

[57] K. Lakin, J. Belsick, J. McDonald, and K. McCarron, "High performance stacked crystal filters for GPS and wide bandwidth applications," in *Proc. IEEE Ultrasonics Symposium*, 2001, pp. 833–838.

[58] K. Lakin, "Coupled resonator filters," in *Proc. IEEE Ultrasonics Symposium*, 2002, pp. 901–908.

[59] G. Fattinger, J. Kaitila, R. Aigner, and W. Nessler, "Single-to-balanced filters for mobile phones using coupled resonator BAW technology," in *Proc. IEEE Ultrasonics Symposium*, 2004, pp. 416–419.

[60] A. Volatier, E. Defay, A. N'hari, J. Carpentier, P. Ancey, and B. Dubus, "Design, Elaboration and Characterization of Coupled Resonator Filters for WCDMA Applications," in *Proc. IEEE Ultrasonics Symposium*, 2006, pp. 829–832.

[61] M. Small, T. Jamneala, L. Callaghan, J. Larson, and R. Ruby, "A De-Coupled Stacked Bulk Acoustic Resonator (DSBAR) Filter With 2 dB Bandwidth > 4% ," in *Proc. IEEE Ultrasonics Symposium*, 2007, pp. 604–607.

[62] T. Grudkowski, J. Black, G. Drake, and D. Cullen, "Progress in the Development of Miniature Thin Film Baw Resonator and Filter Technology," in *Proc. 36th Annual Symposium on Frequency Control*, 1982, pp. 537–548.

[63] V. Yantchev and I. Katardjiev, "Micromachined thin film plate acoustic resonators utilizing the lowest order symmetric Lamb wave mode," *IEEE Trans. on Ultrasonics, Ferroelectrics, and Frequency Control*, vol. 54, no. 1, pp. 87–95, 2007.

[64] W. Pan, R. Abdolvand, and F. Ayazi, "A low-loss 1.8GHz monolithic thin-film piezoelectric-on-substrate filter," in *Proc. IEEE 21st International Conference on Micro Electro Mechanical Systems*, 2008, pp. 176–179.

[65] J. Meltaus, T. Pensala, K. Kokkonen, and A. Jansman, "Laterally coupled solidly mounted BAW resonators at 1.9 GHz," in *Proc. IEEE Ultrasonics Symposium*, 2009, pp. 847–850.

[66] J. E. Graebner, B. P. Barber, P. L. Gammel, D. S. Greywall, and S. Gopani, "Dynamic visualization of subangstrom high-frequency surface vibrations," *Applied Physics Letters*, vol. 78, no. 2, pp. 159–161, 2001.

[67] G. G. Fattinger and P. T. Tikka, "Modified Mach-Zender laser interferometer for probing bulk acoustic waves," *Applied Physics Letters*, vol. 79, no. 3, pp. 290–292, 2001.

[68] H. Martinussen, A. Aksnes, and H. E. Engan, "Wide frequency range measurements of absolute phase and amplitude ofvibrations in micro- and nanostructures by optical interferometry," *Opt. Express*, vol. 15, no. 18, pp. 11 370–11 384, 2007.

[69] K.-Y. Hashimoto, K. Kashiwa, T. Omori, M. Yamaguchi, O. Takano, S. Meguro, and K. Akahane, "A fast scanning laser probe based on Sagnac interferometer for RF surface and bulk acoustic wave devices," in *IEEE MTT-S Microwave Symposium Digest*, 2008, pp. 851–854.

[70] H. Yatsuda, S. Kamiseki, and T. Chiba, "Calculation and optical measurement of SAW diffraction pattern of slanted finger SAW filters on YZ LiNbO3 and 128YX LiNbO3 ," in *Proc. IEEE Ultrasonics Symposium*, 2001.

[71] J. V. Knuuttila, P. T. Tikka, and M. M. Salomaa, "Scanning Michelson interferometer for imaging surface acoustic wave fields," *Opt. Lett.*, vol. 25, no. 9, pp. 613–615, 2000.

[72] K. Kokkonen and M. Kaivola, "Scanning heterodyne laser interferometer for phase-sensitive absolute-amplitude measurements of surface vibrations," *Applied Physics Letters*, vol. 92, no. 6, 2008.

[73] J. Graebner, H. Safar, B. Barber, P. Gammel, G. Herbsommer, L. Fetter, J. Pastalan, H. Huggins, and R. Miller, "Optical mapping of surface vibrations on a thin-film resonator near 2 GHz," in *Proc. IEEE Ultrasonics Symposium*, 2000, pp. 635–638.

[74] K. Kokkonen and T. Pensala, "Laser Interferometric Measurements and Simulations of Waves Transmitted Through the Acoustic Mirror in Thin Film BAW Resonator," in *Proc. IEEE Ultrasonics Symposium*, 2006, pp. 460–463.

[75] A. Link, E. Schmidhammer, M. Mayer, B. Bader, K. Wagner, and R. Weigel, "2D-FEM Modeling of Mirror-Type FBARs Based on an Adapted Set of Material Parameters," in *Proc. IEEE Ultrasonics Symposium*, 2006, pp. 452–455.

[76] A. Hagelauer, B. Bader, G. Henn, A. Schaeufele, S. Marksteiner, K. Wagner, and R. Weigel, "Low-loss BAW filters on high resistivity silicon for mobile radio," in *IEEE MTT-S Microwave Symposium Digest*, 2009, pp. 337–340.

[77] K. Lakin, J. Belsick, J. McDonald, and K. McCarron, "Improved bulk wave resonator coupling coefficient for wide bandwidth filters," in *Proc. IEEE Ultrasonics Symposium*, 2001, pp. 827–831.

[78] D. Feld, R. Parker, R. Ruby, P. Bradley, and S. Dong, "After 60 years: A new formula for computing quality factor is warranted," in *Proc. IEEE Ultrasonics Symposium*, 2008, pp. 431–436.

[79] R. Ruby, R. Parker, and D. Feld, "Method of Extracting Unloaded Q Applied Across Different Resonator Technologies," in *Proc. IEEE Ultrasonics Symposium*, 2008, pp. 1815–1818.

[80] M. Allah, J. Kaitila, R. Thalhammer, W. Weber, and D. Schmitt-Landsiedel, "Temperature compensated solidly mounted bulk acoustic wave resonators with optimum piezoelectric coupling coefficient," in *proc. IEEE Electron Devices Meeting*, 2009, pp. 1–4.

[81] Q. Zou, D. Lee, F. Bi, R. Ruby, M. Small, S. Ortiz, Y. Oshmyansky, and J. Kaitila, "High coupling coefficient Temperature compensated FBAR resonator for oscillator application with wide pulling range," in *Proc IEEE Frequency Control Symposium*, 2010, pp. 646–651.

[82] R. Gabl, E. Green, M. Schreiter, H. Feucht, H. Zeininger, R. Primig, D. Pitzer, G. Eckstein, and W. Wersing, "Novel integrated FBAR sensors: a universal technology platform for bio- and gas-detection," in *Proc. IEEE Conference on Sensors*, vol. 2, 2003, pp. 1184–1188.

[83] J. Enlund, D. Martin, V. Yantchev, and I. Katardjiev, "FBAR sensor array for in liquid operation," *IEEE Sensors Journal*, no. 99, p. 1, 2010.

[84] M. Kadota, T. Ogami, K. Yamamoto, Y. Negoro, and H. Tochishita, "High frequency Lamb wave device composed of LiNbO3 thin film," in *Proc. IEEE Ultrasonics Symposium*, 2008, pp. 1940–1943.

[85] M. Akiyama, T. Kamohara, K. Kano, A. Teshigahara, Y. Takeuchi, and N. Kawahara, "Enhancement of Piezoelectric Response in Scandium Aluminum Nitride Alloy Thin Films Prepared by Dual Reactive Cosputtering," *Advanced Materials*, vol. 21, pp. 593–596, 2009.

[86] K.-Y. Hashimoto, Y. Wang, T. Omori, M. Yamaguchi, M. Kadota, H. Kando, and T. Shibahara, "Piezoelectric boundary acoustic waves: Their underlying physics and applications," in *Proc. IEEE Ultrasonics Symposium*, 2008, pp. 999–1005.

[87] H. Kando, D. Yamamoto, M. Mimura, T. Oda, A. Shimizu, K. Shimoda, E. Takata, T. Fuyutsume, R. Kubo, and M. Kadota, "RF Filter using Boundary Acoustic Wave," in *Proc. IEEE Ultrasonics Symposium*, 2006, pp. 188–191.

Papers 1–6 are not included in the PDF version.
Please order the printed version to get the complete publication
(http://www.vtt.fi/publications/index.jsp).

Series title, number and report code of publication

VTT Publications 756
VTT-PUBS-756

Author(s)
Tuomas Pensala

Title

Thin Film Bulk Acoustic Wave Devices
Performance Optimization and Modeling

Abstract

Thin film bulk acoustic wave (BAW) resonators and filters operating in the GHz range are used in mobile phones for the most demanding filtering applications and complement the surface acoustic wave (SAW) based filters. Their main advantages are small size and high performance at frequencies above 2 GHz. This work concentrates on the characterization, performance optimization, and modelling techniques of thin film BAW devices.

Laser interferometric vibration measurements together with plate wave dispersion modeling are used to extract the full set of elastic material parameters for sputter deposited ZnO, demonstrating a method for obtaining material data needed for accurate simulation of the devices.

The effectiveness of the acoustic interference reflector used to isolate the vibration from the substrate is studied by 1-D modeling, 2-D finite element method and by electrical and laser interferometric measurements. It is found that the Q-value of reflector-based BAW resonators operating at 2 GHz is limited to approximately 2000 by mechanisms other than leakage through the reflector.

Suppression of spurious resonances in ZnO resonators is studied in depth by modeling and measurements. It is verified that the approximate mode orthogonality is behind the suppression in boundary frame type ZnO devices operating in the piston mode, but also another narrow band mode suppression mechanism is found.

A plate wave dispersion based 2-D simulation scheme for laterally acoustically coupled BAW resonator filters is developed and employed in designing of experimental devices, which show both good agreement with the model predictions and a remarkable 4.9 % relative bandwidth.

ISBN
978-951-38-7722-4 (soft back ed.)
978-951-38-7723-1 (URL: http://www.vtt.fi/publications/index.jsp)

Series title and ISSN	Project number
VTT Publications 1235-0621 (soft back ed.) 1455-0849 (URL: http://www.vtt.fi/publications/index.jsp)	70339

Date	Language	Pages
January 2011	English, Finnish abstr.	97 p. + app. 73 p.

Name of project	Commissioned by

Keywords	Publisher
Thin film, bulk acoustic wave, BAW, AlN, ZnO, resonator, filter, GHz, microacoustic, modeling, interferometric imaging	VTT Technical Research Centre of Finland P.O. Box 1000, FI-02044 VTT, Finland Phone internat. +358 20 722 4520 Fax +358 20 722 4374

Julkaisun sarja, numero ja raporttikoodi

VTT Publications 756
VTT-PUBS-756

Tekijä(t)
Tuomas Pensala

Nimeke

Pietsosähköiset ohutkalvoresonaattorit
Suorituskyvyn optimointi ja mallinnus

Tiivistelmä

Pietsosähköisiin ohutkalvoihin perustuvia GHz-alueen mikroakustisia tilavuusaaltoresonaattoreita (BAW) ja niihin pohjautuvia suodattimia käytetään matkapuhelinteknologiassa kaikkein vaativimmissa suodatuskohteissa. Teknologian keskeiset edut ovat pieni koko ja hyvä suorituskyky korkeilla (≥ 2 GHz) taajuuksilla. Työssä keskityttiin BAW-resonaattoreiden karakterisointiin, suorituskyvyn optimointiin ja mallinnustekniikkoihin.

Laserinterferometrimittauksia ja Lambin aaltojen dispersion mallinnusta käytetään yhdessä ohutkalvomateriaalin elastisten materiaaliparametrien määrittämiseen. Näin demonstroidaan menetelmä, jolla voidaan parantaa mm. mallinnuksen tarkkuutta paremman materiaaliparametritiedon kautta. Resonaattorit substraatista erottavan akustisen peilin ominaisuuksia analysoidaan 1D-malleilla, 2D-elementtimenetelmällä sekä kokeellisesti sähköisin ja laserinterferometrimittauksin. Akustista peiliä parantamalla n. 2 GHz taajuudella toimivien resonaattorien hyvyyslukua ei saada parannettua juurikaan yli 2000:n.

Sivuresonanssien vaimennusta reunapaksunnosmenetelmällä ZnO-resonaattoreissa analysoidaan mallinnuksella ja mittauksin. Tulokset osoittavat, että sivuresonanssit saadaan vaimennettua laajalla kaistalla niiden ominaismuotojen heikkoon lineaariseen riippuvuuteen perustuen, mutta myös toinen kapeakaistainen vaimennusefekti havaitaan.

Laatta-aaltojen dispersio-ominaisuuksiin perustuen kehitetään tehokas 2D-mallinnusmenetelmä, jolla voidaan simuloida horisontaalisesti akustisesti kytkettyjä suodattimia. Mallia vertaillaan kokeellisiin suodattimiin hyvin tuloksin, ja sen avulla suunniteltu kokeellinen suodatin saavuttaa 4,9 % suhteellisen kaistanleveyden 2 GHz:n taajuudella.

ISBN
978-951-38-7722-4 (nid.)
978-951-38-7723-1 (URL: http://www.vtt.fi/publications/index.jsp)

Avainnimeke ja ISSN	Projektinumero
VTT Publications 1235-0621 (nid.) 1455-0849 (URL: http://www.vtt.fi/publications/index.jsp)	70339

Julkaisuaika	Kieli	Sivuja
Tammikuu 2011	Englanti, suom. tiiv.	97 s. + liitt. 73 s.

Projektin nimi	Toimeksiantaja(t)

Avainsanat	Julkaisija
Thin film, bulk acoustic wave, BAW, AlN, ZnO, resonator, filter, GHz, microacoustic, modeling, interferometric imaging	VTT PL 1000, 02044 VTT Puh. 020 722 4520 Faksi 020 722 4374

VTT PUBLICATIONS

738 Fusion Yearbook. Association EURATOM-TEKES. Annual Report 2009. Eds. by Seppo Karttunen & Markus Airila. 2010. 136 p. + app. 13 p.

739 Satu Hilditch. Identification of the fungal catabolic D-galacturonate pathway. 2010. 74 p. + app. 38 p.

740 Mikko Pihlatie. Stability of Ni-YSZ composites for solid oxide fuel cells during reduction and re-oxidation. 2010. 92 p. + app. 62 p.

741 Laxmana Rao Yetukuri. Bioinformatics approaches for the analysis of lipidomics data. 2010. 75 p. + app. 106 p.

742 Elina Mattila. Design and evaluation of a mobile phone diary for personal health management. 2010. 83 p. + app. 48 p.

743 Jaakko Paasi & Pasi Valkokari (eds.). Elucidating the fuzzy front end – Experiences from the INNORISK project. 2010. 161 p.

744 Marja Vilkman. Structural investigations and processing of electronically and protonically conducting polymers. 2010. 62 p. + app. 27 p.

745 Juuso Olkkonen. Finite difference time domain studies on sub-wavelength aperture structures. 2010. 76 p. + app. 52 p.

746 Jarkko Kuusijärvi. Interactive visualization of quality Variability at run-time. 2010. 111 p.

747 Eija Rintala. Effects of oxygen provision on the physiology of baker's yeast *Saccharomyces cerevisiae*. 2010. 82 p. + app. 93 p.

748 Virve Vidgren. Maltose and maltotriose transport into ale and lager brewer's yeast strains. 2010. 93 p. + app. 65 p.

749 Toni Ahonen, Markku Reunanen & Ville Ojanen (eds.). Customer value driven service business development. Outcomes from the Fleet Asset Management Project. 2010. 43 p. + app. 92 p.

750 Tiina Apilo. A model for corporate renewal. Requirements for innovation management. 2010. 167 p. + app. 16 p.

751 Sakari Stenudd. Using machine learning in the adaptive control of a smart environment. 2010. 75 p.

752 Evanthia Monogioudi. Enzymatic Cross-linking of β-casein and its impact on digestibility and allergenicity. 2010. 85 p. + app. 66 p.

753 Jukka-Tapani Mäkinen. Concurrent engineering approach to plastic optics design. 2010. 99 p. + app. 98 p.

754 Sanni Voutilainen. Fungal thermostable cellobiohydrolases. Characterization and protein engineering studies. 2010. 98 p. + app. 55 p.

756 Tuomas Pensala. Thin Film Bulk Acoustic Wave Devices. Performance Optimization and Modeling. 2011. 97 p. + app. 73 p.

ISBN 978-951-38-7722-4 (soft back ed.)
ISSN 1235-0621 (soft back ed.)
ISBN 978-951-38-7723-1 (URL: http://www.vtt.fi/publications/index.jsp)
ISSN 1455-0849 (URL: http://www.vtt.fi/publications/index.jsp)